

# **Thermal Design of Electrical Machines**

Investigation and Evaluation of Cooling  
Performances

**Zhe Huang**



**LUND UNIVERSITY**

**Licentiate Thesis**  
**Department of Measurement Technology and**  
**Industrial Electrical Engineering**

**2013**

Department of Measurement Technology and Industrial Electrical Engineering  
Faculty of Engineering  
Lund University  
Box 118  
221 00 LUND  
SWEDEN

<http://www.iea.lth.se>

ISBN:978-91-88934-62-8

CODEN:LUTEDX/(TEIE-1070)/1-141/(2013)

© Zhe Huang, 2013

Printed in Sweden by Media-Tryck, Lund University  
Lund 2013

We cannot solve problems with the same  
thinking we used when we created them

*A. Einstein*



# Abstract

This Thesis focuses on thermal design of permanent magnet synchronous electrical machines (PMSM) used in hybrid vehicles (HEVs) or zero emission vehicles (ZEVs). Electrical machines in such applications are usually designed with high power density requirements but within limited spaces, which lead to high rate of heat generation but low rate of heat dissipation. Therefore, highly efficient thermal design or cooling methods are needed.

Firstly, the thesis discusses different possible approaches to improve the thermal design of electrical machines, which by either decreasing heat generations or increasing heat dissipations. Among different options, direct cooling system is studied further and compared to indirect cooling system.

In this study, three simulation approaches namely Computational Fluid Dynamics (CFD), Finite Element Analysis (FEA) and Lumped Parameter Method (LPM) are applied to different calculation domains with different purposes.

The calculation domain of CFD simulation is selected for coolant, sometimes with limited volume of solid of electrical machines. The aims of CFD simulations in this study are: 1) rough comparisons on direct and indirect cooling systems 2) study of individual cooling channel and forming heat transfer coefficient maps. On the other hand, the calculated domain of FEA simulation is the whole machine, besides the coolant. The interfaces between the coolant and solid are set with boundary conditions which are heat transfer coefficients obtained by CFD simulations. The aim of FEA simulation in this study is to compare the heat transfer and differences between the direct and indirect cooling systems especially at the hot spots. Moreover, the calculated domain of LPM is the complete machine which also uses the heat transfer coefficients calculated by CFD at the boundaries between coolant and solid. The aim of using LPM in this study is to predict the transient distribution of machine temperatures and

furthermore to evaluate the machine thermal performances with different driving cycles.

This thesis also proposes Hydraulic Equivalent Circuit (HEC) method in order to evaluate the flow network for the cooling system, which uses the analogy between the electric circuit and hydraulic circuit.

In addition, this thesis also shows the in-house built experimental system in order to test the cooling system and temperatures for electrical machines. The comparison between measurement results and simulation results are discussed.

# Acknowledgements

First of all, I would express my great thanks to my supervisor Prof. Mats Alaküla who is always ready to help and supportive both in research and life. His great guidance and open attitude encourages me and walks me through many obstructions.

I would also to thank my co-supervisors Assoc. Prof. Avo Reinap and Prof. Jinliang Yuan who have brought me different perspectives of electrical machines and heat transfer. I really appreciate the great and fruitful discussions which always brings brilliant ideas.

I would offer my special thanks to my fantastic project partners who work together with me from the first day of the project and openly share valuable experiences and ideas: Tom Sundelin, Svante Bylund, Viktor Lassila and Jens Wagberg from BAE System Hägglunds; Prof. Mats Leksell, Assoc. Prof. Oskar Wallmark and Shafigh Nategh from Kungliga Tekniska Högskolan (KTH); Magnus Linenmo from Surahammars Bruk; Jerker andersson from Dahrenråd; Lars Kvarnsjoe from Vacuumschelze; Fredrik Krantz from Magcomp; Kristoffer Nilsson and Kathiravan Ramanujam from BorgWarner. I would like to express my appreciation to Jan Folkhammar and his staff who provide their time, equipment and labs in Bevi to assist the material tests and also the pre-tests for the cooling systems.

I wish to acknowledge the help provided by Getachew Darge and Yury Loayza-Vargas who gave me great support during the machine test procedures. I would also like to acknowledge Francisco Márquez, Dan Hagstedt, Rasmus Andersson and Evripidis Karatsivos who share their great technical ideas and discussions with me. I would like to thank Henriette Weibull, Carla Caverzagli Alvarez and Sergio Branda who gave me great help on finding stable accommodations in Lund. My special acknowledgement also extends to all my colleagues and lunch friends in

IEA who made great efforts for a friendly working environment.

Last but not the least I am particularly grateful for the support and assistance given by my dear parents Puxian Huang and Shouchao Hao and my lovely boyfriend Ka-Wei Tang as well as all the rest of my family.

Lund, 12 July 2013  
*Zhe Huang*



# Contents

<b>CHAPTER 1 INTRODUCTION.....</b>	<b>1</b>
1.1 BACKGROUND.....	1
1.2 OBJECTIVES .....	1
1.3 OUTLINE OF THE THESIS .....	2
1.4 CONTRIBUTIONS .....	3
1.5 PUBLICATIONS .....	3
<b>CHAPTER 2 HEAT TRANSFER IN ELECTRICAL MACHINES ....</b>	<b>5</b>
2.1 OVERVIEW .....	6
2.2 HEAT TRANSFER ENHANCEMENT APPROACHES.....	12
2.3 INDIRECT COOLING AND DIRECT COOLING .....	19
2.4 SUMMARY .....	20
<b>CHAPTER 3 DESIGN OF COOLING CIRCUITS.....</b>	<b>23</b>
3.1 COOLING OBJECT .....	23
3.2 COOLING MEDIUM .....	24
3.3 CFD THEORY .....	25
3.4 CFD GEOMETRY AND BOUNDARY CONDITIONS .....	31
3.5 COOLING MAPS .....	36
3.6 HYDRAULIC EQUIVALENT CIRCUIT (HEC) .....	44
3.7 SPECIFICATION OF COOLING CHANNELS FOR PRACTICAL IMPLEMENTATION .....	50
3.8 FLOW NETWORK OF SELECTED COOLING SYSTEMS .....	53
3.9 SUMMARY .....	58
<b>CHAPTER 4 HEAT GENERATIONS IN ELECTRICAL MACHINES .....</b>	<b>61</b>

4.1	INTERIOR PERMANENT MAGNET SYNCHRONOUS MACHINE (IPMSM).....	61
4.2	POWER LOSSES IN THE WINDINGS .....	62
4.3	POWER LOSSES IN THE STATOR CORE.....	64
4.4	POWER LOSSES IN THE ROTOR.....	66
4.5	POWER LOSS MAP OVER VARIOUS OPERATION POINTS .....	67
4.6	SUMMARY .....	68
<b>CHAPTER 5 HEAT TRANSFER ANALYSIS.....</b>		<b>69</b>
5.1	MODEL DEFINITION.....	70
5.2	MATERIAL PROPERTIES .....	72
5.3	LOSSES .....	73
5.4	3D FINITE ELEMENT THERMAL ANALYSIS .....	73
5.5	LUMPED PARAMETER MODEL (LPM).....	78
5.6	LPM WITH DRIVING CYCLES .....	79
5.7	SUMMARY .....	83
<b>CHAPTER 6 EXPERIMENTAL SETUP .....</b>		<b>85</b>
6.1	THE THERMAL TEST METHOD.....	85
6.2	EXPERIMENTAL SETUP .....	88
6.3	HYDRAULIC MEASUREMENTS .....	89
6.4	TEMPERATURE MEASUREMENT.....	92
6.5	SUMMARY .....	95
<b>CHAPTER 7 EVALUATION.....</b>		<b>97</b>
7.1	COOLING SYSTEM.....	97
7.2	WINDING RESISTANCE TEST .....	101
7.3	TEMPERATURE MEASUREMENT RESULTS.....	102
7.4	PRACTICAL REALIZATION OF COOLING CIRCUITS .....	114
7.5	SUMMARY .....	115
<b>CHAPTER 8 CONCLUSIONS.....</b>		<b>117</b>
8.1	REFLECTIONS .....	117
8.2	FUTURE WORK.....	118
<b>REFERENCES.....</b>		<b>121</b>
<b>ABBREVIATIONS.....</b>		<b>125</b>
	ACRONYMS .....	125
	SYMBOLS .....	126

# Chapter 1

## Introduction

### 1.1 Background

In electrical drives in general, and in electrical vehicle drives in particular, it is important to predict the thermal performance limit since this sets the electromechanical performance limit. Besides the power electronics, the electric machine is a core component in the Hybrid Electric Vehicle (HEV)'s or Zero Emission Vehicle (ZEV)'s electric drive system. Based on the driving schedule, the machine will run under the motoring state during vehicle starting, electric assist propulsion or pure electric propulsion. The electric machine is required to operate under the normal generating state during engine propulsion (thereby charging batteries) and the regenerating state during vehicle braking. Obviously, the performances of the electric machine will directly govern the performances of the electric drive system and consequently the fuel economy of the vehicle. 0

However, the limited space and high power density required by the vehicles address more on the thermal issues of the electric machines. Decent thermal design of compact high performance electric motors is a key area to make competitive hybrid electric drivelines for vehicles. Furthermore, various cooling methods differently affect the electric machines in terms of heat removal, cost and life time.

### 1.2 Objectives

The Termsos project is made as a continuation and a complement to Green

Car project<sup>1</sup>. Based on the electric machine designed in the Green Car project, this project aims to understand and compare different cooling methods and develops knowledge to evaluate thermal characteristics of materials and physical design in order to optimize heat transfer performance within given volume and cost. The work throughout the whole project comprises development of models and simulations, prototype development and experimental tests.

### **1.3 Outline of the Thesis**

This thesis contains the following 8 chapters and covers the discussions on heat dissipation, heat generation, thermal modelling and simulations, experimental verification, conclusions and future works.

Chapter 1 is the introductions on the background and objectives of the project. Besides, it addresses the contributions of the project and also a list of the publications.

Chapter 2 discusses the different approaches of decreasing heat generation or increasing heat dissipation in order to improve the heat transfer performances of electric machines in electric vehicle drivetrains. In the end, the studied scopes of this project are narrowed down to investigate on the direct cooling system compared to indirect cooling system.

Chapter 3 presents the design of cooling circuits for the electric machines obtained from Green Car project. Both the theories and simulations (or calculations) of CFD simulations and Hydraulic Equivalent Circuits (HEC) are presented. The CFD and HEC tools finalize the cooling circuit design step by step.

Chapter 4 discusses the heat generations inside the electric machines.

Chapter 5 presents the finite-element analysis (FEA) thermal model and the lumped parameter thermal model (LPM) for the machine with designed cooling systems.

---

<sup>1</sup> Green Car project is financed by Swedish State through Vinnova and conducted by Lund University, AB Volvo, BAE Systems Hägglunds, SAAB Automobile, Volvo Cars, Haldex Traction, Bevi AB, Surahammars Bruk, Sura Magnets AB and Höganäs AB.

Chapter 6 and 7 present the test setup and measurement results separately. The comparisons between the machines with direct and indirect cooling systems from both tests and simulations are shown.

Chapter 8 presents the conclusions and future work of the study.

## 1.4 Contributions

The presented research work has the following contributions for electrical motor design and thermal analysis.

First of all, this research work introduces a new cooling approach for the electrical machines in vehicle drivetrains. Besides, the differences obtained from both tests and simulations between the two cooling systems can be applied into further studies.

Secondly, the research work proposes a conjugated numerical method for heat transfer analysis of electrical machines. The CFD tools are used for machine cooling circuit designs in order to evaluate different designs and then obtain accurate heat transfer coefficients of cooling systems. Based on the obtained results from CFD and combined FEA thermal simulations, more accurate and complete thermal analysis of electric machine is obtained.

Thirdly, developing the knowledge of internal forced cooling and temperature measurements for electrical machines are also one of the main contributions from this research work.

## 1.5 Publications

F. Marquez-Fernandez, A. Reinap, Z. Huang, M. Alaküla, “Dynamic Evaluation of the Overloading Potential of a Convection Cooled Permanent Magnet Synchronous Motor”, IEEE International Electric Machines & Drives Conference (IEMDC), Niagara Falls, Canada, 2011.

Shafiqh Nategh, Andreas Krings, Zhe Huang, Oskar Wallmark, Mats Leksell and Magnus Lindenmo, ‘Evaluation of Stator and Rotor Lamination Materials for Thermal Management of a PMaSRM’, 20th International Conference on Electrical Machines (ICEM), Marseille,

2-5 September 2012.

Zhe Huang, Shafigh Nategh, Mats Alaküla, Viktor Kassila, Jinliang Yuan, “Direct Oil Cooling of Traction Motors in Hybrid Drives”, IEEE International Electric Vehicle Conference (IEVC), Greenville, SC, 2012.

Zhe Huang, Francisco Marquez, Mats Alaküla, Jinliang Yuan, “Characterization and Application of Forced Cooling Channels for Traction Motors in HEVs”, XXth International Conference on Electrical Machines (ICEM), Marseille, 2-5 September 2012.

Francisco Marquez, Zhe Huang, Mats Alaküla, “Redesign of an Electrical Rear Wheel Drive (E-RWD) for a hybrid vehicle in a given drive cycle”, XXth International Conference on Electrical Machines (ICEM), Marseille, 2-5 September 2012.

Shafigh Nategh, Zhe Huang, Oskar Wallmark, Mats Leksell, Andreas Krings, “Thermal Modeling of Directly Cooled Electric Machines Using Lumped Parameter and Limited CFD Analysis”, IEEE Trans. Energy Conversion, submitted.

## Chapter 2

# Heat Transfer in Electrical Machines

Generally speaking, in order to improve the heat transfer performance of any device, there are two main factors to adjust, which are heat generation rate and heat dissipation rate. The difference in heat power results in integration of temperature, which is the quantity that sets the limits for power transfer capability of any device.

For two electrical motor designs, if they produce the same torque and speed, i.e. with the identical mechanical performances, the one with lower heat generation rate or better heat dissipation rate has better heat transfer performance and lower temperature inside the motor. From another perspective, if two electrical motors have the same material grades, i.e. same maximum temperature limitations, the one with lower loss generations or better heat dissipations leads to lower temperatures with identical current rating or leads to better mechanical performance when it reaches the same temperature limitations.

Therefore, if a better heat transfer performance of an electrical machine is pursued, one should have good knowledge of how heat is generated and dissipated in and around the machine. Thereafter, executable proposals for heat transfer improvement can be created.

This chapter discusses heat transfer theory and various solutions to enhance heat transfer performances of electrical machines. Some of the suggested solutions belong to the category of ‘decreasing losses generation’ and the others belong to the category of ‘increasing heat dissipation’. Among these solutions, one promising solution which is the ‘direct cooling motor’ is chosen and studied further in the following

chapters.

## 2.1 Overview

This part presents an overview of heat generation and heat dissipation in electrical machines. Figure 2.1 shows specific parts of an electrical machine, which includes rotor, stator, shaft, winding end part/end winding and winding active part/active winding. Since the active winding is embedded in the stator and not able to be seen from this sectional view, it is shown by the dashed lines in the picture. The heat generation is categorized by different locations of heat sources. The heat dissipation is classified by different heat diffusing mechanisms.

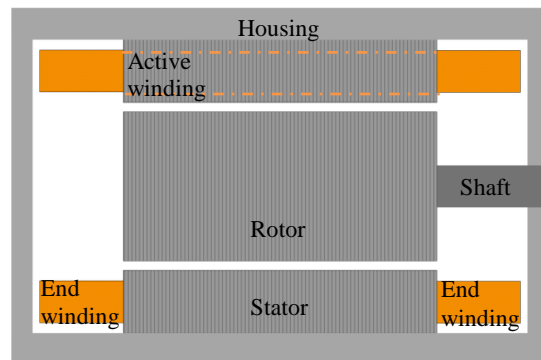


Figure 2.1 Sectional view of an electrical machine

### Heat generation

Electrical machines used in hybrid or pure electrical drivetrain systems are able to work as motors when vehicles are propelled and generators when vehicles are braking. When the electrical machines work as motors, electrical energy is transferred into mechanical energy. The energy transmission forms are reversed for generators. The electrical machine efficiency is defined as the percentage of the output power versus the input power as shown in [2].

The difference between input power and output power is the summation of power losses generated by different irreversible energy conversion processes in different materials in electrical machines, which become heat eventually. The ways to categorize electrical machine losses are similar among different types of machines though the ratio of each type of loss



over the total losses is differed.

Based on the discussion in [2] and [3], the losses in electrical machines can be categorized by heat generated locations or spatial distribution of heat sources as following. Different types of losses are shortly discussed here and detailed mathematic calculations are presented in chapter 4.

- **Winding losses**

Winding losses are divided into two types which according to the character of the current are DC current losses and AC current losses.

The DC current losses are proportional to the winding electrical resistance and square of current value. Since the electrical resistance is defined by  $R_{el} = \rho_e L/A$  and current is defined by  $I = JA$ , the DC current losses can be expressed as  $P_{DC} = J^2 \rho_e V$ . Here  $\rho_e$  is the electric resistivity,  $L$ ,  $A$  and  $V$  is the length, cross section area and volume of the pure conductor, separately, and  $J$  is the current density.

The AC current losses are caused by the skin effect and proximity effect. The skin effect of a conductor is evaluated by the skin depth which is inversely proportional to the AC current frequency, which means that the higher current frequency it is, the smaller skin depth it will be, and therefore there is higher current density through the part of the conductor where current is flowing. The proximity effect of one conductor is caused by the magnetic fields created by others nearby conductors. Comparing to DC current loss, these two effects lead to the redistribution and increase of the current density in the conductors, therefore leading to increased conductor losses.

- **Core losses**

Core losses or iron losses are the energy losses generated in the soft magnetic materials. Soft magnetic materials have high initial permeability, low hysteresis loss and large magnetic induction. These materials can be easily magnetized and demagnetized. Therefore, these are known as soft magnetic materials [4]. Soft magnetic materials have wide usage as stator and rotor core

materials in electrical machine industries. They can be made into lamination form such as electrical steel laminations or powder form such as Soft Magnetic Composites (SMC).

Losses in soft magnetic materials are mainly divided into hysteresis loss and eddy current losses. Hysteresis loss is the amount of input energy expended to change the magnetic flux density polarity of the steel in conjunction with the changing polarity of the alternating magneto motive force (MMF)[5]. Eddy current losses are caused by the induced eddy currents, which are circulating currents resulting from changes of the magnetic fields in the core material.

- **Permanent magnet losses**

For permanent magnet electrical machines, there are power losses generated in the permanent magnets. As the core losses in soft magnetic materials, these losses are also classified into hysteresis losses and eddy current losses. Usually the eddy current losses are the main concern as hysteresis losses for the permanent magnets are rather related to demagnetisation processes of the hard magnetic materials. The detailed discussion on how these losses are calculated is presented in chapter 4.

- **Friction and windage losses**

These losses are due to bearing friction and rotation of the rotor and fan in air. Core loss and friction and windage losses are mainly considered as speed dependent losses as they do not vary significantly with load.

- **Stray load losses**

These losses are extra magnetic and  $I^2R$  loss due to effects of slot openings, leakage flux and harmonic fields.

### **Heat dissipation**

Similar to other forms of energy, thermal energy has a tendency of being stable at low energy status, which means the object containing high thermal energy is able to transfer to low energy status without extra force or work. During this process, there is certain amount of thermal energy released from this object to other objects or ambient through thermal

conduction, convection or radiation, which is the so called heat dissipation. Meanwhile, temperature decreases on this heat dissipated object.

- **Heat conduction**

Heat conduction is a process where heat is diffusing through solid bodies or fluids at rest. The heat flux ( $W/m^2$ ) is written as

$$q = -\lambda \frac{\partial T}{\partial n} \quad 2.1$$

where  $\lambda$  is defined as the thermal conductivity ( $W/(m K)$ ),  $\partial T / \partial n$  is the temperature gradient in the direction of the surface normal vector. The negative sign means that heat is always transferred from a region at high temperature to another region at a low temperature. [6].

For homogeneous materials, i.e. the thermal conductivity is identical in all directions, the general heat conduction equation in solid can be written

$$\underbrace{\frac{\partial T}{\partial \tau}}_{\text{Local acceleration}} = \underbrace{\frac{\lambda}{\rho c} \left\{ \frac{\partial^2 T}{\partial x^2} + \frac{\partial^2 T}{\partial y^2} + \frac{\partial^2 T}{\partial z^2} \right\}}_{\text{Diffusion}} + \underbrace{\frac{Q'}{\rho c}}_{\text{Internal heat generation}} = \frac{\lambda}{\rho c} \nabla^2 T + \frac{Q'}{\rho c} \quad 2.2$$

where  $\partial T / \partial \tau$  is the temperature gradient with respect to time,  $\lambda$  is defined as the thermal conductivity with units  $W/(m K)$ ,  $\rho$  is the density with units  $kg/m^3$ ,  $c$  is the specific heat with units  $J/(kg K)$ ,  $\partial^2 T / \partial x^2$ ,  $\partial^2 T / \partial y^2$  and  $\partial^2 T / \partial z^2$  are the second order derivative with respect to  $x$ ,  $y$  and  $z$  direction separately,  $Q'$  is the internally generated heat per unit volume element with units  $W/m^3$ .

As it marked under equation 2.2, the heat conduction inside a solid body or fluid body at rest contains the local acceleration term, heat diffusion term and internal heat generation term.  $\lambda/\rho c$  is defined as thermal diffusivity. Physical, equation 2.2 defines the rate of temperature change of a solid element both in time domain and space. For instance, big heat conduction  $\lambda$  leads to a dominating diffusion term, thereafter a big temperature variation with time.

While specific heat  $c$  has the inverse effect on the temperature variation over time comparing to  $\lambda$ .

- **Heat convection**

Heat convection often occurs at the boundaries between a solid body and a moving fluid. In the fluid the heat transport is due to a combination of molecular heat conduction and transport of internal energy due to the macroscopic motion of the fluid [6]. The heat convection can be divided into two types, named forced convection and natural convection. If the motion of the fluid is caused by pump, fan, compressor or other external forces, the convection is called forced convection. Otherwise, if the motion of the fluid is caused by inequalities of the density due to temperature differences, this convection is called the natural convection.

Because of the limited space and short time peak performance requirement, i.e. high power density output of a traction drive system, natural convection is not enough to keep all components under the limited temperatures of the materials. Therefore, forced convection approaches such as fan cooling and liquid cooling, etc. have to be involved in the cooling of electrical machines.

Depending on the flow characteristics, it is divided into laminar flow, transient flow and turbulence flow. Laminar flow tends to occur at low velocities with high viscosity fluid. According to [6], it is very hard to present a precise definition of turbulence but it has some important properties. For instance, a turbulence flow field is unsteady and the fluid motion is irregular and shows random variations in time and space concerning the detailed flow structure. According to [7], turbulent flow is a less orderly flow regime that is characterized by eddies or small packets of fluid particles which results in lateral mixing. The fluid status between laminar flow and turbulence flow is called transient flow.

From heat transfer point of view, creating a turbulence flow instead of laminar flow is one way to enhance the heat transfer of the devices.

If a body with very high thermal conductivity is considered and this body is heated or cooled by convection, the temperature

within the body will be almost uniform. The heat balance can be written

$$\rho c V \frac{dT}{d\tau} = -h_f A (T_s - T_{vf}) \quad 2.3$$

where  $h_f$  is heat transfer coefficient,  $A$  is the surface area of the solid in contact with fluid and  $V$  is its volume.

If  $\vartheta = T_s - T_{vf}$  is introduced, then equation 2.3 can be written

$$\frac{d\vartheta}{d\tau} + \frac{h_f A}{\rho c V} \vartheta = 0 \quad 2.4$$

The solution to equation 2.4 is

$$\vartheta = C_1 e^{-\frac{h_f A}{\rho c V} \tau} \quad 2.5$$

With initial condition  $T_s = T_0$ , i.e.,  $\vartheta = \vartheta_0 = T_0 - T_{vf}$  at  $\tau = 0$ , equation 2.5 gives

$$\vartheta = \vartheta_0 e^{-\frac{h_f A}{\rho c V} \tau} \quad 2.6$$

From equation 2.6 one can observe that if the initial temperature  $\vartheta_0$ , fluid properties  $\rho$  and  $c$ , studied body geometry  $V$  and  $A$  are known, then in order to obtain the temperature changes over time for a certain body, the only unknown property is the heat transfer coefficient  $h_f$ . Therefore, the determination of the correct heat transfer coefficient is the key issue in the thermal design and also the essence for the numerical and the empirical methods.

- **Heat radiation**

Thermal radiation is one type of electromagnetic radiations. It is the most difficult term to be found out empirically or calculated mathematically among the three heat dissipating methods.

Stefan-Boltzmann's law describes the radiation from a blackbody as shown below

$$E_B = \sigma T^4 \quad 2.7$$

where  $E_B$  is the total emissive power from a blackbody with units

$W/m^2$  and  $T$  is the surface temperature. The constant  $\sigma$  has the value  $\sigma = 5.67 \cdot 10^{-8} W/m^2K^4$  [6].

A body or surface having constant emissivity  $\epsilon$ , i.e, independent of wavelength, is called a gray body. For a gray body, the thermal radiation is illustrated by the equation below

$$E_g = \epsilon\sigma T^4 \quad 2.8$$

where  $E_g$  is the total emissive power from a gray body,  $\epsilon$  is the emissivity. Emissivity for different materials can be found in [8].

## 2.2 Heat transfer enhancement approaches

This part presents various solutions for heat transfer enhancement for electrical machines which has been studied in this field. Based on the ideas discussed above, some of the approaches belong to the category of ‘decreasing losses generation’ and the others belong to the category of ‘increasing heat dissipation’.

### Winding techniques

A Litz wire consists of many thin wire strands, individually insulated and twisted or woven together [9]. These types of wires are used at high frequency applications above 10 kHz. The fundamental frequency is much lower for most conventional machines and therefore the common magnetic wire is used. Still, the previously mentioned technique is used as windings in electrical machines since the twist or wove designs are able to reduce the skin effect and proximity effect losses in the windings with applied AC current. It is more common that the careful selection of parallel strands is used to get reasonably high fill-factor and good thermal packing of coils.

The fill factor defines the ratio that the total cross section area of the conductors to the total slots area, which includes the area of slots liners, slot wedges, slot dividers, conductors and conductor impregnations and insulations.

The drawback of conventional magnetic wires is that because of the round shape cross sections of the strands and the wires, the fill factors of the grouped wires are always limited considerably and less than one. Comparing to windings with higher fill factors, with the same total slot

area and total current passing through, the ones with smaller fill factors lead to higher current densities  $J$  but smaller conductor volume  $V$ , hence higher winding losses according to the equation  $P = J^2 \rho_e V$ .

Therefore, increasing the fill factor of windings is one of the solutions to decrease losses, hence enhance the heat transfer performance. The electric machines with hairpin windings designed by Remy International Inc. are good examples of using the above theory. Figure 2.2 [10] shows that the hairpin windings are more compact than the conventional round wire windings.



Figure 2.2 Conventional round wire winding (left) compare to hairpin winding (right)

As discussed above, the hairpin conductors have the advantage of high fill factor because of the rectangular shape of the wire. However, it has a risk of high skin effect and proximity effect when AC current is applied, hence higher losses is introduced.

Laminated winding technique is one of the ongoing projects in our department at Lund University and studied in the SuperCool project<sup>2</sup>. Instead of a common round wire winding or rectangular hairpin winding, a laminated coil is formed by multiple layers of thin electrically conductive materials, each having an insulating layer on one side and being shaped in

---

<sup>2</sup> SuperCool project is financed by Volvo Powertrain AB and Fordonsstrategiska Forskning och Innovation (FFI) and cooperated with Lund University (2013-now).

a specialized pattern [11]. Figure 2.3 [12] shows laminated core segment that is suitable for laminated winding and a laminated winding inside a moulded core half.



Figure 2.3 Laminated core segment (left) and laminated wave winding (right)

As discussed in [12], the laminated windings in Figure 2.3 have fill factor as high as 80% and above. Compared to other winding structures, besides high fill factors, applying laminated winding also brings the possibility to have better forced convection between windings because of the gap between every two winding lamination layers.

### Soft magnetic materials

As discussed in 2.1, core losses take a certain ratio in the total motor losses. There are several techniques used to decrease the losses and improve the heat transfer performances of electrical motors.

- **Lamination core material**

Generally speaking, increasing the amount of silicon significantly increases the electrical resistivity of the steel which decreases the eddy currents and narrows the hysteresis loop of the material, and thus reduces the core losses. On the other hand, the material with higher amount of silicon has the lower thermal conductivity and it can cause difficulties with heat dissipations from laminations and as a result, winding and permanent magnet segments.

Table 2.1 shows the typical losses for different types of electrical steels from Surahammars Bruk AB. It can be noticed that for a certain type of electrical steel, the typical losses are increased with the increase of frequency and magnetic fields. Besides, typical loss is increased when the thickness of the sheet increases. Furthermore, for the steels have the same thickness, the typical



losses can be different because of the different alloy contents, coating manners and manufacture process and so on.

Table 2.1 Typical losses for different types of electrical steels

Type	Thick-ness [mm]	$\hat{j}$ [T]	W/kg at 50 Hz	W/kg at 100 Hz	W/kg at 200 Hz	W/kg at 400 Hz	W/kg at 1000 Hz	W/kg at 2500 Hz
<b>M210-27A</b>	0.27	0.1	0.02	0.04	0.07	0.17	0.72	2.97
		0.5	0.28	0.66	1.50	3.84	14.6	59.1
		1.0	0.86	2.04	4.92	13.1	52.7	235
		1.5	2.04	4.92	11.7	31.4	134	
		1.8	2.37					
<b>M235-35A</b>	0.35	0.1	0.02	0.04	0.08	0.19	0.93	3.98
		0.5	0.29	0.71	1.78	4.73	18.5	76.7
		1.0	1.10	2.75	7.19	20.3	88.3	
		1.5	2.25	5.54	14.4			
		1.8	2.94					
<b>M310-50A</b>	0.5	0.1	0.03	0.05	0.12	0.34	1.62	6.31
		0.5	0.40	0.97	2.56	7.14	29.7	128
		1.0	1.23	3.19	9.07	27.4	130	695
		1.5	2.83	7.31	21.1	68.5		
		1.8	3.86					
<b>M600-50A</b>	0.5	0.1	0.04					
		0.5	0.78					
		1.0	2.34					
		1.5	5.17					
		1.8	7.06					

Note:  $\hat{j}$  represents the peak magnetic polarisation in Tesla.

- **Powder materials**

The base of the soft magnetic composite (SMC) material and soft magnetic mouldable composite (SM<sup>2</sup>C) material is an iron powder of high purity and compressibility. The powder particles are bonded with a coating of an organic material, which produces high electrical resistivity. The coated powder is then pressed into a solid material using a die and finally heat treated to anneal and

cure the bond. [13]

Since the iron particles are insulated by the surface coating and adhesive, which is used for composite bonding, the eddy current loss is much lower than that in laminated steels, especially at high frequencies. The total loss is dominated by hysteresis loss, which is higher than that of laminated steels due to the particle deformation during compaction. On the other hand, the powder core has lower mass density and thus a lower magnetic permeability compared to a laminated core.

The pressing force on SMC during the production procedures will influence the specific losses of the soft magnetic materials. According to the research of Technical University of Cluj-Napoca presented in [13], for the SMC with the similar compositions, the lowest magnetising current are obtained at the lowest pressing force. However, the lowest specific losses at the same frequency level are obtained from the material with highest pressing force.

### **Impregnation materials**

Heat generated by windings contributes a big part in the total heat generation of electrical machines. Therefore, removing the heat from windings effectively can also enhance the heat transfer for machines. The heat generated in the winding active part and end part has different thermal paths to dissipate the power losses. The heat generated in winding active part is able to be conducted to the stator teeth and stator yoke, and then through a certain thickness of contact resistance to the housing and ambient. It can also be conducted between coils if more than one layer of coils are implemented. The heat generated by the winding end part has the conduction or convection path (depending on the movement of the motor's inner air) to the motor's inner air, then to other parts of the machine.

Some research has been done on strengthening the end winding heat transfer paths. Different winding impregnation materials have been studied but the idea is the same, which is to replace the poor thermal conductivity air and winding varnish by better thermal conductivity impregnation materials between the winding end part and machine housing. One of the frequently used materials is epoxy encapsulated material. A study carried out by Kungliga Tekniska Högskolan (KTH) found one silicone based thermally conductive material (SbTCM) with better thermal conductivity

than Epoxy material. [14] shows the thermal conductivity differences between normal varnish  $0.25 \text{ W/m} \cdot \text{k}$ , Epoxy  $0.8 \text{ W/m} \cdot \text{k}$  to  $1 \text{ W/m} \cdot \text{k}$  and SbTCM  $3.2 \text{ W/m} \cdot \text{k}$ . Therefore the lowest steady state temperatures are observed in the motor using SbTCM comparing to the motors using normal varnish and epoxy. Figure 2.4 shows one application example of using SbTCM between the winding end part and machine housing.

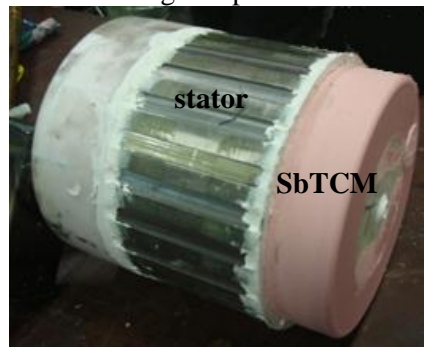


Figure 2.4 Application example of SbTCM (pink) between winding end part and housing (not shown) in electric machine

### Phase-change material

Depending on the threshold temperatures, a phase-change material can change status between solid, liquid and gas while releasing or observing a large amount of energy, and therefore it is able to be used as an effective coolant.

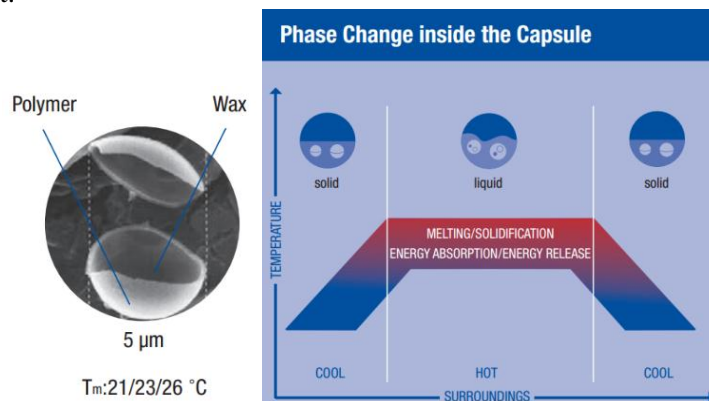


Figure 2.5 Micronal® PCM inside the polymer capsule (left) and its threshold temperatures (right) [15]

As shown in Figure 2.5, Micronal® PCM wax is contained in a 5  $\mu\text{m}$  polymer capsule. When there is a rise in temperature above a defined temperature threshold (21, 23°C or 26°C), the wax absorbs the excessive heat energy and stores it in phase change [15]. When the temperatures fall below the threshold, the wax releases the energy and changes the phase from liquid to solid again. This material is used for intelligent temperature management for buildings.

Another example of using phase-change material for cooling purpose is the 3M™ Novec™ Thermal Management Fluids. [16] shows various coolants with boiling points from 34°C to 131°C. These fluids are applied for immersion cooling of electronics.

As discussed before, phase-change materials have been utilized in cooling of architectures and electronics. Using the right phase-change materials with suitable threshold temperatures could be an effective way to improve the cooling of electric machines.

### **Forced cooling**

Besides improving winding techniques and material thermal properties, forced cooling is also commonly used in highly loaded electrical machines to improve their heat transfer performances. As discussed in [17, 18], the applied forced cooling approaches for electric machines on the market include internal or external cooling fan, liquid cooling methods such as spiral grooves and zigzag arrangements of axial covered channels and oil spray cooling at end windings.

As discussed before, enhancing the heat transfer at winding end part leads to better heat transfer performance of the electrical machines. One way is to use impregnation materials with better thermal conductivity. The other way has been studied is the oil spray cooling applied to the winding end part in order to increase the convective heat transfer capabilities.

According to [19], Toyota has successfully implemented the oil spray cooling approach in the electric machines used by Prius. [20] shows that Oak Ridge National Laboratory has verified the solution and come to a conclusion that ‘the cooling was significantly improved compared with oil-sling cooling systems’. Figure 2.6 [20] shows the oil spray nozzles inside an electric motor.



Figure 2.6 Spray nozzle locations inside motor housing [20]

### 2.3 Indirect cooling and direct cooling

As mentioned above, except for the end winding cooling, liquid cooling methods include water or oil cooling with spiral grooves or zigzag arrangements of axial covered channels inside housing. These forced liquid cooling methods indeed improve the heat transfer performance of electric machines comparing to machines with natural convections only. However, these forced cooling channels drilled inside housings leads to uncertain contact resistance air pocket and a small layer of housing aluminium between the coolant and the stator. Besides, due to different thermal expansion rates of stator iron and housing aluminium, bigger air pocket can be obtained between housing and stator at high temperatures. Because of the relatively low thermal conductivity of air, heat generated from the inside of the machine is hard to be conducted to the coolant in the housing or to the ambient. Therefore the direct cooling concept is proposed in order to remove the uncertain air pocket between the housing and stator. Direct cooling means that the coolant directly contacts with the stator back. Figure 2.7 shows the conceptual figures of the traditional liquid cooling i.e. indirect cooling (left), and the direct cooling (right). Compared to indirect cooling, the direct cooling concept moves the cooling circuits closer to the heat source and sometimes overlapping with the heat source.

In the direct cooling system, the coolant directly contacts with the stator back, hence oil rather than water is preferred to avoid corrosion. This is also an advantage of using oil cooling when electrical motor and reduction gear of a hybrid vehicle share the same housing. Therefore it is easy to employ in the lubricant oil in the reduction gear as the coolant for the

electrical machine. Figure 2.8 shows the machine with indirect (left) and direct (right) cooling system, separately, and also the reduction gear sharing the same oil tank.

The enhancement of heat transfer performances by engaging direct cooling system compared to using indirect cooling system for the same electrical machine are studied in this project.

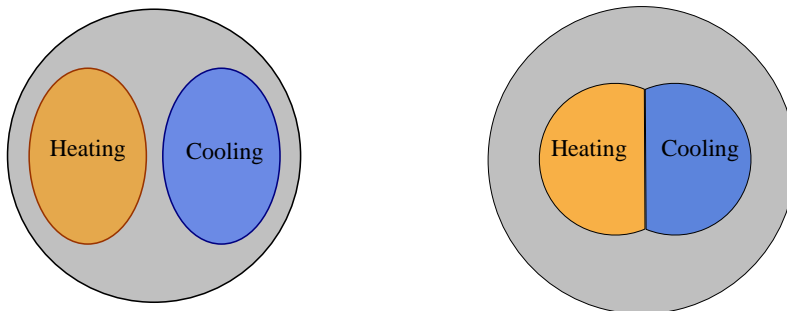


Figure 2.7 Separated heating and cooling circuits (left) and attached heating and cooling circuits

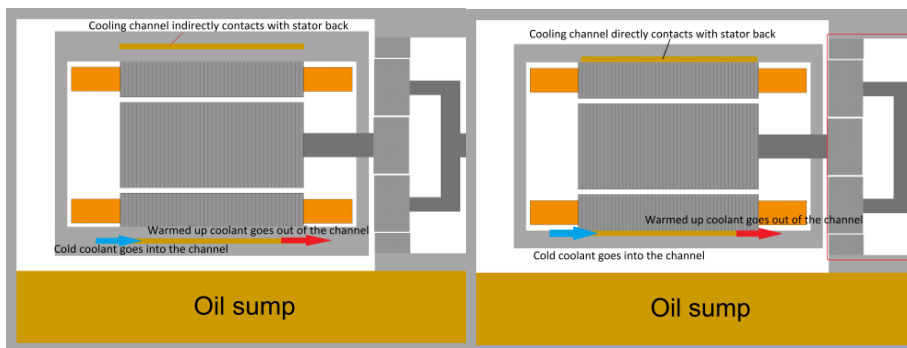


Figure 2.8 Electric machines with indirect (left) and direct (right) cooling system designs

## 2.4 Summary

In this chapter the basics on heat transfer theory and different techniques to enhance the heat transfer of electric machines have been described. As it

---

is discussed before, some of the suggested approaches belong to the category of ‘decreasing the heat generation’, such as hairpin windings, thin core lamination materials and powder soft magnetic materials. Some of the suggested methods belong to the category of ‘improving the heat dissipation path’, such as high thermal conductivity impregnation materials, oil spray cooling, phase-change materials, indirect and direct cooling. Lamination winding technique covers both categories because of the high fill factor, hence low generated losses and at the same time the possibility of increasing the heat convection between laminated windings. The enhancement of heat transfer performances by engaging direct cooling system compared to using indirect cooling system for the same electrical machine are further studied in this project.





## **Chapter 3**

### **Design of Cooling Circuits**

This chapter discusses the design procedures of cooling circuits implemented for electrical machines. The aim of the cooling circuit design is to obtain the cooling ducts with the best cooling performance within limited space and pumping power.

Firstly, the electrical machine used in the study, i.e. the cooling object, is introduced. Secondly, the cooling medium is discussed and its properties are presented.

Thereafter, the major discussions on the implemented design methods of the cooling circuits are presented. Computational Fluid Dynamics (CFD) approach and Hydraulic Equivalent Circuit (HEC) approach are the two approaches used for designing the cooling system. CFD simulations are used for conjugated calculation including both fluid dynamics and heat transfer calculations. However, CFD requires a high resolution mesh leading to long computing time. Hence, in this study, the conjugated CFD simulation is implemented only for a simple geometry considering single channel. Then HEC approach is applied to evaluate fluid distributions and pressure drop of the whole cooling system. These two methods are combined with each other in order to fulfil the design requirements. Based on the calculation results combined with the manufacturing requirements, the final designs are elected.

#### **3.1 Cooling object**

The electric machine designed in the Green Car project is chosen as the cooling design target in this project. The initial machine design and the improved machine design are presented in [21] and [22], separately. Both of the designs are supposed to be implemented in a parallel hybrid vehicle

without plug-in capabilities for an Electrical Rear Wheel Driven (E-RWD) unit. Besides, the designed machine should be enclosed in a cylinder of 214 mm diameter and 160 mm length including the end windings [22] and the DC-link voltage of the drive is set to 300 V [21].

For the initial designed machine, the traction motor power is limited to 12 kW continuous and 30 kW peak. With a field weakening ratio selected to 1:5 and a maximum speed of 15000 rpm @ 150 km/h and the nominal torque is 40 Nm @ 3000 rpm and the peak torque 100 Nm [21, 22].

Both the experimental tests and the FEA simulations show that the maximum torque of the initial designed motor cannot exceed 100 Nm because of magnetic saturation in the stator core. Therefore, in the redesigned machine, the size of stator slots is decreased hence increasing the size of stator laminations to avoid the early saturation in the stator. The nominal torque for the redesigned machine with natural convection is 30 Nm @ 4550 rpm, and the peak torque 127 Nm, which combined give a nominal power of 14.3 kW to be compared to the original machine at 12 kW [22].

### 3.2 Cooling medium

In the direct cooling system, the coolant contacts directly with the stator back, hence oil rather than water is preferred to avoid corrosion. In addition, the electrical motor in a hybrid vehicle is mounted inside or in contact with a gearbox. As it is shown in Figure 2.8, the reduction gear is applied to reduce the high speed of a high power density electric motor so that the power produced can be transferred to the wheels, with the added benefit of torque amplification. When the electrical motor and reduction gear share the same housing, it is easy to employ in the lubricant oil in the reduction gear as the coolant for an electrical machine [17]. Table 3.1 shows the properties of coolant applied in the CFD simulations.

Table 3.1 Coolant properties

	Statoil Transway S
Density [kg/m <sup>3</sup> ]	852
Viscosity @40°C [mm <sup>2</sup> /s]	35.2
Viscosity @100°C [mm <sup>2</sup> /s]	8.05
Thermal conductivity [W/(m K)]	0.12~0.2

### 3.3 CFD theory

#### Why CFD

CFD is fundamentally based on the governing equations of fluid dynamics. They represent mathematical statements of the conservation laws of physics. [23] The concerned governing equations used by CFD calculations and their physical meanings are discussed in the following sections.

In general, CFD is mainly used to compute the fluid dynamics and can include heat transfer. Three physical laws are adopted by CFD calculations [23]:

- Mass is conserved for the fluid.
- Newton's second law, the rate of change of momentum equals the sum of forces acting on the fluid.
- First law of thermodynamics, the rate of change of energy equals the sum of rate of heat addition to the rate of work done on the fluid.

As it is presented by [24, 25, 26], CFD has the advantage that it can be used to predict fluid flow in complex regions, while FEA heat transfer analysis can only be used to model conduction heat transfer in solid or non-solid components with the limitation that the fluid dynamics is not in the focus and the heat transfer coefficient at the boundaries between solid and moving fluid has to be provided by other approaches, for instance, empirical numerical equations. This difference is because that FEA heat transfer analysis does not involve solving the mass conservation and Navier-Stoke equations and FEA is thus not able to predict the velocities or pressures in fluid domains, thereafter, the temperature evolution in the domains. This difference is examined in detail in the following parts on CFD theories.

#### Why partial CFD

Considering the size of the problem, there are two different ways of using CFD tool for electrical machines thermal analysis. The first choice is to simulate the heat paths of whole machine including convections at the interfaces of fluid and solid regions and conductions in all solid parts.

Under this circumstance, CFD is often used to evaluate the accuracy of FEA or lumped parameter calculations. However, including solid regions in a CFD analysis prolonged preparation by increasing the complexity of setup [24]. Therefore, it is inefficient to use for designing prototypes, which needs sensitivity studies on various parameters and repeats the simulations for many times.

Another way of using CFD for thermal analysis is to implement CFD on the selected parts of the studied machine to predict the coolant flow rate, velocity and pressure distribution in the coolant or surrounding the machine, as well as heat transfer coefficients at the fluid-solid interfaces, which are applied in the subsequent temperature analysis in the remaining solid structures by FEA or lumped parameter thermal model. Based on the previous review of the difference between CFD and FEA on heat transfer analysis, it is easy to understand that for FEA thermal analysis, one of the most challenging issues is to determine accurately the heat transfer coefficients at the interfaces between the solid and fluid. By the conjugation of CFD simulations and FEA simulations, the time spending on mesh, solving and sensitivity study by CFD becomes short, and the accuracy of FEA is improved.

With the concern of computational cost, the CFD can sometimes be replaced with the known empirical/experimental expressions or data on fluid dynamics and heat transfer. The main concern on the thermal design and selection on the computation tool for that relies on cooling channels. Taking a closer look into the cooling channels one can distinguish the shape of the cross section area of the channel that is perpendicular to the coolant flow and the profile or the path of the channel along the flow direction. Focusing on thermal design and selection of cooling system, [24, 27, 28] present different equations and curves of calculating the heat transfer coefficients for various cross section shapes of cooling channels. However, most of them are obtained empirically for fluid in fully developed hydraulic and heat regions (the definition of *fully developed* and *entry region* are explained in the following **theory** part). Some research is done on investigating the heat transfer for the thermal entry (defined by Equation 3.9) regions but for very few specific shapes. On the other hand, the parallel cooling ducts with coolant flowing along axial direction are chosen to ease the manufacture process comparing to spiral cooling channel surrounding the machine. Therefore each paralleled longitudinal

cooling channel has the length approximately 80 mm because of the restriction by the length of the electric machine, which is relatively short and leads to big influences by the entry regions. Hence, there is not only focus on shaping the longitudinal parallel cooling channels but also the inlet and the outlet in and out from the channels. Still the problem can be solved by parts. Therefore CFD applied on parts of the machine offers possibilities to investigate accurately and flexibly on heat transfer coefficients at the solid and fluid interfaces with consideration of entry region effects.

### Theory

The first physical law obeyed by any CFD calculation is the mass conservation law. It states that the amount of fluid entering a control volume must equal to the amount of fluid coming out. In the Cartesian coordinate system, it can be expressed as

$$\frac{\partial \rho}{\partial \tau} + \frac{\partial(\rho u)}{\partial x} + \frac{\partial(\rho v)}{\partial y} + \frac{\partial(\rho w)}{\partial z} = 0 \quad 3.1[23]$$

where  $u$ ,  $v$ ,  $w$  are the local velocity components in the flow field,  $x$ ,  $y$ ,  $z$  are the locations in Cartesian coordinate system,  $\tau$  is time and  $\rho$  is the fluid density. If constant density and two dimensional CFD analysis is considered, Equation 3.1 is simplified as

$$\frac{\partial u}{\partial x} + \frac{\partial v}{\partial y} = 0 \quad 3.2$$

According to Equation 3.2, if the velocity  $u$  along  $x$  direction is increasing, i.e. positive  $\partial u/\partial x$ ,  $\partial v/\partial y$  must be negative to fulfil the mass conservative law, which means that the velocity  $v$  along  $y$  direction is decreased.

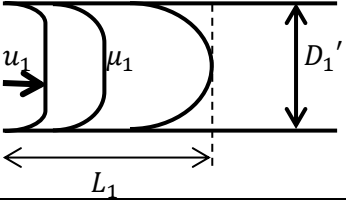
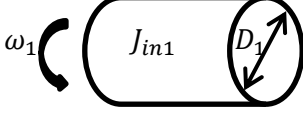
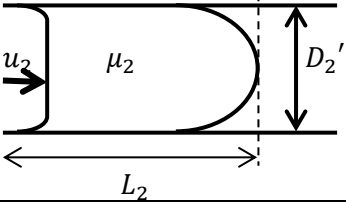
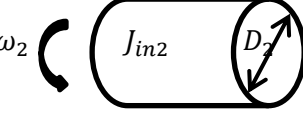
The second import equation solved by CFD simulations is the momentum equation which describes the force balancing on the fluid mass. For a two dimensional case, the momentum equations in each direction in Cartesian coordinate system can be written as [23]

$$\rho \frac{\partial u}{\partial \tau} + u\rho \frac{\partial u}{\partial x} + v\rho \frac{\partial u}{\partial y} = -\frac{\partial p}{\partial x} + \mu \frac{\partial^2 u}{\partial x^2} + \mu \frac{\partial^2 u}{\partial y^2} \quad 3.3$$

$$\underbrace{\rho \frac{\partial v}{\partial \tau}}_{\text{Local acceleration}} + \underbrace{u\rho \frac{\partial v}{\partial x} + v\rho \frac{\partial v}{\partial y}}_{\text{Advection}} = \underbrace{-\frac{\partial p}{\partial y}}_{\text{Pressure gradient}} + \underbrace{\mu \frac{\partial^2 v}{\partial x^2} + \mu \frac{\partial^2 v}{\partial y^2}}_{\text{Diffusion}} \quad 3.4$$

where  $p$  is pressure and  $\mu$  is the dynamic viscosity. As it is marked in the Equation 3.4, the momentum equation contains the local acceleration term, advection term, pressure gradient term and diffusion term. At the steady state, velocity is not changing with time, i.e. local acceleration term is zero.

Table 3.2 Analogy between fluid mechanism and machine rotation

Fluid mechanism	Machine rotation
	
	
<p>If <math>u_1 = u_2</math>, <math>\rho_1 = \rho_2</math>, <math>p_1 = p_2</math>,  <math>D_1' = D_2'</math>, <math>\mu_1 &gt; \mu_2</math>, then <math>L_1 &lt; L_2</math></p>	<p>If <math>\omega_1 = \omega_2</math>, <math>J_{in1} = J_{in2}</math>,  <math>F_1 = F_2</math>, <math>D_1 = D_2</math>, <math>f_1 &gt; f_2</math>,  then <math>N_{rot1} &lt; N_{rot2}</math></p>

Comparing the fluid momentum phenomenon to a rotating electrical machine, the advection term in Equation 3.3 and 3.4 is analogous to machine inertia, the pressure term is analogous to applied force and the diffusion term is analogous to the friction. Table 3.2 shows the analogy

between fluid mechanism and the kinetics of a rotating machine. The pictures in the left column show the comparison between two types of fluid materials with different dynamic viscosity  $\mu$  but the same density  $\rho$ , inlet velocity  $u$ , and pressure  $p$ , flowing through identical sized pipes ( $D_1' = D_2'$ ). According to Equation 3.3 and 3.4, case 1 (shown by the left top picture in table 3.2) with higher dynamic viscosity  $\mu_1$  leads to a higher diffusion term, i.e. higher friction, therefore a faster transition to a *fully developed flow* region with shorter *hydrodynamic entry length*  $L_1$ . Flow development is related to the change of speed gradients along  $x$  and  $y$  directions according to eq. 3.2 and is considered fully developed when the change along the flow direction remains the same. Comparing to the fluid mechanism on the left column, the two pictures on the right column illustrates the analogical machine rotation scenarios. These pictures show two identical sized electrical machines ( $D_1 = D_2$ ) with the same inertia  $J_{in}$  and applied force  $F$  but different friction factors  $f$ . Therefore, the one with bigger friction factor  $f_1$  will take less number of rotations  $N_{rot1}$ , i.e. shorter rotational distance to reach the constant speed.

The velocity profile along the fluid flow direction in a pipe is shown in the left column of table 3.2. When the hydraulic boundary layers from top and bottom walls merge at the centreline, therefore the velocity profile forms a parabolic curve, the fluid is fully developed. The distance from the tube inlet to the position where the friction coefficient reaches within about 2 percent of the fully developed value [8] is defined as *hydrodynamic entry length*, for instance,  $L_1$  and  $L_2$  in table 3.2.

As discussed in [8, 27, 28], for internal fluid flow with laminar flow, the hydrodynamic entry length can be calculated by:

$$L_{h,laminar} \approx 0.05Re \cdot D_h \quad 3.5$$

where  $Re$  is the Reynolds number and  $D_h$  is the hydraulic diameter. For laminar flow in ducts,  $Re$  is less than 2300 [8]. The Reynolds number is defined as

$$Re = \frac{\rho \mathcal{V}_m D_h}{\mu} = \frac{\mathcal{V}_m D_h}{\nu} \quad 3.6$$

where  $\mathcal{V}_m$  is the mean fluid velocity in flow direction,  $\mu$  is the dynamic viscosity and  $\nu$  is the kinematic viscosity which is equal to  $\mu/\rho$ . The

hydraulic diameter  $D_h$  is defined as

$$D_h = \frac{4A_c}{p_c} \quad 3.7$$

where  $A_c$  is the cross section area of the duct and  $p_c$  is its wetted perimeter.

Thermodynamic equation is involved if the heat transfer calculation is included in the CFD analysis. The thermodynamic equation in a Cartesian coordinate system with three dimensions is expressed as

$$\underbrace{\frac{\partial T}{\partial \tau}}_{\text{Local acceleration}} + \underbrace{+u \frac{\partial T}{\partial x} + v \frac{\partial T}{\partial y} + w \frac{\partial T}{\partial z}}_{\text{Advection}} = \underbrace{\frac{\lambda}{\rho c} \left\{ \frac{\partial^2 T}{\partial x^2} + \frac{\partial^2 T}{\partial y^2} + \frac{\partial^2 T}{\partial z^2} \right\}}_{\text{Diffusion}} + \underbrace{\frac{Q'}{\rho c}}_{\text{Internally generated heat}} \quad 3.8$$

The meaning of each symbol can be found from the previous discussions and also from the symbol list. Comparing to Equation 2.2, this equation contains the advection term which enables the CFD analysis to involve the fluid velocities into the temperature evolution process. Meanwhile, the fluid velocities are obtained by solving the previous mass conservation (Equation 3.1) and the Navier-Stokes equations (Equation 3.3 and 3.4).

Equation 3.3, 3.4 and Equation 3.8 show great similarities between the fluid dynamic analysis and thermodynamic analysis, though the studied objects and the unknowns to be solved are different. For the fluid dynamic analysis, the studied object is the velocity or pressure. While for thermodynamic analysis, the studied object is the temperature. However, both sets of equations contain the local acceleration term, advection term and diffusion term which indicate the studied objects changing with time  $\tau$ , velocities, and diffusion factors. Therefore, comparing to the *hydraulic entry length* in fluid dynamic study, there is *thermal entry length* in heat transfer analysis, which can be calculated by [8]

$$L_{th,laminar} \approx 0.05 Re \cdot D_h \cdot P_r \quad 3.9$$

where  $P_r$  is the Prandtl number which is defined as



$$P_r = \frac{c\mu}{\lambda} = \frac{\text{viscous diffusion}}{\text{thermal diffusion}} \quad 3.10$$

where  $c$  is the specific heat,  $\lambda$  is the thermal conductivity, and  $\mu$  is the dynamic viscosity.  $P_r$  indicates the ratio between the fluid flow developing speed and heat transfer developing speed. For the fluid with  $P_r$  larger than 1, for instance oil or water, indicates that the viscous diffusion is dominating comparing to thermal diffusion, therefore a faster transition of hydraulic fluid development, hence shorter hydraulic entry length than thermal entry length.

The above three sets of partial differential equations (PDE) Equation 3.3, 3.4 and Equation 3.8 are used for numerically solving the fluid dynamic problems. These are enough to predict the flow velocity, pressure and temperature in fluid and solid regions if the studied flow is laminar. More PDEs need to be involved if the studied flow is turbulence, which are not included in this study.

### 3.4 CFD geometry and boundary conditions

As discussed before, partial CFD simulation method is used in the following studies. However, based on different study purposes, two groups of partial CFD simulations are focused. The first CFD simulation is carried out with the ambition of predicting the differences on the cooling effects between the direct cooling system and indirect cooling system. The focus is on the single rectangular cooling channel in the machine housing and the adjacency to the electrical machine. Therefore solid geometries including electric machine housing and part of the stator combined with fluid coolant are considered in the simulations. Thereafter the temperature distributions at the interfaces between the housing and stator are studied.

The second CFD simulation takes place with the ambition of evaluating heat transfer coefficients of pipe walls with different cross section areas of the pipe and different fluid properties including both fluid developing and fluid developed regions. Therefore only the fluid region with walls is studied in order to compare the heat transfer capabilities for different cooling channel designs and also create the heat transfer coefficient maps for future usage.

Figure 3.1 shows the section view of the electric machine stator core and the housing with paralleled cooling channels made in the axial direction. For both direct and indirect cooling systems, the cooling of the end winding parts is identical. In order to compare, the cooling channels covering the active winding length, i.e. axial stator length, are selected in these CFD models [17]. Besides, the partial CFD calculations are done based on the assumption that the coolant flow is distributed evenly in each of the paralleled channels. Therefore, the heat transfer performance at one channel is assumed to be identical to the others. Hence, one cooling channel is selected as the calculation domain and represents the rest of the cooling channels.

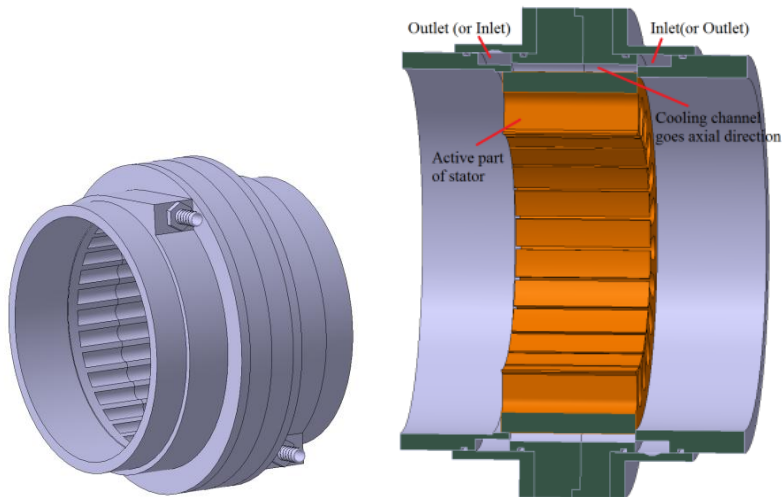
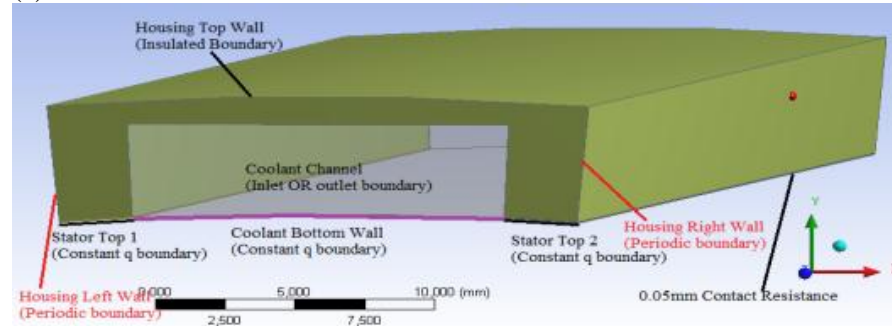


Figure 3.1 Section pictures of housing with cooling grooves

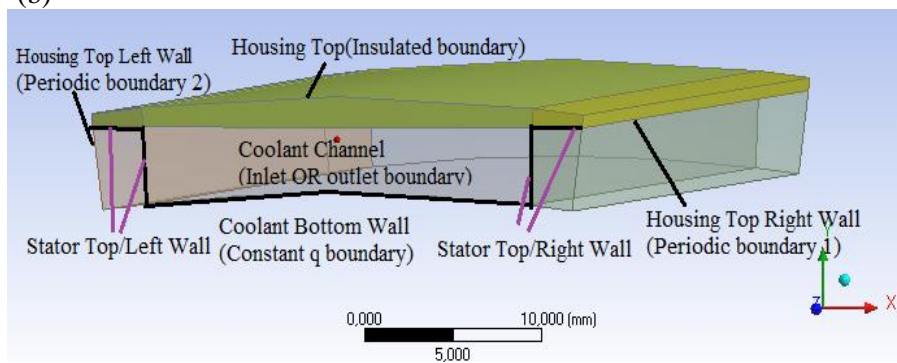
Figure 3.2 shows the geometries and boundary conditions applied in the first group of CFD simulations with the purpose of comparing the cooling effects between direct and indirect cooling systems. The *indirect* cooling includes cooling channels inside the housing and the challenging thermal contact between the stator back and the housing. Alternatively, the *direct* cooling means that the coolant directly contacts with the stator back. In order to make a direct contact between the coolant and the stator back, two approaches are utilized to make the grooves: (1) grooves in the housing (Figure 3.2-a); (2) grooves in the stator back (Figure 3.2-b) [17]. Figure

3.2-c shows the geometry and boundary conditions for housing with indirect cooling channels.

(a)



(b)



(c)

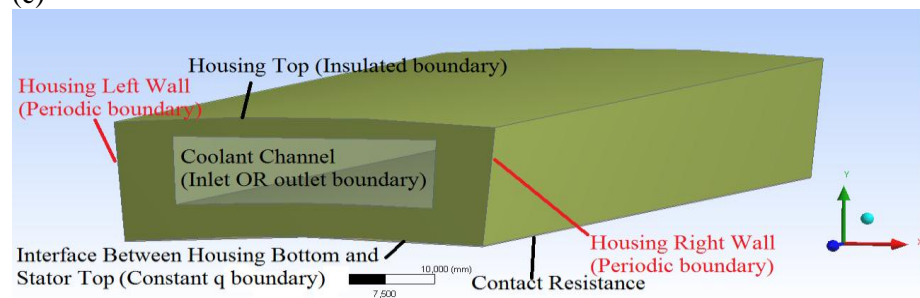


Figure 3.2 Boundary conditions of CFD simulations with rectangular ducts, direct cooling ducts in housing (a), direct cooling ducts in stator (b), Indirect cooling ducts (c)

As shown in Figure 3.2, all the boundary conditions are specified. In the following expressions,  $u$ ,  $v$  and  $w$  represent the velocity in  $x$ ,  $y$  and  $z$  directions, separately.

- Inlet

Fluid region:

$$u = v = 0, w = \text{constant}, T = T_{in} = 25^{\circ}\text{C}$$

Solid region:

$$u = v = w = 0, \partial T / \partial z = 0$$

- Outlet

Fluid region:

$$\partial u / \partial z = \partial v / \partial z = \partial w / \partial z = \partial T / \partial z = 0$$

Solid region:

$$u = v = w = 0, \partial T / \partial z = 0$$

- Housing Top:

In order to compare the cooling effects of the forced cooling approaches, natural convection on the housing top is eliminated, i.e. housing top is thermally insulated, thus the heat transfer coefficient there is zero.

- Boundaries at housing left and right wall (periodic)

$$u = v = w = 0, \partial T / \partial z = 0$$

- Boundary condition at the interface between the housing bottom and stator top (constant  $q$ ):

$$q = \text{constant}, u = v = w = 0$$

For the interior boundaries, there is no need to specify the boundary conditions in FLUENT<sup>3</sup> since the ‘coupled’ boundary conditions will be applied automatically with a conjugated mesh.

The heat transfer coefficient at a specific channel surface is calculated by

$$h_f = q_s / \Delta T \quad 3.11$$

where  $q_s$  is the wall average heat flux and  $\Delta T$  is the mean temperature difference.

$$\Delta T = T_s - T_{vf} \quad 3.12$$

where  $T_s$  is the wall average temperature by integrating the temperature over the duct wall and  $T_{vf}$  is the flow average temperature by integrating the temperature over the investigated fluid volume.

For the convenience of comparison, a dimensionless parameter  $\eta$  is defined as

$$\eta = (T_{ave} - T_{in}) / T_{in} \quad 3.13$$

where  $T_{ave}$  is the average temperature obtained by integrating the temperature over the interface between the housing bottom and stator top and  $T_{in}$  is the coolant inlet temperature which is constant 25°C.

In order to obtain the best cooling effect with the lowest cost for the both direct and indirect cooling approaches, the second group of CFD simulations is carried out to characterize the effect of cooling when using different shapes of forced cooling channels which helps the designers to choose the suitable channel if the forced cooling method is applied. The cross-section configurations of the three different shapes are shown in Figure 3.3.

---

<sup>3</sup> FLUENT is a registered trademark of the ANSYS. Inc, United State.

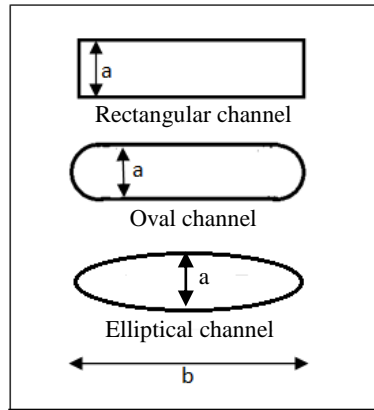


Figure 3.3 Cross-section configuration of three different cooling channels

The height width ratio  $\vartheta$  is defined as

$$\vartheta = a/b \quad 3.14$$

where  $a$  is the height and  $b$  is the width of the channel cross section.

Generally speaking, if no forced cooling approaches are applied to the end winding, the majority of the heat is dissipated (refer to Figure 2.1) by conduction to the slots, stator, housing and finally by convection and radiation to the surrounding air. With the forced cooling channels applied in the motor as shown in Figure 3.1, the major portion of the heat generated by the motor is dissipated by convection from the hot walls around the channels in the housing or stator to the coolant. With the aim to characterize these cooling ducts, a simplified model is made by neglecting the solid bodies around the cooling channels. Besides, because of the good heat conduction in the radial direction of the solid (stator and housing), i.e. in the direction perpendicular to the fluid flow direction, the heat flux derivatives are relatively small in this direction. As a result, uniform heat flux  $q$  is applied around the channel walls [18].

### 3.5 Cooling maps

This section presents the results obtained from the previously discussed partial CFD simulations. These results show either the temperature rise of the interface between stator and housing or the heat transfer coefficients from the cooling channel surface. The latter is presented as a map or a two

dimensional function of coolant flow and shaping of different types of channel cross-sections. Some of the cooling maps are later used for the thermal design of electrical machine.

Figure 3.4 plots the relative temperature (Equation 3.13) at the housing and the stator interfaces with different cooling methods (indirect cooled and directed cooled), rectangular channel height and width, which is obtained from the first group of CFD simulations. Besides, the red lines represent cooling channels with 2 mm height and the blue lines cooling channels with 4 mm height. Moreover, the x-axis shows different widths of cooling channels and y-axis shows the percentage of the average temperature rise at the interface between the stator and housing against inlet temperature, which is calculated by Equation 3.13.

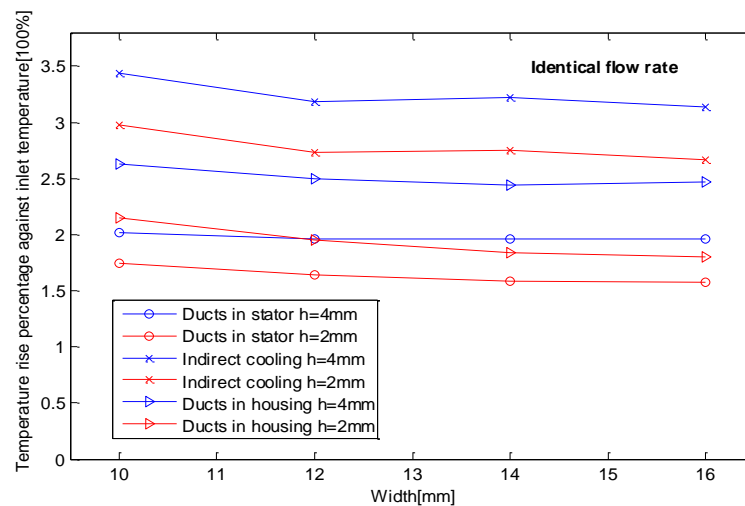


Figure 3.4 Relative temperature at housing and stator interface with different cooling methods, channel height and width

Figure 3.4 shows that when a certain position of cooling channels is chosen, with identical total flow rate and identical height, a wider channel leads to smaller temperature rise, i.e. lower average temperature at the housing and stator interface. In addition, when channel width is fixed, 2 mm height duct leads to smaller temperature rise on stator back compared to the duct with 4 mm height.

Furthermore, when the size of a rectangular channel is fixed, both direct cooling designs, one made in the housing or another in the stator back, show better cooling performances than the indirect cooling system design. For instance, comparing the rectangular channel with the same cross section size 12 mm\*4 mm, but made in different positions: (1) cooling duct is made indirectly contact with stator back as shown in Figure 3.2(c); (2) cooling duct is moved closer to the stator as direct cooling duct shown in Figure 3.2(a), the stator and housing interface temperature of the electrical machine with indirect cooling system shows 320% higher than the inlet temperature, while the stator and housing interface temperature of the machine with direct cooling shows only 260% higher than the inlet temperature. Therefore, the housing and stator interface temperature of the machine has been decreased for app. 18% if compared the machine used direct cooling system to the one used indirect cooling system.

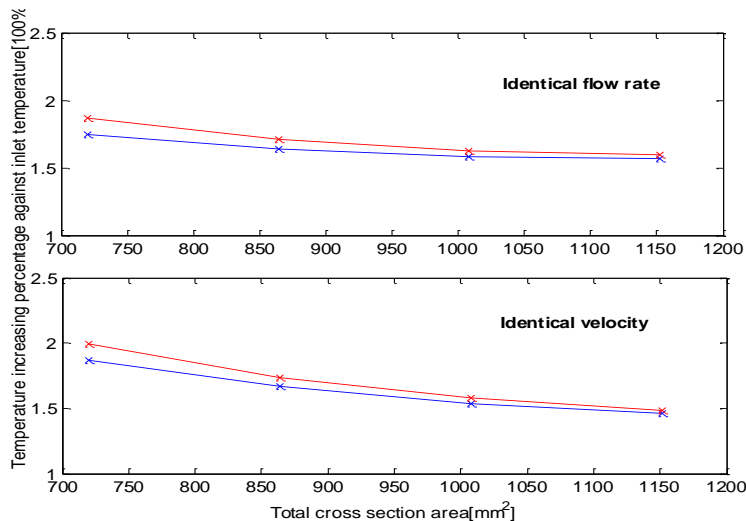


Figure 3.5 Relative temperature rise at the interface between stator and housing for 24 channels and 36 channels



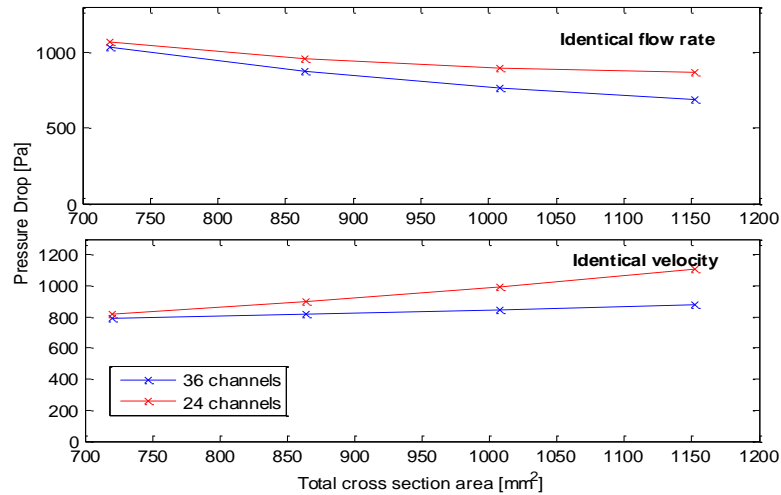


Figure 3.6 Pressure drop for 24 channels and 36 channels

Except for size and position of cooling channels, the number of cooling channels is another design parameter needs to be evaluated. In this study, because of 24 slots in stator is chosen in motor design stage, the 24 channels cooling system is numerically simulated to compare with a 36 channels cooling system. Rectangular channels with height 2 mm made in the stator are chosen for this comparison under identical flow rate or identical velocity. The width of each channel in the 24 channels cooling system is calculated by keeping the same total cross section area as in the corresponding 36 channels cooling system. [17]

Figure 3.5 and Figure 3.6 show that with either identical flow rate or identical velocity boundary conditions, 24 channels cooling system shows a slightly higher average temperature on the interface and a higher pressure drop, which means that, applying the same pumping power, 36 channels system gives better cooling performance than 24 channels system.

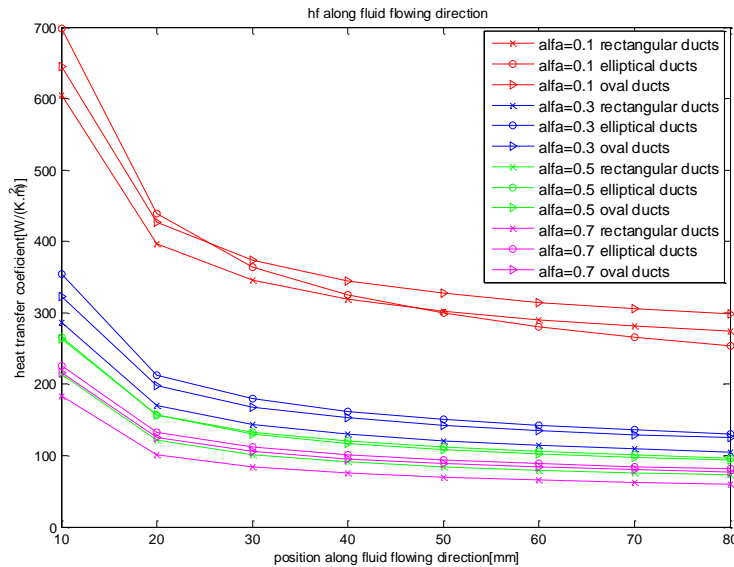
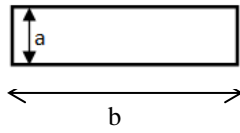


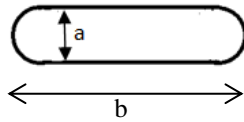
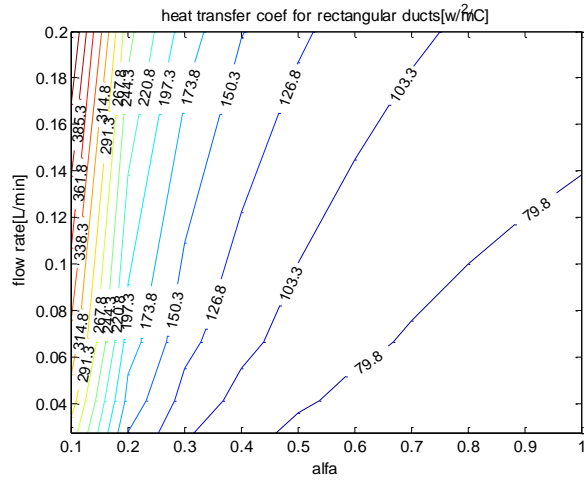
Figure 3.7 Heat transfer coefficient along fluid flowing direction

In Figure 3.7, the average heat transfer coefficients are presented along the fluid flowing direction for the three different shapes of channels. The results are obtained for the cooling system with 15 paralleled channels, total flow rate 1L/min and 'height width ratio' 0.1, 0.3, 0.5 and 0.7, separately. Figure 3.7 clearly shows that the heat transfer coefficient decreases along the fluid flowing direction which is an inherent characteristic of heat convection in the developing region. For 'height width ratio' 0.1, rectangular channel shows slightly bigger heat transfer coefficient than elliptical duct after 50mm position from the inlet. However with 'height width ratio' 0.3, 0.5 and 0.7, elliptical and oval ducts show better heat transfer coefficient than the rectangular ducts. [18]

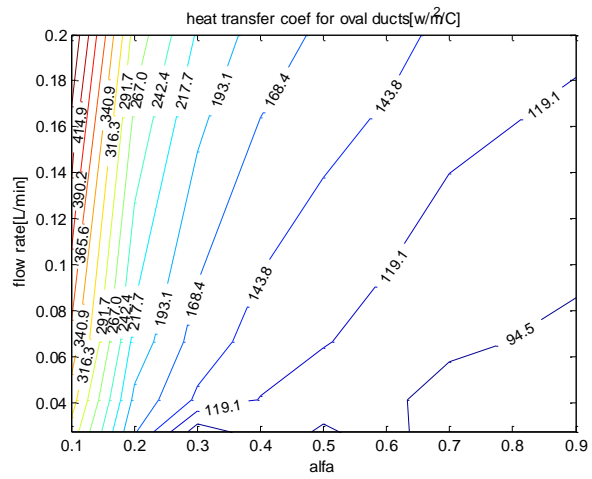
Thereafter, different combinations of flow rate and 'height width ratio'  $\partial$  are investigated in order to have a comprehensive picture of the heat transfer capabilities of cooling channels with the three different cross sections.



$$Nu = Re^{0.262} Pr^{0.387} \delta^{0.113}$$



$$Nu = Re^{0.325} Pr^{0.40} \delta^{0.257}$$



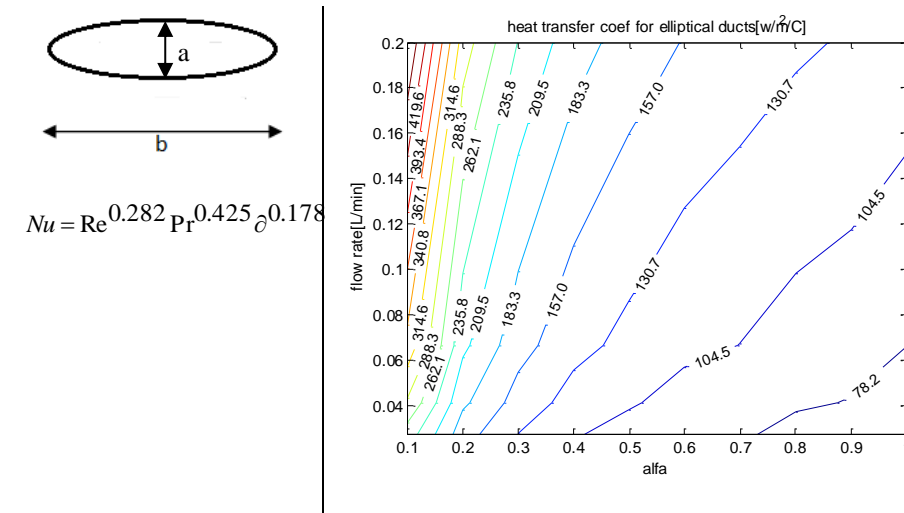


Figure 3.8 Heat transfer coefficients and Nusselt number predicted for three cooling ducts with different cross sections

In Figure 3.8, the left column shows the expression of the dimensionless parameter Nusselt number  $Nu$  versus Reynolds number  $Re$ , Prandtl number  $Pr$  and height width ratio  $\delta$  for three different shaped cooling channels. Reynolds number and Prandtl number are defined by Equation 3.6 and 3.10, separately. Furthermore, the expression of Nusselt number for each channel is obtained with the purpose of generalizing the heat transfer abilities for different shaped cooling channels with different fluid velocities. Besides, heat transfer coefficients can be evaluated from Nusselt numbers by equation

$$Nu = h_f * D_h / \lambda \quad 3.15$$

In the right column of Figure 3.8, the average heat transfer coefficients are plotted with the flow rates in each paralleled channel varying from 0.028L/min to 0.2L/min and the 'height width ratios'  $\delta$  varying from 0.1 to 1. For the three different shaped channels, the average heat transfer coefficient over the whole duct length is big at high flow rate with small 'height width ratio'  $\delta$ . In addition, comparing the three different shaped channels, with identical  $\delta$  and flow rate, the oval channels give better heat transfer coefficients than the elliptical and the rectangular channels in most of the cases. Between the rectangular and elliptical channels, the rectangular channel only shows higher heat transfer coefficient than the

elliptical channel when  $\delta$  is smaller than approximately 0.2 and flow rate is smaller than approximately 0.05L/min. [18]

The following case study of conjugated heat transfer simulations is carried out based on the heat transfer coefficients obtained from partial CFD simulations above.

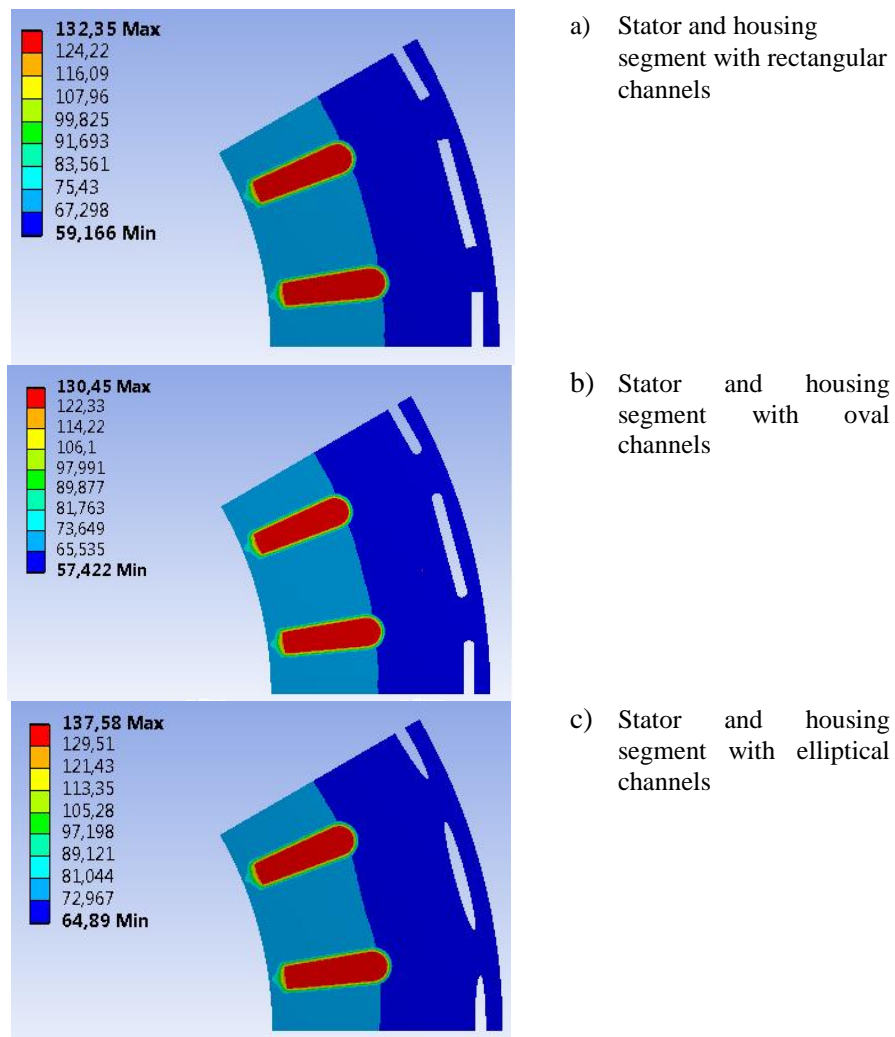


Figure 3.9 Temperature distributions [°C] for stator and housing segment with different shaped channels

In order to compare the different cooling performances caused by different designs of cooling ducts, the three different shaped cooling channels are applied with three identical simplified geometries of windings, insulations, stator and housing. All the three cooling channels have 'height width ratio' 0.1 and flow rate 0.042L/min in each channel. According to [21], the nominal current density of the studied motor is 9A/mm<sup>2</sup> and the motor can operate linearly up to 3 times the nominal current density. Therefore 27A/mm<sup>2</sup> current density is applied in the following thermal analysis.

Figure 3.9 shows the temperature distributions for motor stator and housing segments in Celsius. Comparing the three temperature plots, it is found that the design in case b with oval channels shows the smallest maximum temperature, while the highest maximum temperature appears in the stator and housing segment with elliptical channels in case c.

### 3.6 Hydraulic equivalent circuit (HEC)

The hydraulic equivalent circuit (HEC) is used to evaluate the flow network performances including flow rate distributions and pressure drop estimations for the whole cooling circuit. If one cooling duct is analogous to one resistance, the flow network is analogous to resistances network which are connected in series or parallel. The use of a flow network analysis is to evaluate (1) flow rate distribution, which will influence the heat transfer behavior directly and (2) pressure drop, which is proportional to the cooling system cost.

Besides the HEC method which is discussed in the following parts, the CFD tool is able to accomplish the job of flow network analysis as well. The advantage of using CFD to simulate the flow network is that it can take into account the fluid flowing details, such as tube turning, fluid expansion and contraction, and therefore leads to high accuracy. However, since the flow network analysis needs to involve the whole cooling system with a large number of cooling ducts, the mesh and computing time gets relatively long. Hence, the HEC is proposed in order to build a quick and accurate enough method for flow network analysis that also can be easily implemented on other different designs of cooling system.

References [29-31] present three different ways for the flow network to be analogous to the electric circuit separately. Figure 3.10 from [29] shows one way that how pressure drop is related to flow rate and hydraulic

resistance by equation  $\Delta P = R^2 Q^2$ . [29] also points out that if fluid flow is known to be laminar, then a relation that the pressure drop is proportional to the flow rate may be more appropriate.

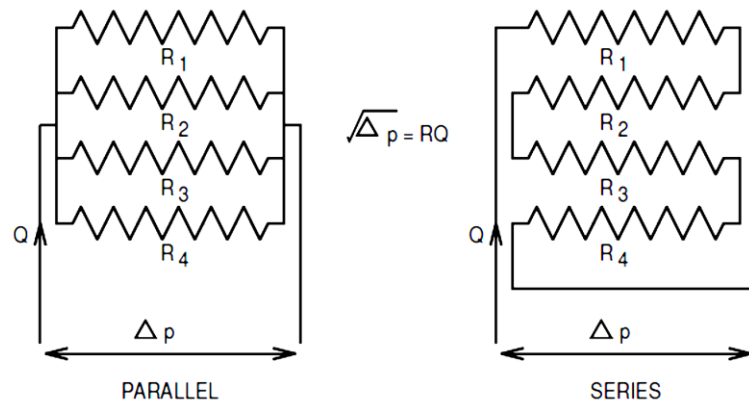


Figure 3.10 Hydraulic circuit non-linear analogy

[30] shows another analogy method between the electric circuit and hydraulic circuit by the equation  $\Delta P = RQ^2$ , which indicates the non-linear relation between the pressure drop and flow rate.

[31] discusses the linear relation between the pressure drop and flow rate which fulfils the equation  $\Delta P = RQ$ . The approximation is good if  $\frac{r}{L} \ll 1$  and  $\frac{r}{L} \ll 1/Re$ , where  $r$  is the radius of circular pipe,  $L$  is the length of the pipe,  $Re$  is the Reynolds number. For non-circular pipe,  $r$  is replaced by  $D_h/2$ , where  $D_h$  is the hydraulic diameter.

In this study, the radius of each parallel cooling channel is much smaller than the length of it, therefore the condition  $\frac{r}{L} \ll 1$  is fulfilled. On the other hand, the size limitation of the oil pump leads to relatively low coolant velocity, therefore relatively small Reynolds number and laminar flow, which means that the condition  $\frac{r}{L} \ll 1/Re$  is fulfilled. Hence, linear relation between the pressure drop and flow rate is applied in this study. Table 3.3 shows the analogy between hydraulic system and electric system.

Table 3.3 Analogy between hydraulic system and electric system

Type	Hydraulic	Electric
Quantity	Volume $V$	Charge $q$
Potential	Pressure $P$	Potential $\Phi$
Flux	Volumetric flow rate $Q$	Current $I$
Flux density	Velocity $v$	Current density $j$

The pressure losses  $\Delta P_f$  associated with a pipe of constant cross section, due to the wall friction along the fluid flowing direction is expressed by Equation 3.11 [8]

$$\Delta P_f = f \frac{L}{D_h} \frac{\rho \mathcal{V}_m^2}{2} = f \frac{L}{D_h} \frac{\rho Q^2}{2A^2} \quad 3.16$$

where dimensionless quantity  $f$  is the Darcy friction factor,  $\mathcal{V}_m$  is the mean velocity,  $L$  is the length of pipe,  $D_h$  is the hydraulic diameter,  $\rho$  is the density of coolant,  $A$  is the cross section area,  $Q$  is the flow rate.

For laminar flow, the Darcy friction factor  $f$  is a linear function of the Reynolds number and dependent on flow cross section geometry. There is another often used dimensionless friction factor which is the so called Fanning friction factor and it equals to  $f/4$ . The general expression of the Darcy friction factor for laminar flow is

$$f = \frac{k}{Re} = k \frac{\mu}{\rho \mathcal{V}_m D_h} \quad 3.17$$

where  $\mu$  is the dynamic viscosity, constant  $k$  differs with different shapes of pipe cross section. For turbulence flow,  $f$  is also dependent on the surface roughness of the pipe [32].

Combine Equation 3.16 and 3.17, friction pressure losses can be expressed as

$$\Delta P_f = k \frac{\mu}{\rho \mathcal{V}_m D_h} \frac{L}{D_h} \frac{\rho \mathcal{V}_m^2}{2} = \frac{k\mu L}{2D_h^2} \mathcal{V}_m \quad 3.18$$

Since  $Q = \mathcal{V}_m A$ , friction pressure losses for pipe with constant cross section is expressed as



$$\Delta P_f = \frac{k\mu}{2D_h^2} \frac{L}{A} Q \quad 3.19$$

Therefore, the corresponding hydraulic resistance is

$$R_f = \frac{k\mu}{2D_h^2} \frac{L}{A} \quad 3.20$$

According to Equation 3.20, the hydraulic resistance is proportional to the fluid dynamic viscosity, pipe length and inverse proportional to the cross section area and square of hydraulic diameter.

Equation 3.19 shows the friction pressure losses due to the frictions between the pipe wall and fluid. Except for the frictional losses, according to [32], the influence of internal contractions and expansions due to flow area changes, if present, is also lumped into the core friction loss term. Besides, the pressure changes due to the momentum rate change or the flow acceleration (or deceleration) effects because of the fluid heating (or cooling) should also be considered. Therefore, the total pressure drop for a straight pipe is expressed as Equation 3.16 [32, 33]

$$\Delta P = \frac{\rho \mathcal{V}_m^2}{2} * \underbrace{[1 - \sigma^2 + K_c]}_{\text{Entrance effect}} + \underbrace{+2\left(\frac{\rho_i}{\rho_o} - 1\right)}_{\text{Momentum effect}} + \underbrace{+f \frac{L}{D_h} \rho_i \left(\frac{1}{\rho}\right)_m}_{\text{Core friction}} + \underbrace{+(1 - \sigma^2 - K_e) \frac{\rho_i}{\rho_o}}_{\text{Exit effect}} \quad 3.21$$

where  $\mathcal{V}_m$  is the mean velocity,  $\rho$  is the average fluid density,  $\rho_i$  is the fluid inlet density,  $\rho_o$  is the fluid outlet density,  $\sigma$  is the ratio of the small area to the big area when the flow has sudden contraction or expansion,  $K_c$  is the contraction loss coefficient and  $K_e$  is the expansion loss coefficient.  $K_c$  and  $K_e$  is a function of contraction or expansion ratio  $\sigma$ , Reynolds number  $Re$ , and flow cross-section geometry.

As shown in Equation 3.21, the pressure drop caused by fluid flowing through a straight pipe with constant cross section area includes pressure losses caused by entrance effect, exit effect, friction and momentum effect. Among these effects, both pressure drops caused by entrance effect and

exit effect contain two contributions. One term introduced by  $1 - \sigma^2$  is the pressure drop due to the area change along, and the other term introduced by  $K_e$  or  $K_c$  is the pressure drop associated with the irreversible free expansion or contraction and the momentum rate changes following an abrupt cross section change. Besides, the momentum effect term reflects the pressure change caused by the change of fluid density.

In the cooling channel designs of this study, the outlet is not only contracted afterward expanded, but also bended. The bending of a pipe leads to the pressure losses because of the flow separation at the walls and a swirling secondary flow arising from the centripetal acceleration [34]. This results in a pressure gradient between the outer wall (maximum pressure) and the inner wall (minimum pressure) at a given cross section. The resulted secondary flow is shown at section AA in Figure 3.11 [32].

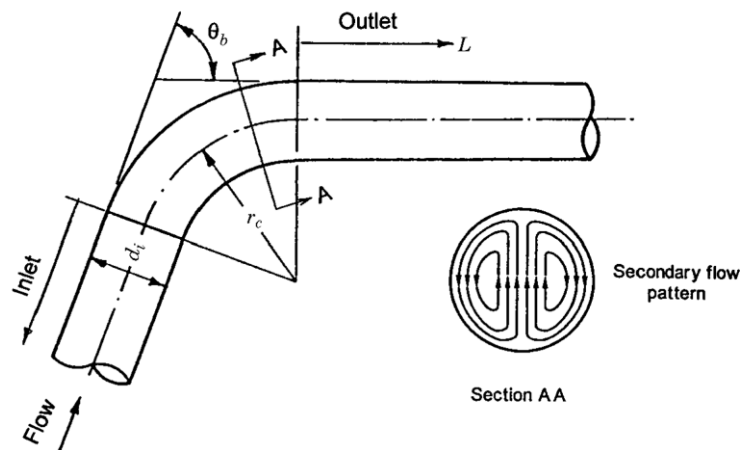


Figure 3.11 Circular-cross-section pipe bend with a secondary flow pattern [32]

Pressure drop associated with bending is expressed by

$$\Delta P_b = K_{b,t} \frac{\rho V_m^2}{2} \quad 3.22$$

where  $K_{b,t}$  is the total pressure drop coefficient due to the bend, which consists of two parts: (1) the pressure drop for the bend due to the curvature effect, the flow development effect in the outlet pipe, and the

surface roughness effect, and (2) the pressure drop associate with the outlet straight pipe of specified surface roughness. [32]

$$K_{b,t} = K_b + K_f = K_b + f \frac{L}{D_h} \quad 3.23$$

where  $K_b$  and  $K_f$  are pressure loss coefficients for these two contributions, separately.

As a conclusion for pressure drop calculation, besides the pressure losses due to the friction between fluid and walls, the pressure losses for a pipe should contain the pressure changes associated with [30, 32, 33, 34]

- Pipe entrance or exit
- Sudden expansion or contraction
- Bends, elbows, tees and other fittings
- Valves, open or partially closed
- Gradual expansions or contractions

### HEC implementation

Figure 3.12 shows the simplified cooling system applied in this study. Comparing to Figure 3.10, this equivalent cooling circuit combines both series and parallel configurations. Firstly, the nodes are chosen at the positions whose pressures are of interest. Thereafter, the hydraulic resistances are calculated between two closest nodes. As shown in Figure 3.12, the nodes are chosen at each paralleled cooling channels inlet and outlet since the pressure drop and flow rate at each paralleled cooling channel are of interest. Moreover, the resistances in red color ( $R_i$  and  $R_{i+1}$ ) and green color ( $R_o$  and  $R_{o+1}$ ) represent the hydraulic resistances of inlet inlet collector segments close to the inlet side and outlet collector segments close to the outlet side, separately. Besides, the resistances in blue color ( $R_c$ ) represent the hydraulic resistances of paralleled cooling channels.

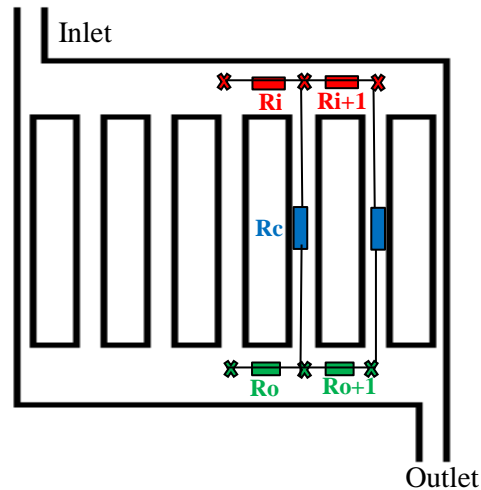


Figure 3.12 Simplified cooling system for electrical machines

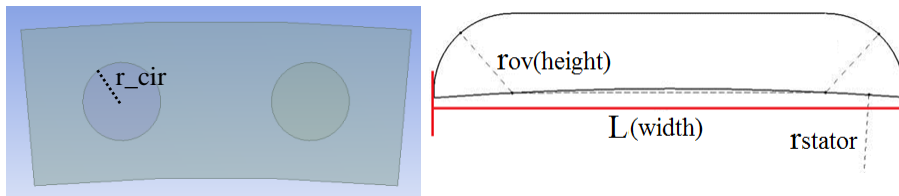
### 3.7 Specification of cooling channels for practical implementation

As shown in Figure 3.4, both electrical machines with direct cooling systems, independent of whether the direct cooling channels are made in the housing or made in the stator back, show better heat transfer performances than the machine with indirect cooling system. However, making cooling channels at the back of the stator means taking away some amounts of stator iron core, which may lead to more saturation of the machine and thus weaker performances than with the machine where the direct cooling channels are located in the housing. At the same time, the following study should be able to compare the differences between the direct and indirect cooling system, but electrical machines with different electro-magnetic behaviors will introduce another uncertain factor into the comparison which is not preferable. Thus making cooling grooves at the back of the stator is not regarded as an interesting alternative in the following study in this thesis. Therefore, one machine with the direct cooling channels made in the housing and one indirect cooling machine are selected for further manufacturing and investigation.

As shown in Figure 3.8 and Figure 3.9, the first proposed cooling channel design is to manufacture both indirect and direct cooling system with

paralleled oval ducts, since oval duct shows the best heat transfer coefficients and lowest temperature at the same machine operation point, i.e. the same applied current density, meanwhile with the same cost in term of space. However, due to the manufacturing limitations when indirect cooling channels are made in the housing, cutting the required oval shaped channels inside the housing is quite difficult. While drilling circular holes in housings is the most convenient way of making the paralleled indirect cooling channels. On the other hand, the paralleled direct cooling channels need to be maximally contacted with the stator laminations, hence making circular holes is not an option for direct cooling system. Additionally, taking away iron from the back of stator should be avoided as discussed before. In the end, cutting cooling channels in the housing with half oval cross section without changing the stator is chosen for direct cooling system, while drilling circular grooves in the housing is chosen for indirect cooling system.

In order to investigate the cooling performance differences just because of moving the cooling channels closer to the heat generation source, i.e. changing the heat dissipation paths, the total heat transfer coefficients should be identical between the two cooling systems. Therefore, the final design of the direct cooling system and indirect cooling system are chosen by insuring the total hydraulic parameters  $D_h$ , total areas and circumferences of the cross sections in the two cooling systems the same. This is done by scanning through and comparing the total areas and circumferences of circles which has diameter small than 5mm (decided by the thickness of the housing) and half oval which has height less 5mm and width less than 18.5mm (decided by the outer diameter of the stator). Ultimately, 36 half oval shaped directly cooling channels and 72 circular indirectly cooling channels are proposed with the following sizes:

(a) Indirect:  $r_{cir}=2\text{mm}$ (b) Direct:  $r_{ov}=2.65\text{mm}$ ,  $L = 11.05\text{mm}$ 

(c) Indirect cooling channel (80mm) with inlet and outlet collector

Figure 3.13 Final cooling ducts design for indirect (a), (c) and direct (b) cooling system, separately with total cross section area difference 0.3% and circumference difference 0.01%

Figure 3.13 (a) and (b) shows the final design of the cross section area for one indirect and one direct cooling channel, separately. Figure 3.14 (c) shows the channel design along the axial direction, which contains both the inlet and outlet collectors except for the 80mm paralleled cooling channel. Besides, the outlet is contracted to build up a high pressure drop, thereby forcing the coolant flow in each channel to be evenly distributed. Figure 3.14 shows the section pictures of the final designs of indirect cooling system and direct cooling systems with housing and stator iron, separately.

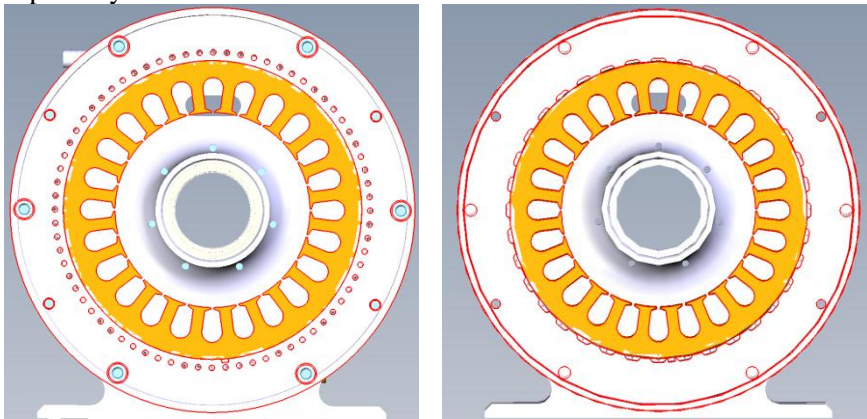
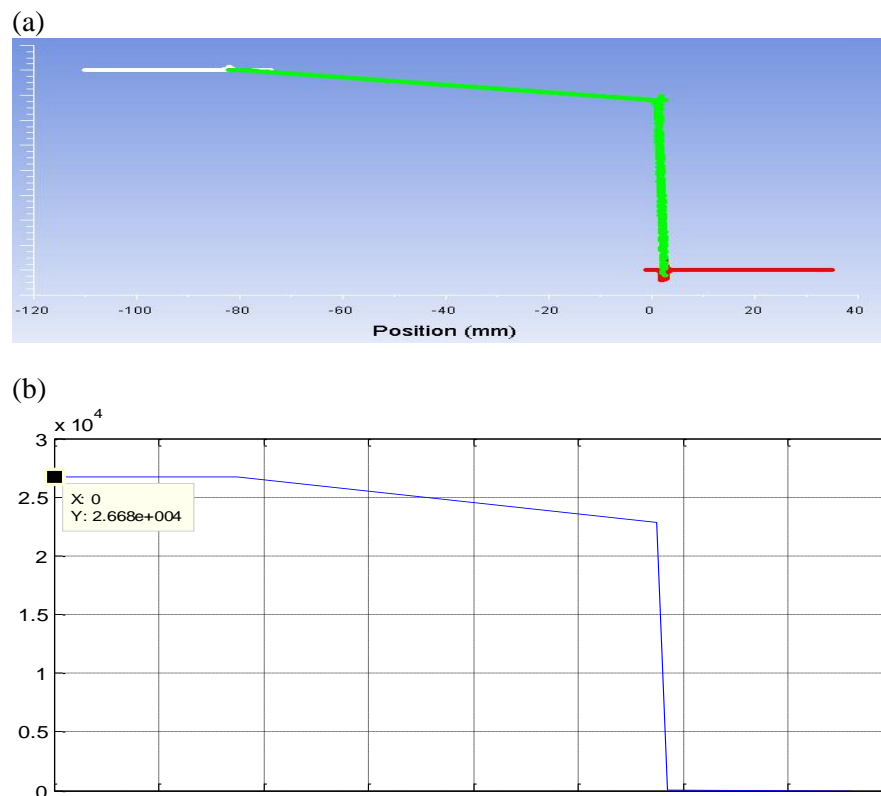


Figure 3.14 Final designs for indirect cooling system (left) and direct cooling system (right)

### 3.8 Flow network of selected cooling systems

As discussed in chapter 3.6, a Hydraulic Equivalent Circuit (HEC) is proposed to evaluate the flow network performances including flow rate distributions and pressure drop, i.e. the cost, of the whole cooling circuit. Besides, Figure 3.13 shows the HEC implementation method for the designed cooling circuit, which contains the hydraulic resistances for inlet collector, paralleled channel, outlet collector. The following Figure 3.15 shows the pressure drop along the fluid flow direction for one paralleled cooling channel including inlet and outlet collectors and with total flow rate 1.7L/min.



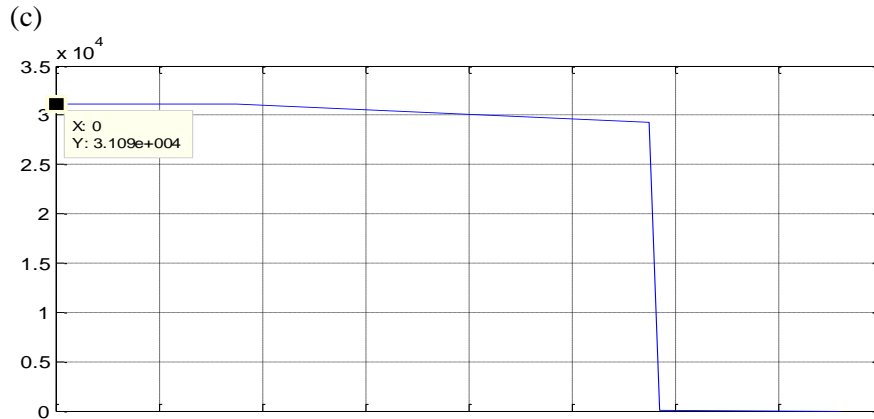


Figure 3.15 (a) CFD simulation result of pressure drop for indirect cooling channel (corresponding to Figure 3.14(c)); (b) Empirical calculation result of pressure drop for indirect cooling channel (corresponding to Figure 3.14(c)); (c) Empirical calculation result of pressure drop for direct cooling channel

Figure 3.15 (a) and (b) represents the pressure drop of indirect cooling channel obtained from CFD simulation and empirical calculation, separately. And Figure 3.15 (c) represents the pressure drop of direct cooling channel obtained from empirical calculation. As shown in Figure 3.15, the biggest percentage of the total pressure drop is caused by the small “bottleneck” at the outlet in both cooling systems. Besides, with total flow rate 1.7L/min at 22°C, the empirical calculations give 27 kPa and 31 kPa for one paralleled channel in indirect system and direct cooling system, separately. Comparing the pressure drops of a single channel in the two cooling systems, the direct cooling channel shows slightly higher pressure drop than the indirect cooling channel. That is mainly because that in the two cooling systems, the inlet and outlet ring shape collectors are designed with the same inner and outer radius, therefore moving the parallel cooling channels closer to the stator in the direct cooling system leads to prolonging of connectors between the paralleled channels and the ring shape collectors, which results in the higher pressure drop for a single channel in direct cooling system.

According to [18], the pumping power is calculated as below

$$W_{pump} = Q \cdot \Delta P \quad 3.24$$



where  $W_{pump}$  is the pumping power in Watt,  $Q$  is the flow rate in  $m^3/s$  and  $\Delta P$  is the pressure drop in Pa.

Table 3.4 shows the calculated hydraulic resistances for the selected cooling systems.

Table 3.4 Calculated Hydraulic Resistances

	Direct cooling channels		Indirect cooling channels	
<b>Inlet/outlet ring segment</b>	Hydraulic Resistance [kg/(s · m <sup>4</sup> )]	4.7e6	Hydraulic Resistance [kg/(s · m <sup>4</sup> )]	2.82e6
<b>Parallel channel</b>	Hydraulic Resistance [kg/(s · m <sup>4</sup> )]	3.94e10	Hydraulic Resistance [kg/(s · m <sup>4</sup> )]	6.78e10

Thereafter, the Hydraulic Equivalent Circuits for both cooling systems are built as shown in Figure 3.16 and 3.17.

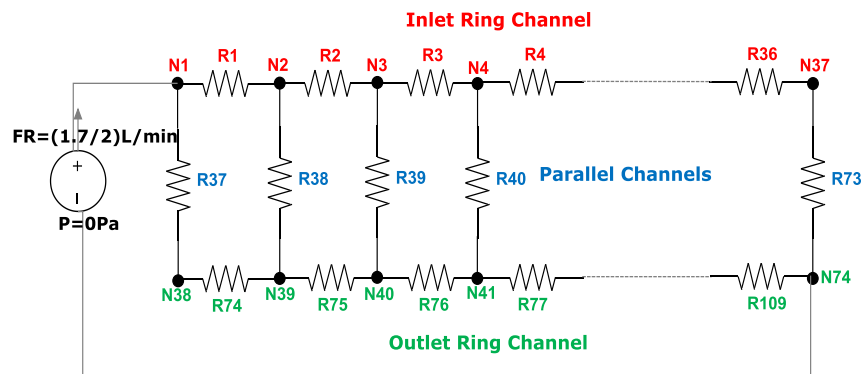


Figure 3.16 Hydraulic Equivalent Circuit for half of the indirect cooling system

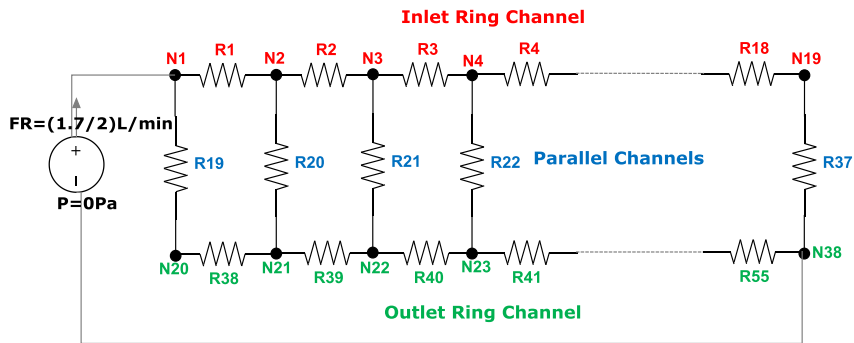


Figure 3.17 Hydraulic Equivalent Circuit for half of the direct cooling system

Similar to Figure 3.13, in both of Figure 3.16 and 3.17, the hydraulic resistances marked in red represents the resistances for inlet collector segments, the ones marked in blue represents the resistances for paralleled channels, and the ones marked in green represents the resistances for outlet collector segments. Besides,  $N_1$  to  $N_i$  represents the nodes at different positions.

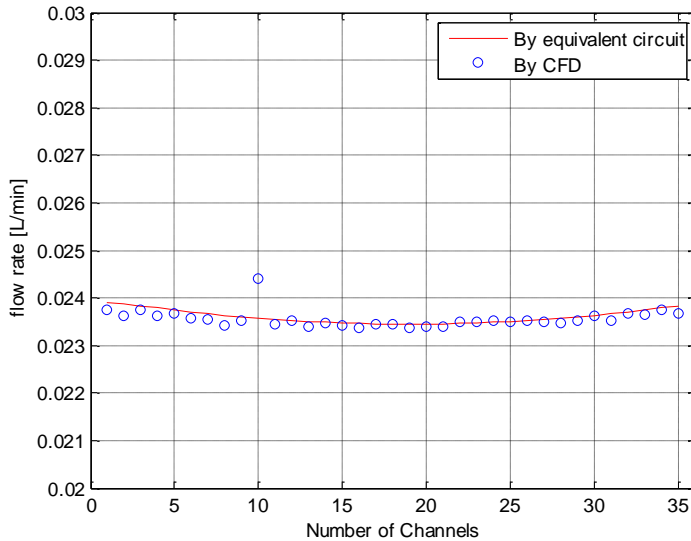


Figure 3.18 Flow distributions for indirect cooling system

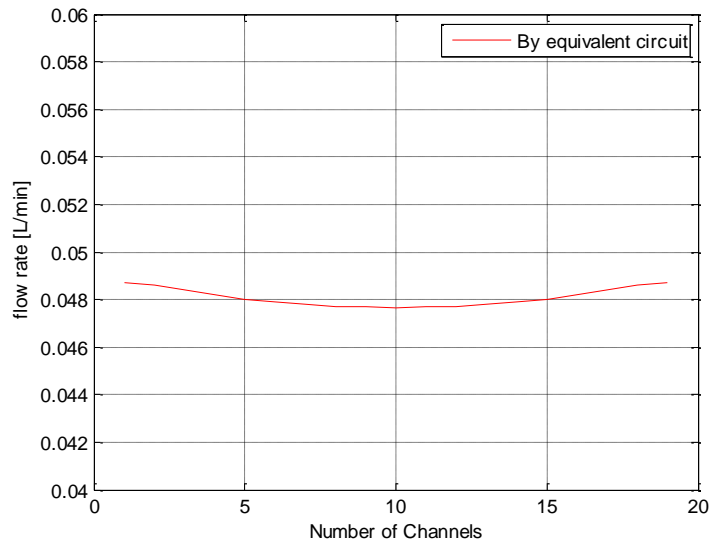


Figure 3.19 Flow distributions for direct cooling system

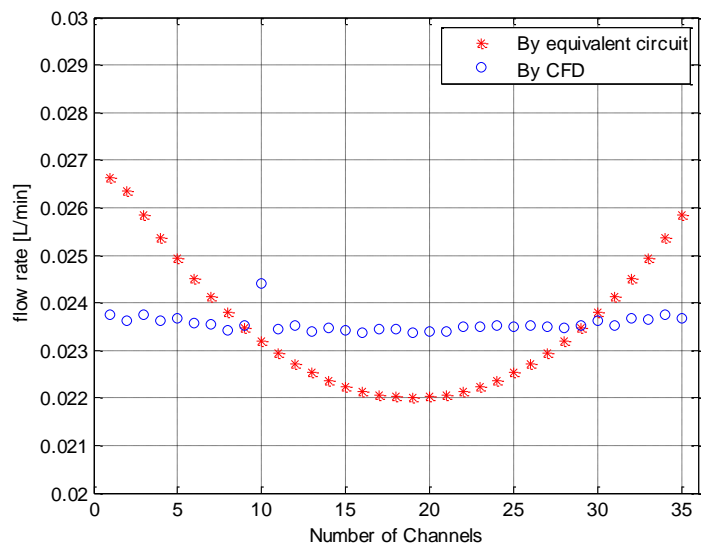


Figure 3.20 Flow distributions for indirect cooling system without contraction at outlet

Figures 3.18 and 3.19 show the flow rate distribution in each paralleled cooling channel for the designed indirect and direct cooling systems at total flow rate 1.7L/min. Pressure drop for direct cooling system is slightly higher with the same total flow rate because of the slightly longer design of the contracted outlet path. Figure 3.18 shows that the flow rate distributions calculated by CFD (blue circles) and hydraulic equivalent circuit (red line) show good agreement. Comparing Figure 3.18 to Figure 3.20, it shows that the coolant is distributed more evenly in each cooling duct due to the pressure drop built up by the contraction at outlet.

### 3.9 Summary

This chapter first presents the studied electrical machine and the coolant properties. Based on these known information, which is the size of the machine, the power losses to be dissipated and cooling medium properties, both indirect and direct cooling systems are studied based on different simulation tools which are CFD simulations and Hydraulic Equivalent Circuit (HEC) calculations.

CFD tools are used for two purposes. One purpose is to compare the heat transfer performances of direct and indirect cooling systems. Direct cooling system have cooling ducts made in stator or housing. Indirect cooling system includes thermal contact between the laminated stator core and the housing and cooling ducts inside the housing. This comparison shows that direct cooling system is better than the indirect cooling system, in term of interface temperature between the housing and the stator. Ultimately, the direct cooling system with ducts made in housing and indirect cooling system are chosen for further manufacturing and test. The alternative direct cooling system is not practically preceded as it needs more exhaustive redesign of electrical machine, since removing some amount of iron from the back of the stator has the possibility of influencing electromagnetic field distributions of the machine. At the same time, sensitivity studies of channel number and channel height and width are carried out. After all, 36 channels are proposed for both direct and indirect cooling system. For channels with a given cross section area, bigger in width and smaller in height channels show better heat transfer performances. The other purpose of CFD simulation is to characterize the cooling channels, therefore finding the most effective way of taking away heat within a limited space of an electrical machine. Channels with three different cross sections are studied and the oval duct is proposed to be the

---

best candidate for heat transfer with the same length and height, i.e. the same consumed space. After adjusting the proposed designs to the manufacturer's limitation, the final designs for both cooling systems are selected as shown in Figure 3.14. After selecting the cooling systems, HEC is used to evaluate the flow network performances including flow rate distributions and pressure drop, i.e. the cost, of the whole cooling circuit. The outcome of the cooling system performance, which is the ability to carry away the heat, is part of the complete heat transfer models (chapter 5) that are compared to the practical experiments (chapter 7). Heat production and heat sources are investigated in chapter 4.



## Chapter 4

# Heat Generations in Electrical Machines

This chapter discusses the power losses generated in different parts of an electrical machine. The calculated DC winding losses are implemented into 3D thermal FEA and lumped parameter models presented in chapter 5. In the end of this chapter, loss maps with various speed and torque combinations obtained by 2D electromagnetic FEA simulation are presented. These loss maps are used as inputs to the lumped parameter model in Simulink in order to predict the temperatures of electrical machines with driving cycles.

### 4.1 Interior Permanent Magnet Synchronous Machine (IPMSM)

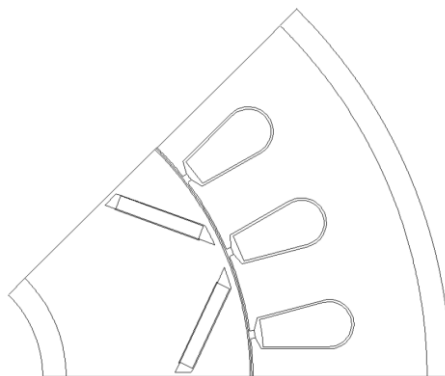


Figure 4.1 IPMSM with natural convection

### Modelling geometry and materials

As stated in 3.1, the studied electrical machine is designed in the Green Car project with nominal torque 30 Nm and the base speed 4550 rpm, which combined give a nominal power of 14.3 kW with natural convection. Figure 4.1 shows the machine design proposed in [22]. The material specifications are presented in table 5.2.

### Determination of rated operation point

A set of 2D finite element heat transfer analysis is taken in order to select the nominal current density for each of the simulated geometries at the predefined cooling conditions. However, the 3D nature of the heat transfer process in certain parts of the machine implies that there are thermal effects which are not accounted for in the 2D FE model [24]. Therefore, a more detailed thermal analysis is conducted by the lumped parameter model proposed in [35] to extend and contribute to 2D FEA.

## 4.2 Power losses in the windings

The power losses in windings are calculated by considering the temperature dependent resistances.

### DC losses

The current density in the cross section of a conductor is uniformly distributed if a DC current is running through. According to Ohm's law, the resistance of the conductor is the value of voltage over the conductor divided by the value of the current. This resistance is also called DC resistance. Copper loss due to flowing DC current varies with the load in proportion to the current squared and can be expressed as:

$$P_{DC} = R_{el}I^2 \quad 4.1$$

where  $P_{DC}$  is the stator winding losses in watt caused by DC current,  $R_{el}$  is the conductor resistance in ohm and  $I$  is the DC current in A.

According to the discussion in Chapter 2, the DC current losses can be expressed as

$$P_{DC} = J^2\rho_eV \quad 4.2$$

where  $\rho_e$  is the resistivity,  $L$ ,  $A$  and  $V$  are the length, cross section area and



volume of the pure conductor where the heat losses are generated, separately, and  $J$  is the current density in A/m<sup>2</sup>.

Nevertheless, resistances of winding are changed with the temperature changes. Therefore, the temperature coefficient should be considered if the temperature changes cannot be ignored

$$R_{el} = R_{el_r} [1 + \alpha_r (T - T_{ref})] \quad 4.3$$

where  $R_{el}$  is the conductor resistance at temperature  $T$ ,  $R_{el_r}$  is the conductor resistance at temperature  $T_{ref}$ ,  $\alpha_r$  is the temperature coefficient of resistance for the conductor material,  $T$  is the conductor temperature and  $T_{ref}$  is the reference temperature that  $\alpha_r$  is specified. Normally, for copper windings,  $\alpha_r$  is approximately 0.004 K<sup>-1</sup> according to [36].

### AC losses

According to reference [37], if a time-varying current is running in a conductor, the induced magnetic field is going to redistribute the current density due to the skin effect and the proximity effect.

The skin effect in a conduction material is evaluated by the skin depth  $\delta$ , which is defined by

$$\delta = \sqrt{\frac{1}{\pi f_r \sigma_e \mu_0 \mu_r}} \quad 4.4$$

where  $\sigma_e$  is the electrical conductivity,  $\mu_0$  is the magnetic permeability of free space,  $\mu_r$  is the relative permeability of conducting material. With increasing frequency, the skin depth  $\delta$  becomes thinner, which gives a higher current concentration around the periphery of the conductor. With the same total conductor current, the perceived resistance increases and thus the losses. For efficient use of a conductor, the conductor diameter should be less than two skin depths for the highest frequency of the current that the conductor is intended to carry.

The proximity effect of conductors means that when there is a bundle of conductors, the current density distribution is influenced by the conductors adjacent to it. It is the tendency for current to flow in loops or concentrated distributions due to the presence of magnetic fields generated by nearby

conductors. In transformers and inductors, proximity effect losses are generally more significant than skin effect losses. The AC losses are not accounted by the 2D FE electromagnetic simulations.

### 4.3 Power losses in the stator core

The core losses, also called the iron losses, ( $P_t$ ) of soft magnetic materials can be written as the sum of hysteresis loss ( $P_h$ ) and eddy current loss ( $P_e$ ) as shown below

$$P_t = P_h + P_e \quad 4.5$$

To account for a large discrepancy between the theoretical computed losses and the experimental measured ones, a third component is introduced, named abnormal or excess losses  $P_e$  [38]. Then the iron loss is the addition of hysteresis loss, eddy current loss and excess loss.

#### Hysteresis losses ( $P_h$ )

Magnetic materials have losses associated with the hysteresis of the  $B$ - $H$  loop, as shown in Figure 4.2 [39], where the x-axis is the magnetic field  $H$  and the y-axis is the flux density  $B$ . Hysteresis occurs due to friction associated with magnetic domain wall movement and magnetic domain rotation when an external magnetic field  $H$  is applied, causing the change in magnetic flux density to lag the change in the magnetic field. This lag is known as hysteresis. For an AC magnetic field, a loop is formed in the  $B$ - $H$  plane, forming the hysteresis curve. The area enclosed by such a loop corresponds to the hysteresis loss [40]. It also shows that the magnetized state of the material depends not only on the magnetizing force being currently applied, but also on the previous magnetic state [41].

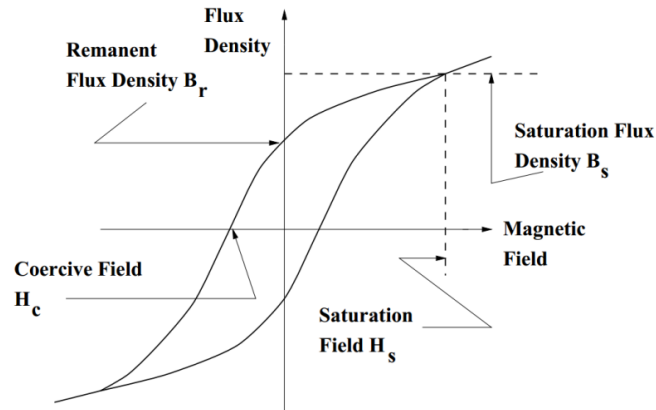


Figure 4.2 Hysteresis curve

Usually, the manufacturer specifies core losses curves as a function of the loss per volume or mass unit, depending on the flux density and the frequency. In some cases, empirically derived expressions are given instead of curves [40]. Steinmetz formula [41] shows the analytical equation of calculating the hysteresis losses

$$P_h = k_h \cdot f_r^{\partial 1} \cdot B_m^{\partial 2} \quad 4.6$$

where  $f_r$  is the frequency of flux reversal in Hz,  $k_h$  is the hysteresis coefficient,  $\partial 1$  and  $\partial 2$  are material dependent hysteresis loss constants and  $B_m$  is the AC peak flux density. According to [40], the hysteresis loop is travelled once each period, implying that  $\partial 1=1$ . Also, if the hysteresis loop is approximated as being rectangular,  $\partial 2=2$  can be assumed.

### Eddy current losses (Pe)

Eddy currents are the circulating currents resulting from changes of the magnetic fields in the core material. When any electrical conductor is placed within a magnetic field, a current perpendicular to the cross-section of the conductor is created and lead to the eddy current losses as shown in Figure 4.3. For this reason, steel lamination thickness is minimized to reduce the amount of eddy current flow. Moreover, the steel is alloyed with elements (often silicon) to further reduce eddy current losses [39].

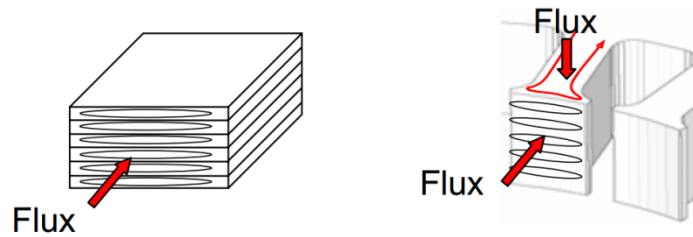


Figure 4.3 Eddy currents created in laminated steels with different magnetic fields [43]

Equation 4.7 [42] shows the analytical equation of calculating the eddy current loss of lamination steels

$$P_e = k_e \cdot f_r^2 \cdot B_m^2 \quad 4.7$$

where  $k_e$  is the eddy current losses coefficient.

### Excess loss

As discussed in [40], the excess loss results from the non-uniform distribution of the currents induced by the wall movement and the maximum intensity of these losses being obtained in the wall proximity. The analytical equation is expressed by [44]

$$P_{ex} = k_{xe} \cdot f_r^{1.5} \cdot B_m^{1.5} \quad 4.8$$

In the 2D FEA simulations, the stator losses are separated into the stator teeth losses and stator yoke losses based on the flux densities at these two parts.

## 4.4 Power losses in the rotor

The losses in the rotor are divided into electromagnetic losses in the rotor laminations and magnets, and mechanical friction losses. The electromagnetic losses are related to flux density and frequency. Mechanical friction losses are the losses caused by machine rotation. The calculation of power losses in the rotor is not the main concern of this work and therefore not treated here. Furthermore as the power losses are speed dependent the practical evaluation of cooling system and heat production is tested at low rotation speed.

### 4.5 Power loss map over various operation points

Usually the machine characteristics for vehicular application are shown as torque speed diagrams and efficiency map. Here the power loss maps of stator conductor and core losses are presented.

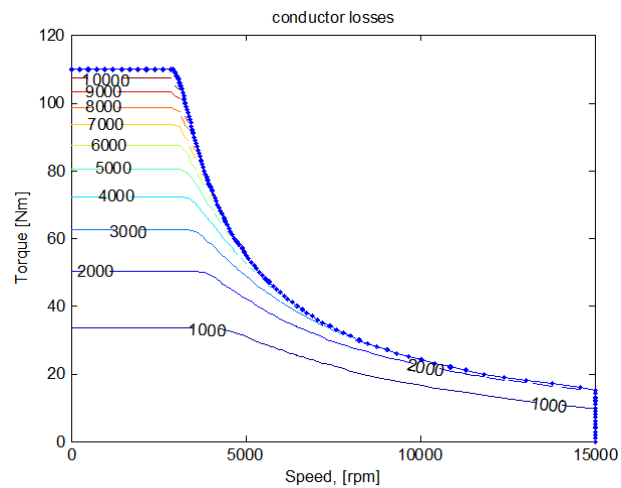


Figure 4.4 Winding loss map

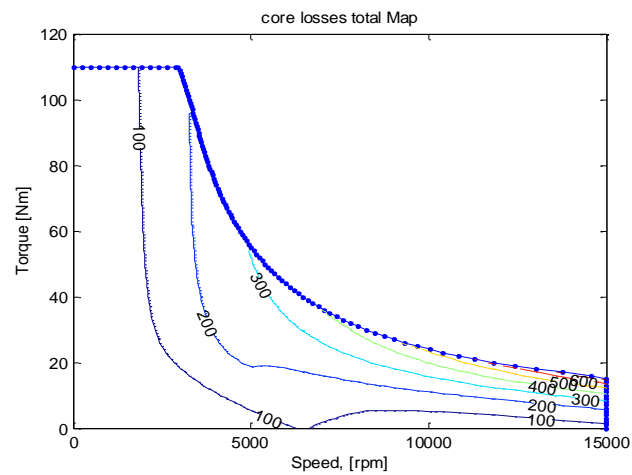


Figure 4.5 Stator core loss map

Figure 4.4 and Figure 4.5 show the winding losses and stator core losses contour maps of the designed machine, separately. The x-axis is the machine speed in rpm and y-axis shows the machine output torque in Nm. The losses are given in Watts. As shown in Figure 4.4, winding losses increase dramatically with increasing torque due to increased current loading, whereas, the stator core losses increase rapidly with increasing speed. The winding losses shown in Figure 4.4 are calculated based on the winding stator temperature at 150°C which need to be adjusted to the real temperature when it is used to evaluate the machine temperature with driving cycle.

#### **4.6 Summary**

This chapter discusses different electromagnetic power loss origins in permanent magnets synchronous machines, especially in the stator.

## Chapter 5

### Heat Transfer Analysis

Based on the previous cooling circuit design and power losses estimation (chapter 4), this chapter focuses on thermal circuits and heat transfer analysis. In general, electrical machine heat transfer theoretical analysis can be divided into two basic types: numerical methods and analytical lumped parameter method (LPM).

The main strength of numerical analysis is that any device geometry can be modelled with high accuracy. However, it is very demanding in terms of geometry set-up, mesh formation and computational time. There are two types of numerical analysis: computational fluid dynamics (CFD) and finite-element analysis (FEA).

As discussed in chapter 3, CFD has the advantage that it can include both fluid dynamic analysis and heat transfer calculation at the same time. For instance, it can be used to predict flow in various regions, such as natural convection around the electrical motor outer surfaces, forced convection inside cooling ducts and around the motor end windings, thereafter, to provide convection heat transfer coefficients for the interested regions. However, CFD approach requires relatively high mesh quality, therefore longer computing time than FEA approach.

FEA can only be used to model conduction heat transfer in solid components. For convection boundaries, the same numerical or analytical or empirical algorithms used in the lumped-circuit analysis must be adopted. The LPM approach has the advantage of being very fast to calculate; however, the developer of the network model must invest effort in defining a circuit that accurately models the main heat transfer paths.[24]

Considering the pros and cons for both numerical and analytical heat transfer approaches, this chapter presents heat transfer analysis on both direct cooled and indirect cooled motors by FEA and LPM approaches separately, with convection coefficients for forced cooling channels adopted from CFD.

Thereafter, the verified LPM is implemented in MATLAB Simulink in coordination with a parallel hybrid vehicle model and control algorithm with pre-defined driving cycles as a reference input. It brings an opportunity of monitoring the temperatures of an electrical machine for vehicular application in driving conditions at any instantaneous time while following the loss maps presented in chapter 4.

## **5.1 Model definition**

### **FEA thermal analysis**

Numerical thermal analysis including FEA thermal analysis and CFD thermal analysis has the strength of modelling and visualizing any device geometry exactly. To obtain any result from numerical analysis, one has to follow the steps, which are geometry building, creating mesh, assigning materials, boundary conditions set-up, equation solving and results postprocessing.

Compared to CFD thermal analysis, FEA is normally chosen and used to model heat conduction in solid components. As mentioned before, for convection boundaries, the same numerical or analytical or empirical algorithms used in the lumped-circuit analysis must be adopted [24]. In this study, the convection boundaries in the forced oil cool regions are obtained from CFD calculation. Besides, the convection boundaries in the natural convection regions are obtained by analytical and empirical approaches.

The thermal FEA studies for electrical motor are carried out by the state of the art software ANSYS.

### **LPM thermal analysis**

LPM solves the heat transfer problems by applying thermal circuits in analogy to electrical circuits. In this part, the electrical description of thermal systems, node presentation approach and thermal resistances and



capacitances calculation method are discussed.

- **Description of thermal systems analogous to the electric circuits**

The one dimensional heat conduction in the electric/electronic components is described in a homogeneous isotropic material Equation 5.1[6]

$$\frac{\partial^2 T}{\partial x^2} = \frac{c \cdot \rho}{\lambda_{th}} \cdot \frac{\partial T}{\partial t} \quad 5.1$$

where  $\lambda_{th}$  stands for the specific heat conductance,  $c$  for the specific thermal capacitance,  $\rho$  for the density of the material,  $T$  for the temperature and  $x$  for the coordinates in the direction of the heat propagation.

In the search for an electrical analog model for heat conduction, the comparison with a transmission line comes closest. After simplification, the transmission line can be changed into [45]

$$\frac{\partial^2 U}{\partial x^2} = C' \cdot R' \cdot \frac{\partial U}{\partial t} \quad 5.2$$

where  $C'$  is the capacitance per unit length,  $R'$  is the resistance per unit length.

Table 5.1 shows the analogous parameters applied in thermal circuit and electric circuit, separately.

Table 5.1 Analogous parameters

Thermal		Electrical	
Temperature	T in K	Voltage	U in V
Heat flow	P in W	Current	I in A
Thermal resistance	$R_{th}$ in K/W	Resistance	R in V/A
Thermal capacitance	$C_{th}$ in Ws/K	Capacitance	C in As/V

- **Node representation**

The thermal lumped parameter model is based on limited number of nodes representing different parts of an electrical machine. These nodes are chosen because of the interested temperatures at these parts of the machine. In general, the geometrical complexity of an electrical machine requires a large thermal network if a

solution with a high resolution of the temperature distribution is required [46]. However, the lumped-parameter thermal models provide an appealing means of estimating the key temperatures inside an electrical machine much more rapidly than with FEA, albeit with some loss in estimation accuracy [47].

- **Equivalent thermal resistances and capacitances**

After determining the nodes of which the temperatures are interested to investigate, it is important to obtain the accurate equivalent thermal resistance between every two nodes and thermal capacitance between each node and ambient. Thermal resistance defines the heat conduction capability, which is determined by the geometry and thermal conductivity of the studied object. Thermal capacitance reflects the dynamics of the temperature evolution, which is determined by the geometry and heat capacity of the studied object. The calculation methods for different equivalent thermal resistances are presented in [35].

## 5.2 Material properties

Table 5.2 shows the thermal conductivities and thermal capacitances of different parts of the electrical machines. These properties are applied in both FEA and LPM calculations.

Table 5.2 Thermal conductivities and specific heat capacity for different parts of electrical machine

Machine part	Thermal conductivity [W/(m·K)]	Specific heat capacity [J/kg/K]
Housing	237	897
Stator lamination (axial direction)	0.37	450
Stator lamination (radial direction)	31	450
Winding copper	400	385
Winding impregnation	0.18	247
Winding linear	0.2	247
Slot wedge	0.2	247
Rotor lamination (axial direction)	0.37	450

Rotor lamination (radial direction)	31	450
Magnets	8	425
Shaft	237	897
Air	0.03	1012

The fill factor for the winding active part is 0.36, for the end winding part is approximately 0.25 according to the manufacturer. The stacking factor of the stator and rotor laminations is 0.97.

### 5.3 Losses

As shown in chapter 4, obtaining accurate losses of a motor under different operation points is important. When the motor is running at a high speed and low load, iron losses rather than copper losses dominate the total generated losses. Furthermore, iron losses are affected not only by the rotor rotation speed but also the lamination steel properties. However, according to [48], different manufacturing processes, which are related to high temperature or mechanical stresses, can lead to the actual properties of the lamination stack differ significantly from the properties in the data sheet, which is normally tested under a specific pressure, humidity, temperature and etc.

In order to verify the thermal models and the designed cooling circuits, the complex power losses estimation in iron core is avoided on purpose. The validation of the thermal model is carried out with rather low rotor rotation speed. Under this circumstance, copper losses are dominated but the iron losses can be ignored.

However, based on the verified thermal model, if temperatures of electrical machines at various operation points are interested, loss maps at different motor components such as windings, stator yoke and stator teeth must be applied. The loss maps are obtained from core loss maps of laminated materials at different frequencies and magnetic flux density, which is calculated by software FEMM with FEA approach as presented in chapter 4.

### 5.4 3D Finite Element Thermal Analysis

In order to compare the cooling performances between the two electrical machines with cooling channels made at two different ways in the

housing, the steady state analysis by 3D FEA is carried out first. The 3D FEA thermal steady state analysis is made by Ansys Steady State Thermal package, in which the implemented heat transfer coefficients of internal forced cooling channels are obtained from CFD simulations (chapter 3). Comparing to transient FEA heat transfer analysis, the steady state calculation takes much less time. However, it is still able to calculate the temperatures at different parts of the electrical machines when thermal equilibrium is reached. By comparing the steady state temperatures, one can easily compare the two different cooling approaches. Next, the 3D FEA model setup for electric machine is discussed.

### Equivalent winding

The modelling of stator winding needs to have special concern due to complex 3D geometry of various materials that introduce highly anisotropic properties for the winding volume. Therefore this section describes how the windings are modelled.

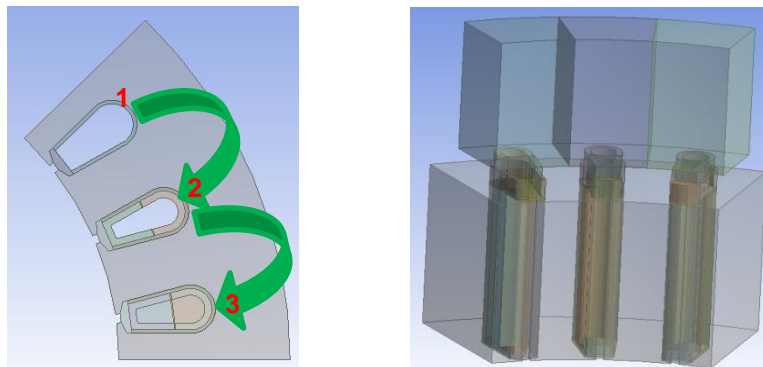


Figure 5.1 3D FEA equivalent winding active part (left); and equivalent windings of both active and end parts (right)

Table 5.3 Winding data

<b>Number of strands per turn</b>	8	<b>Number of turns per coil</b>	8
<b>number of coils per slot</b>	2	<b>active winding fill factor</b>	0.36
<b>end winding fill factor</b>	0.25	<b>active length of the winding</b>	80 mm
<b>end winding axial length 1</b>	45 mm	<b>end winding axial length 2</b>	35 mm
<b>conductor diameter</b>	0.8 mm	<b>wire diameter</b>	0.88 mm

<b>liner thickness</b>	0.48 mm	<b>wedge thickness</b>	3mm
<b>slot insulation thickness</b>	0.31 mm	<b>slot divider thickness</b>	0.24 mm

The simulation simplifies the winding active and end parts. For winding active part, all the copper conductors are lumped together as one block in the middle of a slot as shown in Figure 5.1. Besides, the winding impregnations and insulations are lumped as one layer of equivalent winding insulation around the equivalent copper block. This corresponds to a worse thermal situation than the real winding since most of the conductors of the real winding does not have all winding and slot insulation on their “outside”.

Figure 5.1 (left) shows the three steps of parameterizing the equivalent winding active part, which contain (1) draw the slot wedge and lumped the slot linear; (2) draw the equivalent winding insulation layer; (3) draw the double layers copper blocks with slot divider. The equivalent parameters are calculated from the physical sizes of the real windings which are presented in table 5.3. The winding fill factor is defined as the ratio of the total cross section area of pure copper to the total slot area. The end winding axial length 1 and end winding axial length 2 show the end winding length in non-drive end and drive end, separately.

The end windings are simplified as a solid body representing the mixture of pure conductor, air, impregnations and insulations. The reason of simplifying the end winding in such a manner is because that the end winding wires are not only winded in the axial direction as active windings, but also bended along other directions, which results in that the heat transfer path in the end windings is not mainly in the axial direction but follows the bending path of the pure conductors. Besides, sometimes the real end windings normally pressed or punched into such a block in order to save space. According to [49], the equivalent thermal conductivity of the end winding  $\lambda_{ew}$  can be calculated as

$$\lambda_{ew} = \lambda_{cond}F_{ew} + \lambda_{ins}(1 - F_{ew}) \quad 5.3$$

where  $\lambda_{cond}$  and  $\lambda_{ins}$  are the thermal conductivities of pure conductor and the impregnation material, respectively, and  $F_{ew}$  is the average fill factor of the end winding.

The equivalent thermal resistance (inverse of thermal conductance) in Equation 5.3 is obtained by considering the pure conductor and insulation are connected in parallel as shown in Figure 5.2 (left), where the blue region represents the insulation layer and the orange region represents the conductor layer. Equation 5.3 is sufficient if the heat produced by the end windings is mainly conducted through the pure conductor to the active winding, and then to the stator, housing and finally to the ambient. However, it underestimates the thermal resistances between middle of the end winding and the surrounding air which is enclosed in the housing. In this scenario, the heat produced by the end winding has to pass layers of insulation and conductor, which are connected in series as shown by Figure 5.2 (right) [56], and the corresponding equivalent thermal conductance is expressed as

$$\lambda_{ew} = \frac{\lambda_{cond}\lambda_{ins}}{\lambda_{cond}F_{ew} + \lambda_{ins}(1 - F_{ew})} \quad 5.4[56]$$

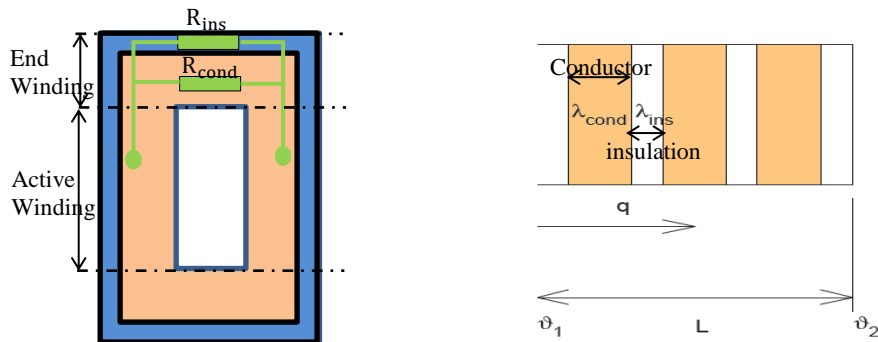


Figure 5.2 Equivalent thermal resistance or conductance of a winding- conductor and insulations in parallel connection (left); conductor and insulations in series connection (right) [56];

### Results from 3D FEA

Figure 5.3 and 5.4 show the temperature distributions of electric machines with direct and indirect cooling systems, separately. The applied RMS current is 31.15A and the total flow rate is 1.7L/min for the both machines. The figures clearly show that maximum temperature of the machine is decreased from 89.1 to 85.6°C by moving the cooling channels closer to the stator.

Figure 5.5 shows that (1) the temperatures in the middle of the end windings are the highest, i.e. the hottest spots in windings; (2) the highest temperature of the winding active part is located in the middle of the active winding; (3) along the radial direction there are great temperature gradients from winding center to winding outer surface. The big temperature gradients in the equivalent winding insulation layer are outcome of the low thermal conductivity.

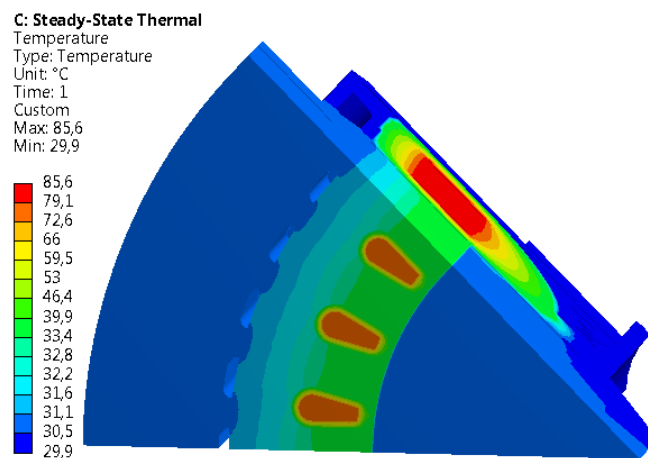


Figure 5.3 3D FEA temperature prediction for machine with direct cooling system, applied current 31.15A and current density  $6.7 \text{ A/mm}^2$

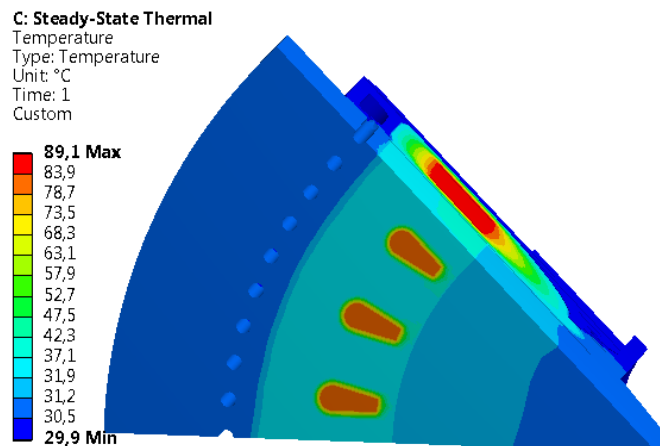


Figure 5.4 3D FEA temperature prediction for machine with indirect cooling system, applied current 31.15A and current density  $6.7 \text{ A/mm}^2$

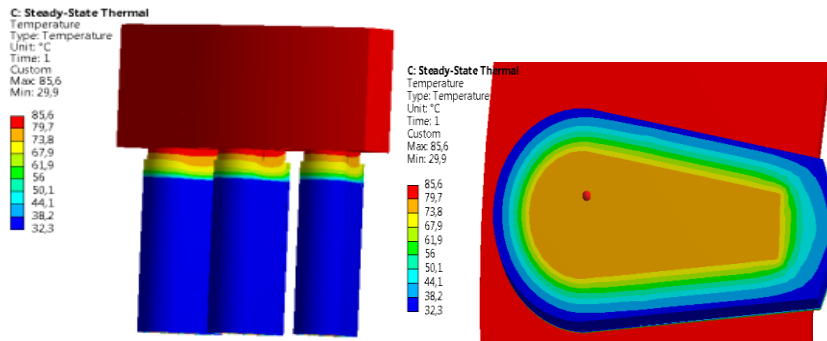


Figure 5.5 3D FEA winding temperatures (left) and cross section view of active winding temperatures (right) for machine with direct cooling system, applied current 31.15A and current density 6.7 A/mm<sup>2</sup>

## 5.5 Lumped Parameter Model (LPM)

Chapter 5.1 explains the basic knowledge about the LPM including analogousness between thermal and electrical circuit, node representation and equivalent thermal resistances and capacitances. As discussed in [47], the lumped-parameter thermal models provide an appealing means of estimating the key temperatures inside an electrical machine much more rapidly than with FEA, albeit with some loss in estimation. For instance, if monitoring the temperature of an electrical motor at any instantaneous time while driving is interested, a fast transient heat transfer calculation approach such as LPM is required.

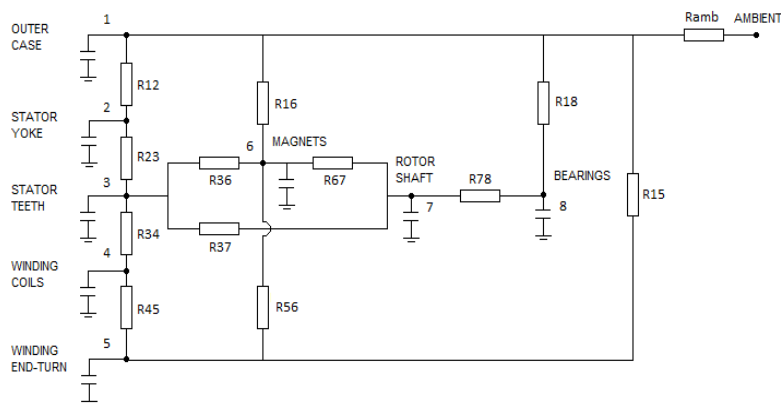


Figure 5.6 Lumped parameter model for an electrical machine [35]



Figure 5.6 shows the schematic drawing of the lumped parameter model used in this study. It is inherited from the Green Car Project and it is presented and verified in [35]. This lumped parameter model has 8 nodes whose temperatures are interested to be investigated. The chosen nodes are the winding active part, the winding end part, the stator yoke, the stator teeth, the rotor magnets, the rotor core, the rotor shaft and the bearings as shown in table 5.4.

Table 5.4 Specified nodes in lumped parameter model

1	Housing	5	Winding end turn
2	Stator yoke	6	Magnets
3	Stator teeth	7	Rotor shaft
4	Winding coil	8	Bearing

## 5.6 LPM with driving cycles

Based on the verified lumped parameter model, a new application is presented in the following discussions. This application aims to obtain temperature distributions over different driving cycles of a designed electrical machine which is implemented in a hybrid vehicle without plug in possibility. By analysing the temperature evolution under driving cycles, on one hand, it offers the possibilities of choosing the suitable materials which can endure the worst thermal stress, at the same time, is not over estimated, i.e. too costly. On the other hand, if the applied materials properties are known, life time and aging speed can be evaluated based on these results.

### Studied vehicle

A car with weight 1600 kg, wheel radius 0.3 meter and maximum required traction power 100 kW is studied. Internal combustion engine (ICE) has maximum power 75 kW and maximum speed 6000 rpm. The electric traction motor is used as a hybrid support machine on the rear axis, which has one-gear transmission and reaches maximum speed 15000 rpm at a vehicle speed of 172 km/h.

### Driving cycle

The New European Driving Cycle (NEDC) and the high speed (US06) driving cycle are studied. It contains the total driving time, speed, acceleration of the car and slope of the road. Figure 5.7 and 5.8 show the

studied NEDC driving cycle and US06 driving cycle, separately. The x-axis shows the time in second and y-axis shows vehicle speed in km/hour.

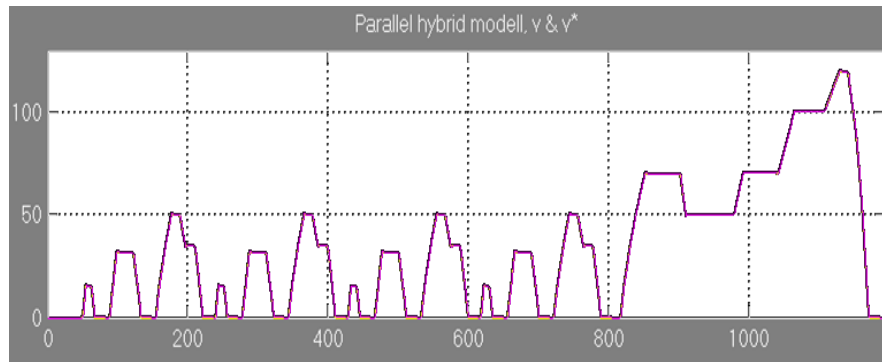


Figure 5.7 NEDC driving cycle

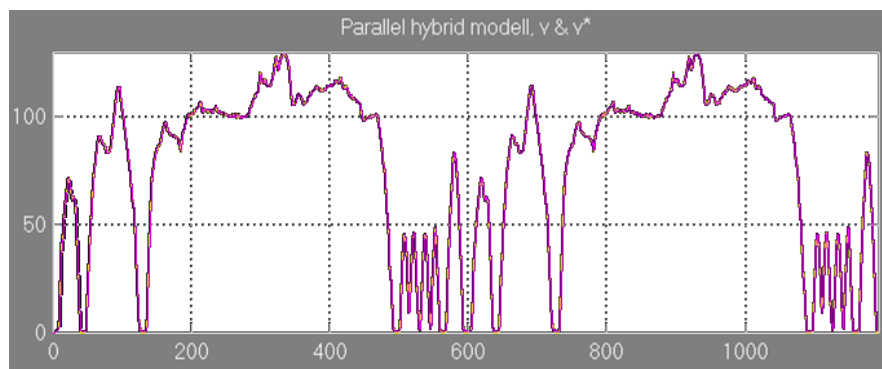


Figure 5.8 US06 driving cycle

### Loss map

The loss maps are formed by calculating the loss in a certain part of an electrical machine at any operation condition, i.e. any speed and torque combination. Three loss maps are applied into this calculation, which are loss map for windings, stator yoke and stator teeth. These loss maps are obtained by postprocessing the electro-magnetic FEMM calculations for the designed motors. Furthermore, the loss map for the windings is divided into loss maps for winding active part and the one for winding end part, separately. As discussed in chapter 4, the losses for the rotor and magnets are neglected. Figure 4.4 and 4.5 show the loss maps for the windings and the stator core, separately.

These loss maps of the end winding, the active winding, the stator teeth and the stator yoke are imported into two dimensional look-up tables in Simulink, as shown in Figure 5.9. At any instantaneous time, with any input of the required torque and speed of the electrical machine, the look-up table outputs the corresponding loss values and then it is used as the inputs to the thermal LPM to solve the temperature partial differential equations.

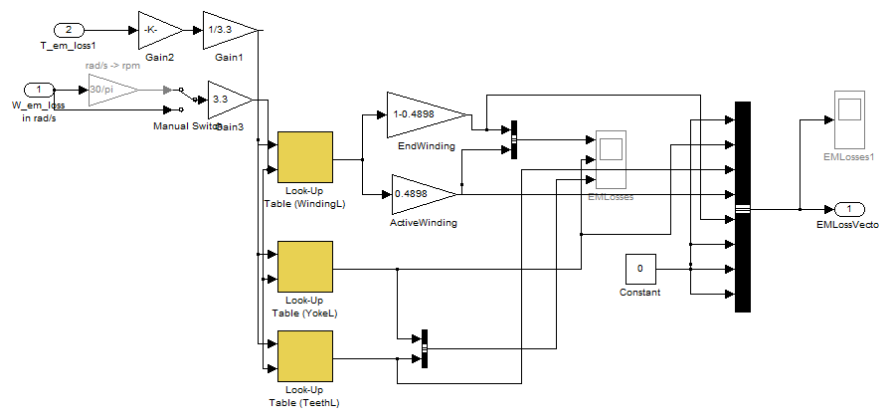


Figure 5.9 Simulink model of imported loss maps

### LPM implementation in Simulink

Comparing to the LPM implementation in Matlab, LPM implementation in Simulink has its advantages in terms of graphical interface, ease of solving differential equations and so on. Besides, in order to combine with the whole traction system which is built by Simulink, the LPM must be ‘translated’ to Simulink ‘language’. Figure 5.10 shows the Simulink model of solving temperature differential equations by having vectors of thermal conductances, thermal capacitances and power losses as inputs, and temperatures and temperature derivatives at the interested nodes as outputs as shown in table 5.4.

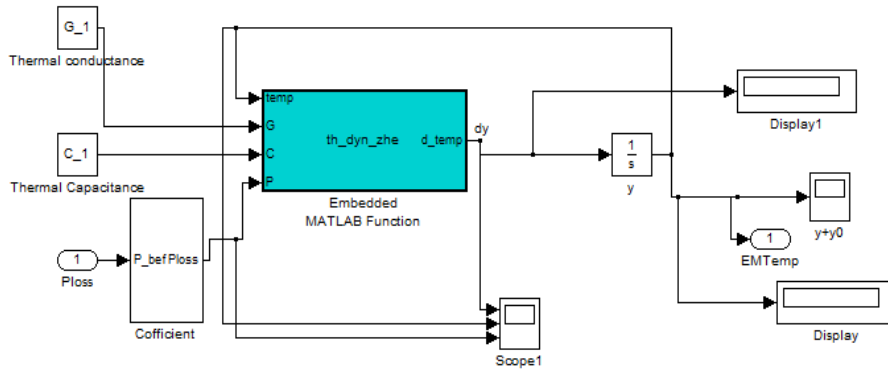


Figure 5.10 Simulink model of solving temperature differential equation based on imported thermal conductance and capacitance matrixes

## Results

Figures 5.11 and 5.12 show the temperature evolutions after driving with NEDC driving cycle and US06 driving cycle, respectively. The x-axis represents the driving time in second and the y-axis represents the temperatures in °C. There are 8 curves in the plots which represent the temperatures at the 8 different nodes as presented in table 5.4.

The two plots clearly show that the two hottest spots in the machine are presented by the green and red curves which are the node temperatures of the winding end part and the winding active part, separately. The machine shows quite low temperatures while driving in the city traffic until the last several minutes. Comparing to the NEDC driving cycle, during the last few minutes, the car is decelerated therefore the electrical machine is working as generator to charge the battery. Though battery charging while decelerating helps the energy saving, the designer should keep in mind that it also results in thermal stress to the electrical machine, as shown by Figure 5.11. Figure 5.12 shows that while the vehicle is driving on the high way, insulation class F which can endure maximum 155°C is good enough at most of the time. However, there are two peaks during the whole driving cycle of which the temperatures are over 155°C, but it will definitely work with insulation grade H (maximum allowed hot spot temperature 180 °C).

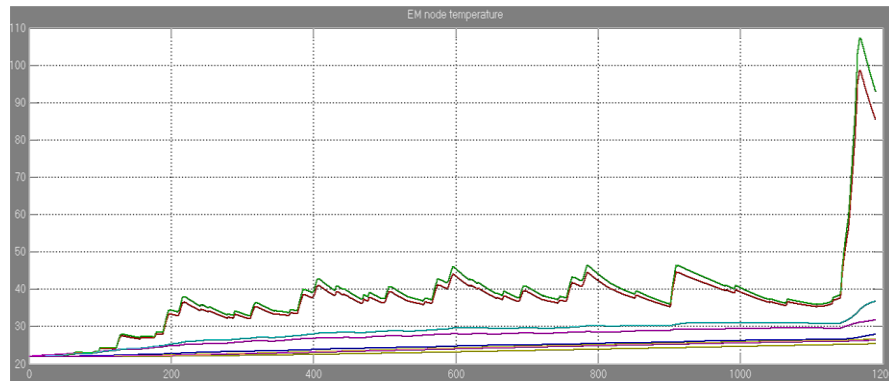


Figure 5.11 Temperature evolution while driving with NEDC driving cycle

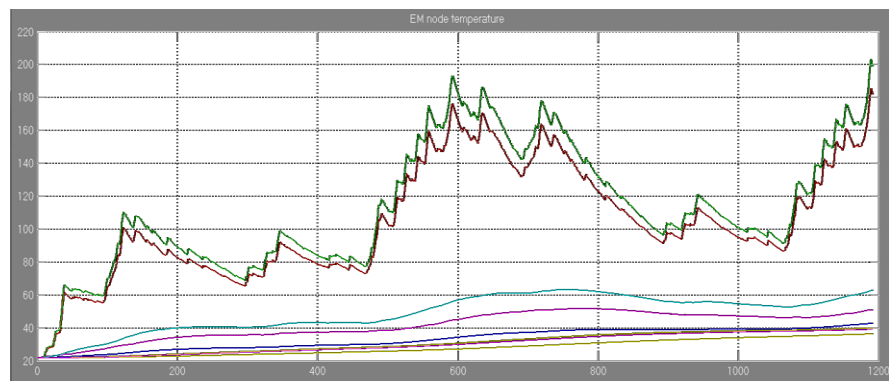


Figure 5.12 Temperature evolution while driving with US06 driving cycle

## 5.7 Summary

This chapter presents two different thermal models, which are 3D Finite Element Analysis (FEA) and Lumped Parameter model (LPM), separately. The simulations clearly show that the machine with direct cooling system has lower temperatures than the one with indirect cooling system at the same operating conditions. Besides, this chapter also presents the method of predicting electrical machine temperatures while driving with different driving cycles and hybrid vehicle drivetrain.



# Chapter 6

## Experimental Setup

This chapter discusses the experimental setups in terms of testing system and components.

### 6.1 The thermal test method

#### Goals

There are two goals of the thermal test: (1) compare the heat transfer performances between electrical machines with direct cooling system and indirect cooling system; (2) study the test results then evaluate the simulation or theoretical calculation methods. At the same time, gaining the experiences on thermal test is also very important.

#### Practical realization

A machine test normally includes measurement of torque-flux maps, torque-speed diagrams, efficiencies maps. Making such measurements usually require a test bench including torque sensors, a power analyzer and accurate adjustment of the test machine, torque sensor and load machine line up. The test system is expensive and time consuming to arrange and also to use since a sequence of stationary measurements are made [50].

However, the machine tests in this study get rid of the expensive and time consuming test bench based on the dynamic test approach developed by Yury Loayza Vargas in IEA department, Lund University. [50] presents the theory and evaluation of the dynamic test with the ambition of measuring the machine rotor position, stator current and inverter voltage, and estimating machine torque, speed, flux and efficiency. Based on the developed test methods, the tests in this study also extent the function ranges of dynamic test approach to include the thermal measurements.

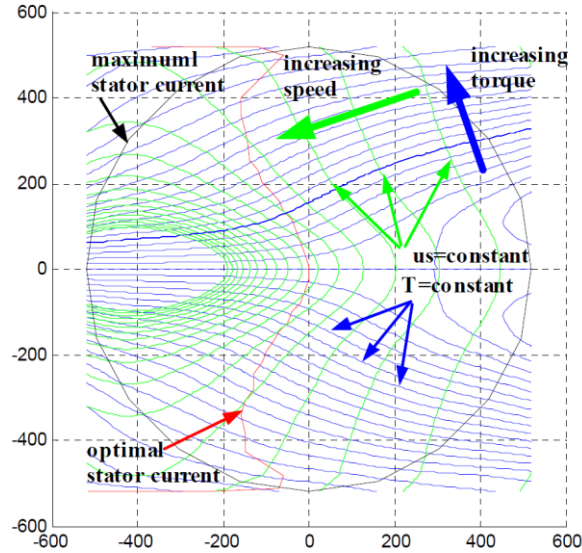


Figure 6.1 Current (black), torque (blue) and voltage (green) contour lines and optimal stator current (red) in  $x/y$  current frame

Figure 6.1 [51] shows the machine current, torque and voltage contour lines in the rotor reference frame ( $x, y$ ) with  $x$  aligned with the permanent magnets main direction of magnetization. The horizontal axis show the  $i_x$  current and the perpendicular axis show  $i_y$  current. The iso stator voltage (or torque) curves describe where the stator current must be for constant voltage (or torque). Besides, the  $i_{s0}$  stator voltage lines are parts of ellipses with a radius that shrinks as the speed increases. Moreover, this figure shows that a certain torque can be achieved by the use of an infinite number of combinations of the stator current components in the  $x/y$ -reference frame. However, it is possible to find current vectors crossing the torque contour lines, at the same time, the end points of the current vectors are closest to origin of  $i_x/i_y$  coordinate, i.e. smallest magnitudes of applied current. The optimal stator current curve in red shows the shortest applied current vectors at all torque levels, i.e. the biggest torque/current ratio.

However, since one of the aims of the electrical machine thermal tests is to compare the heat transfer performances of the two different cooling systems, the steady state temperatures at different current levels need to be



studied. Then it requires (1) the machine controller should be able to keep running the machine at a certain speed for enough long time until the measured temperatures reaching steady state; (2) at the same time, the machine controller should be able to run the machine with different current levels. Therefore, for the machine thermal tests, the optimal stator currents are not chosen, instead, different level of  $i_{sx}$  currents with  $i_{sy} \approx 0$  are applied, in order to keep the acceleration or deceleration torque to zero, i.e. constant speed.

On the other hand, the other aim of the thermal tests is to evaluate the thermal models, hence keeping relatively simple of the loss model will make the comparisons of the thermal models relatively simple and easy. Therefore, the machine tests are carried out at the lowest possible speed with electrical frequency 2.5Hz, and as discussed in 6.2, the friction losses and iron losses are negligible at such a low frequency. PI speed controller is also implemented to make precise control on speed.

According to [50], the motor control algorithm is created in LabView (from National Instruments) and applied to a real time controller cRio NI-9022 which is composed of a real time unit and a FPGA. FPGA is used for the rotor position/speed and motor input voltage/power estimation, measurement noise filtration, coordinate transformation, etc. A 4-channel simultaneous analogue input module (NI-9215) is used for measurements of the phase currents and the rotor position. A sequential analogue input module (NI-9205) with 32 channels is used for the dc link voltage, dc link current, temperature, etc measurements. A high-speed digital I/O module (NI-9402) is used for tracking the state of the PWM voltages applied to each phase. [50] also shows that the nominal dc-link voltage of 300V the measurement accuracy is  $\pm 0.18V$ .

## 6.2 Experimental setup

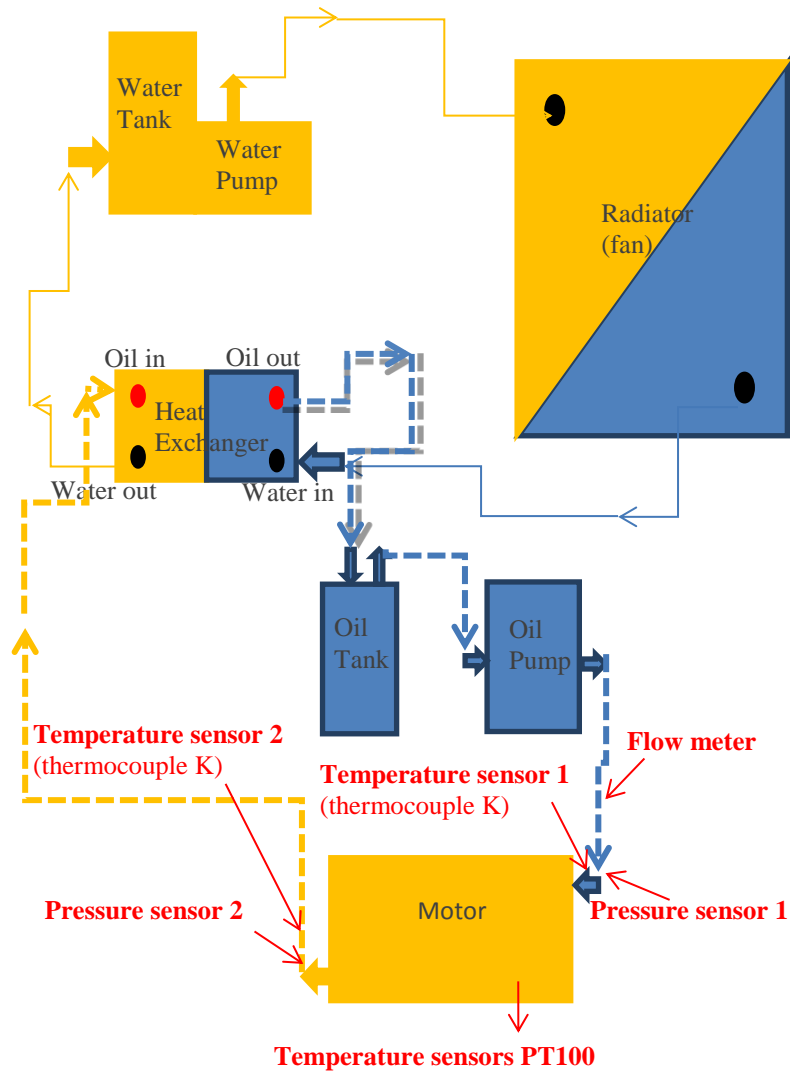


Figure 6.2 System drawing of test setup

Figure 6.2 shows the system drawing of hardware for electrical machine thermal test. The hardware contains the oil system with the oil flow

indicated by the dashed line arrows, the water system with the water flow indicated by the solid lined arrows and the sensors whose positions are shown by the red arrows. The oil system is used for electric machine cooling and the water system is used to cool the oil system through a heat exchanger and a radiator. Besides, the blocks in orange color indicate that the internal fluid are at high temperatures and the blocks in blue color indicate that the internal fluid are at low temperatures.

PT100 temperature sensors are embedded in the specific positions while the machines are manufactured and the sensor positions are discussed in chapter 6.2. The advantages of using PT100 resistance thermometers are (1) accuracy is high over quite high measured ranges (-200 to 850°C) [52] (2) don't require special connection cables as thermocouples do. However, the oil temperatures at the inlet and outlet of cooling systems are measured by thermocouple K because of its inexpensive, rigid with oil and wide measurement range between -200 and 1350°C [52]. The detailed instructions on components used for the thermal tests are shown below.

### 6.3 Hydraulic measurements

#### Gear pump

Marco UP3/Oil gear pump is used for the test. The rated voltage is 12VDC and rated current is 7.3A. The external gear pump has two gears working against each other. One gear is driven by a motor which is called drive gear and it in turn drives the driven gear. Each gear is supported by a shaft with bearings on both sides of the gear [54].

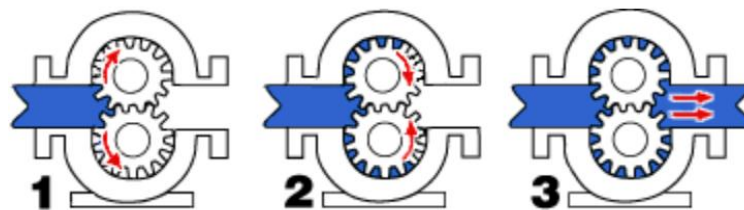


Figure 6.3 Working principle of a gear pump

Figure 6.3 shows the working principle of a gear pump, which contains the following three steps. (1) As the gears come out of mesh, they create expanding volume on the inlet side of the pump. Liquid flows into the cavity and is trapped by the gear teeth as they rotate; (2) Liquid travels

around the interior of the casing in the pockets between the teeth and the casing -- it does not pass between the gears; (3) Finally, the meshing of the gears forces liquid through the outlet port under pressure. [52]

### Flow meter

SF800 flow meter from Swissflow is used in the test system. Table 6.1 shows the applied range of this flow meter. The structure chart of the flow meter is shown in Figure 6.4. The applied excitation circuit is shown in the left picture of Figure 6.5.

Table 6.1 Flow meter range [52]

Range	
Flow rate [L/min]	0.5 to 20
Temperature [°C]	-20 to 90
Operating pressure [bar]	16
Max. pressure [bar]	40

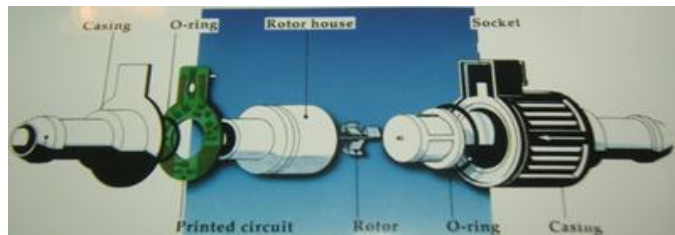
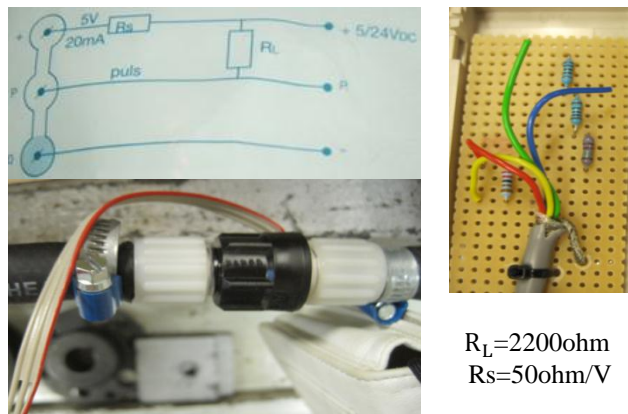


Figure 6.4 Structure chart of the flow meter



$$R_L = 2200 \text{ ohm}$$

$$R_s = 50 \text{ ohm/V}$$

Figure 6.5 Excitation circuit (left top and right) and SF800 flow meter (left bottom)

The output signal of the flow meter is a pulse train with a frequency that is proportional to the flow rate. Besides, according to the instruction, an output of 6000 pulses means 1 liter of fluid flowing through the flow meter. Therefore, if 100Hz is measured as the output of the flow meter, which means 100 pulses per second or 6000 pulses per minute, it corresponds to 1 L/min.

### Pressure meter

Two pressure sensors PSE563 from SMC are used to measure the pressures at the inlet and outlet of the electrical machine cooling system, separately.

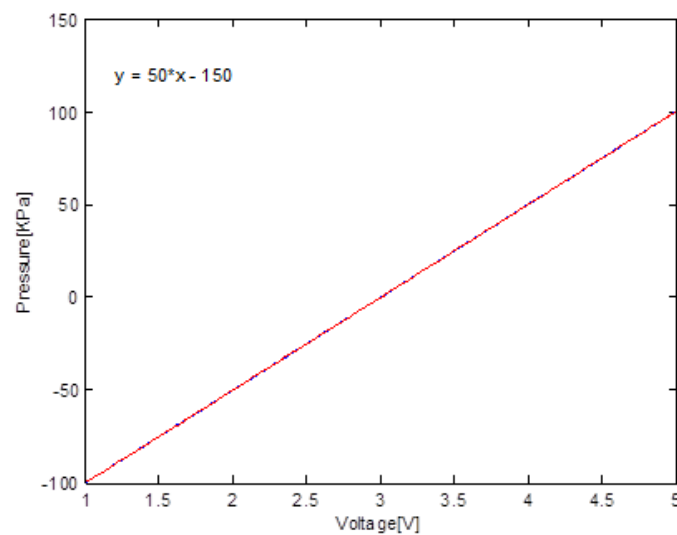


Figure 6.6 Output voltages correspond to pressures

The sensors output analog voltage between 1V and 5V which corresponds to the pressure between -100kPa to 100kPa as shown in Figure 6.6. The pressure differences between inlet and outlet are observed. According to the Figure 6.6, 3V is corresponding to 0Pa and every voltage change of 1V corresponding to 50kPa pressure change.

## 6.4 Temperature measurement

### Thermocouple type K

Two thermocouples of type K are used at the inlet and outlet of the cooling system in order to measure the coolant.

According to [55], the temperature versus voltage relationship of most of the thermocouples is not linear. However, according to Figure 6.7 thermocouple K approaches a constant over a temperature range from 0 degree C to 1000 degree C.

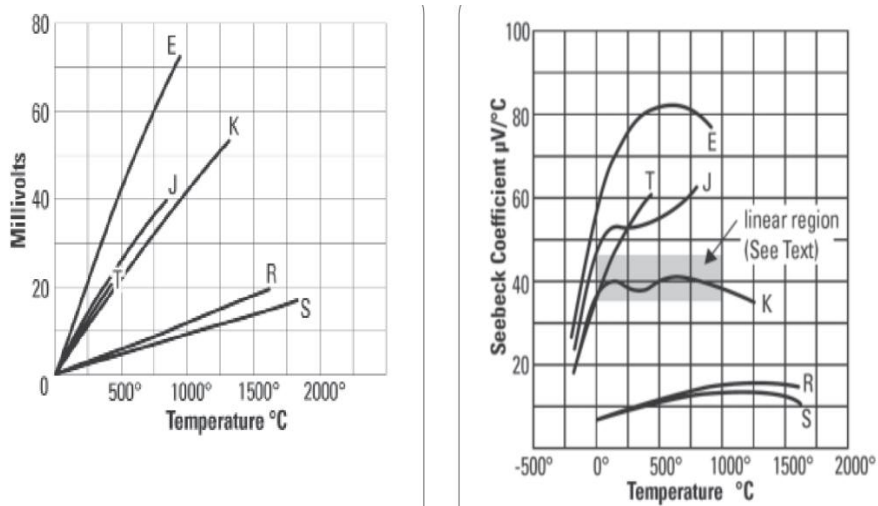


Figure 6.7 Thermocouple temperature vs. voltage graph(left), Seebeck coefficient vs. temperature

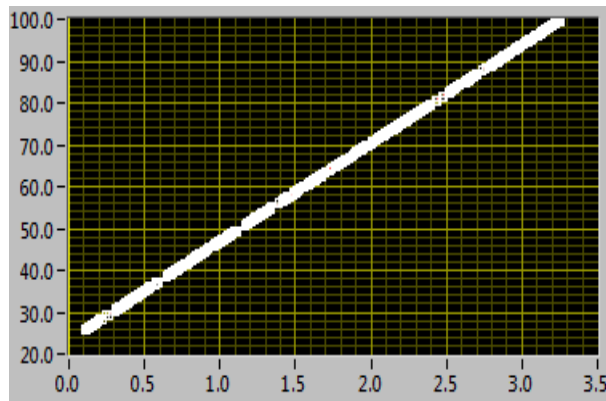


Figure 6.8 Measured samples for thermocouple type K

Figure 6.8 shows the calibration measurement samples for thermocouple type K. The x axis is the measured voltage, and the y axis shows the measured temperature for K type thermocouple. Therefore, Figure 6.7 shows the linear relation between the voltage and temperature for thermal couple K.

#### Pt100 temperature sensor

The specification of PT100 temperature sensor assembling is declared in this section.

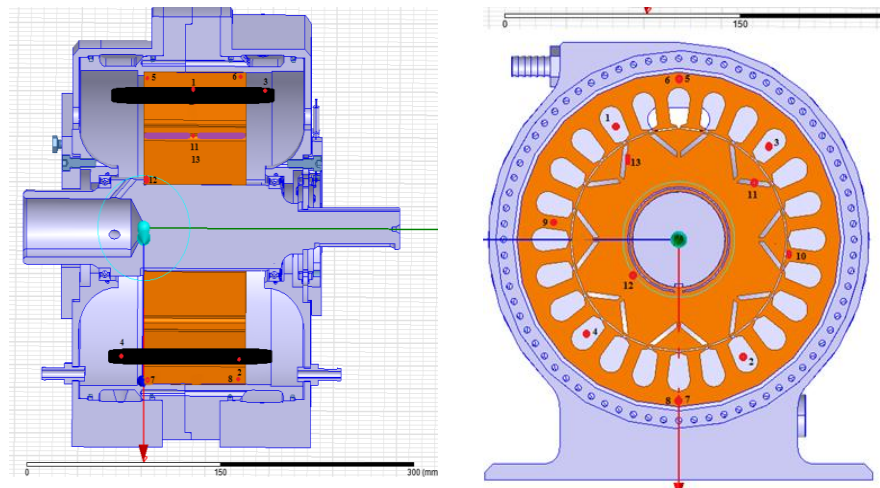


Figure 6.9 Pt100 sensors locations in tested electrical machines

There are 13 temperature sensors as shown in Figure 6.9, which are located in windings, stator yoke, stator teeth, magnets and rotor, separately. Table 6.2 outlines the Pt100 locations.

Table 6.2 Pt100 location list

No.	Location	No.	Location
1	Winding active part	2	Between active part and end part of the winding
3	Winding end part	4	Winding end part
5	Yoke (top)	6	Yoke (top)
7	Yoke (bottom)	8	Yoke (bottom)
9	Teeth	10	Teeth
11	Between magnets	12	Rotor
13	Between magnets		

Figure 6.10 and 6.11 show the measured temperatures while the machine is running as generator, but with different rotation speed. Figure 6.10 shows the active winding temperatures in Celsius versus time [hours] at electric frequency 200Hz. Figure 6.11 shows the yoke temperature and active winding temperatures at electric frequency 2.5Hz, which is the lowest speed that the machine is able to keep. The comparisons show that while the machine is running at low speed 2.5Hz, the applied torque is mainly used to overcome the friction, which will not lead to big iron losses, friction loss, therefore no big temperature rises. Hence the following tests are done with speed control at 2.5Hz combining with different currents control.

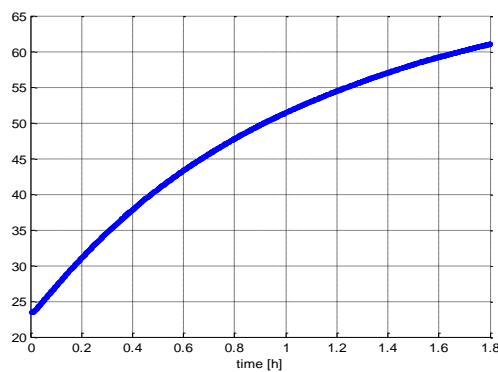


Figure 6.10 Active winding temperatures at electric frequency 200Hz



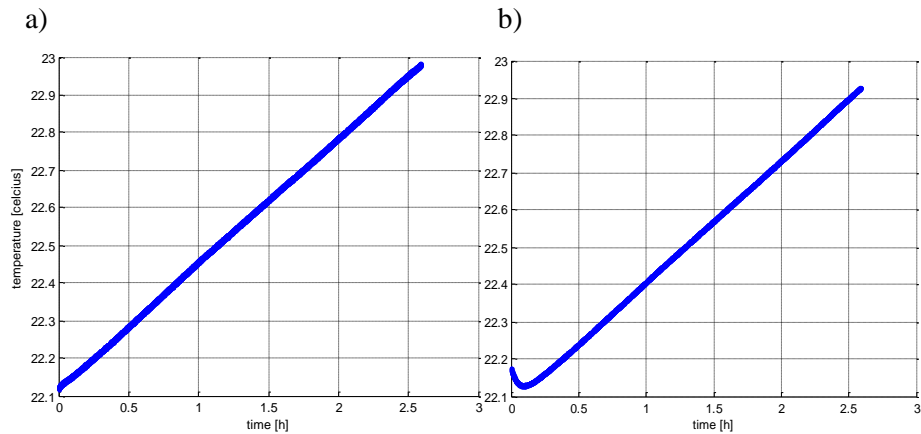


Figure 6.11 yoke (a) and active winding (b) temperatures with no current and electric frequency 2.5Hz

## 6.5 Summary

This chapter discusses the experimental goals and experimental setups including the test system and devices used for testing. For the test system part, the machine control principles are explained firstly. Then the FPGA implementations are stated. Furthermore, the devices for hydraulic measurements including gear pump, flow meter, and pressure meter and the devices for temperature measurements including thermocouple type K, Pt100 temperature sensor and slip ring unit are shown.



# Chapter 7

## Evaluation

This chapter presents the measurement results and calculation results.

### 7.1 Cooling system

As discussed in chapter 6, the cooling system measurements include the temperatures and pressures measured at the general inlet and outlet of the cooling systems.

#### Heat transfer coefficients

As discussed in chapter 3, the cooling channels for direct cooling system and indirect cooling system are designed to have the same total heat transfer coefficients. Therefore the temperature differences from the two machines are due to changing positions of the cooling channels and reducing the problem of unknown thermal resistance or air pocket between the housing and the stator.

According to forced heat transfer balance [28]

$$(T_{out} - T_{in}) \cdot c \cdot M = (T_s - T_{vf}) \cdot h_f \cdot A \quad 7.1$$

where  $T_{out}$  and  $T_{in}$  are the outlet and inlet temperatures of the cooling system,  $c$  and  $M$  are the specific heat and mass flow rate of the coolant,  $T_s$  is the cooling channel surface temperature,  $T_{vf}$  is the fluid volume temperature,  $h_f$  is the heat transfer coefficient and  $A$  is the wetted area.

Therefore, the heat transfer coefficients of the machine with two different cooling systems can be evaluated by

$$h_f = \frac{(T_{out} - T_{in}) \cdot c \cdot M}{(T_s - T_{vf}) \cdot A} \quad 7.2$$

Figures 7.1 and 7.2 show the coolant temperatures at the inlet and outlet of both the direct and indirect cooling systems while the current 31.15A and corresponding current density  $6.7\text{A}/\text{mm}^2$  are applied in windings. The two plots show that the average coolant temperature increases faster in the indirect cooling system comparing to those in direct cooling system. It is because the surface temperature  $T_s$  in Equation 7.2 is higher in the indirect cooling machine than it in the direct cooling machine. Therefore the coolant volume temperature  $T_{vf}$  is correspondingly higher in the indirect cooling machine. Figure 7.3 shows the ratio of average heat transfer coefficient of direct cooling system divided by the one of indirect cooling system. This plot indicates that the heat transfer coefficients of the two cooling systems are almost identical.

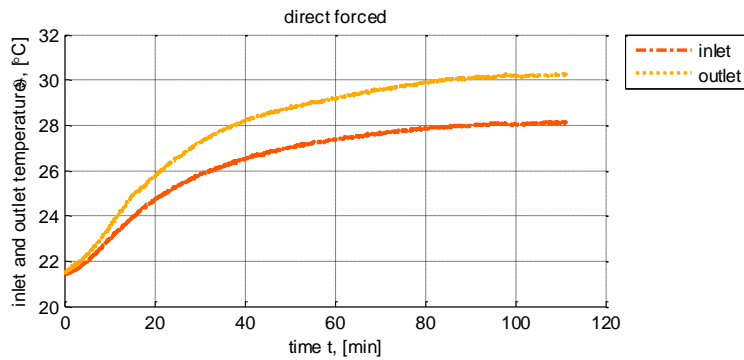


Figure 7.1 Inlet and outlet temperatures of machine for direct cooling system

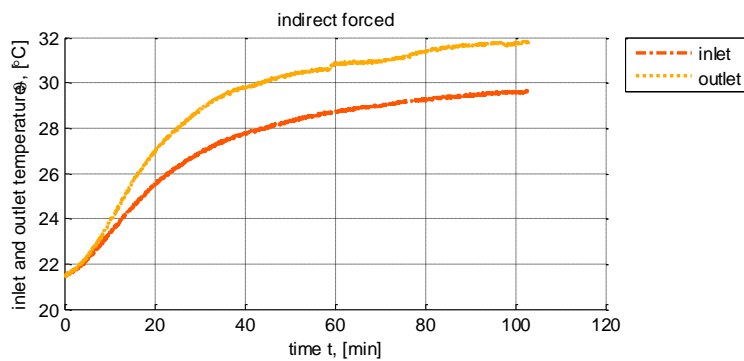


Figure 7.2 Inlet and outlet temperatures of machine with indirect cooling system

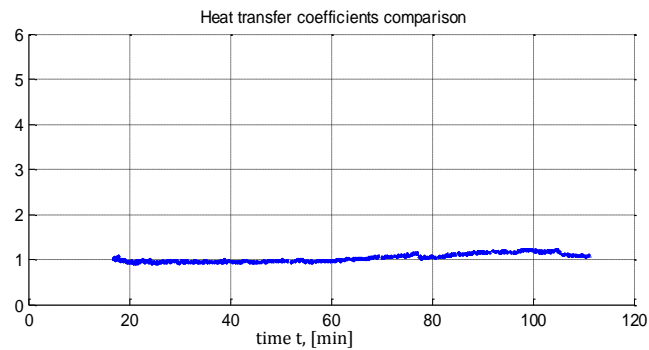


Figure 7.3 Average heat transfer coefficients ratio of direct and indirect cooling system

### Pressure drop test

As discussed in chapter 6, two pressure sensors are utilized at the inlet and outlet of the machine cooling system. There is no automatic control implemented for the gear pump, therefore simple manual control is used by setting the almost the same pumping power.

According to Equation 3.19, system pressure losses decrease with the decrease of coolant viscosity and density, which is due to the coolant temperature rise. At the same time, the same pumping power can push more coolant which leads to higher flow rate. This phenomenon is shown by figures 7.4 and 7.5. The x-axis shows the flow rates in L/min with temperature changing from 21°C to approximately 35°C and the y-axis shows the pressure losses of the two cooling systems.

Figure 7.5 shows that at the room temperature and flow rate 1.53L/min, the pressure loss of the direct cooling system is approximately 30kPa. Therefore, at room temperature with higher flow rate 2.75L/min, the pressure loss of the indirect cooling system will be 54kPa. However, at the steady state when the coolant temperature reaches 35°C, the pressure drops to approximately 20kPa with flow rate 2.75L/min. Hence, with the same flow rate 2.75L/min, the pressure losses at 21°C shows 2.7 times higher than that at 35°C, which is mainly caused by the viscosity changing from 219mm<sup>2</sup>/s to 105mm<sup>2</sup>/s and also a slightly density change.

Comparing the two cooling systems, at the steady state, the same flow rate but slightly lower pressure losses are obtained by the direct cooling

system.

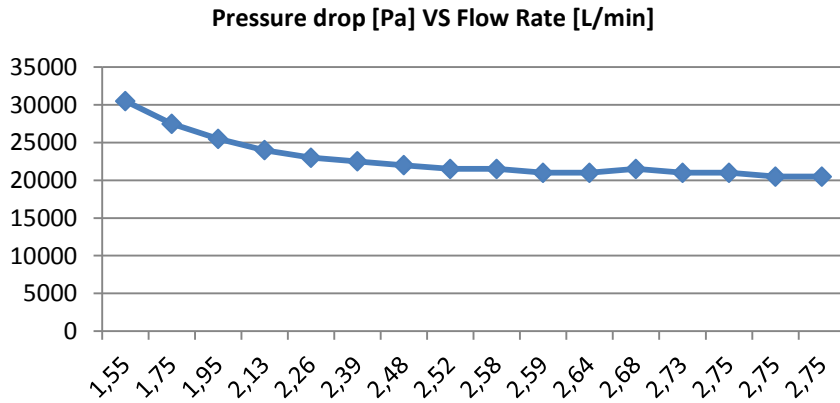


Figure 7.4 Pressure differences between inlet and outlet of indirect cooling system

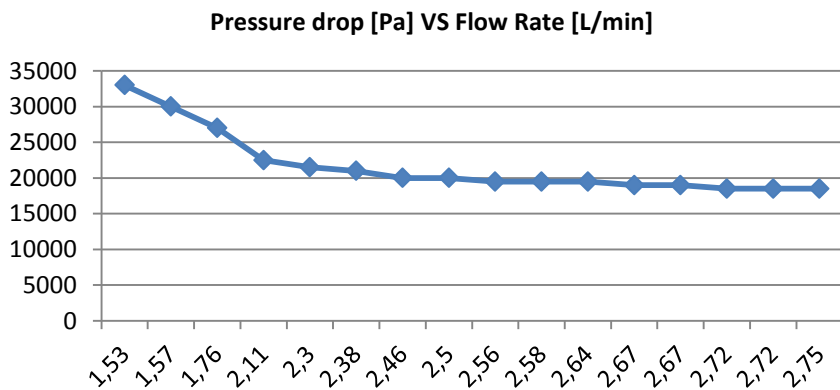


Figure 7.5 Pressure differences between inlet and outlet of direct cooling system

As shown in Figure 3.15, with total flow rate 1.7L/min and coolant density  $876\text{kg/m}^3$  and viscosity  $0.18\text{kg/s.m}$  at  $22^\circ\text{C}$ , the empirical calculations give  $27\text{kPa}$  and  $31\text{kPa}$  for a single channel in indirect system and direct cooling system, separately. However, the test results show that the total pressure drops is higher for the indirect cooling system than the direct cooling system. The reason is that indirect cooling system has double number of paralleled channels comparing to the direct cooling system. Therefore, the pressure losses due to division of coolant are higher, which lead to slightly higher total pressure losses in the indirect cooling system.

However, since the major part of the pressure losses are caused by the parallel channels, the total pressure drop of these two cooling systems should be similar with the same boundary conditions as shown by Figure 7.4 and 7.5.

The calculated and the tested pressure losses are in the same order of magnitudes, which means that the pressure calculation method can be used to evaluate the cooling system and choose the size of the pump.

## 7.2 Winding resistance test

As discussed in chapter 6, the machine tests are done under relatively low speed, hence the winding losses are dominating among the total losses. Therefore, winding resistances of the machines are important parameters to identify. This is done by continuously applying  $I_{sx}$  current from 0A to 70A forward and backward, meanwhile measure  $I_{sx}$  and  $U_{sx}$ . Thereafter the resistances are calculated by  $U_{sx}/I_{sx}$ . The top plot in Figure 7.6 shows the applied current. The x-axis shows the number of samples and the y-axis shows the current in A. The plot at the bottom of Figure 7.4 shows the temperature changes while the measurement is taken. After linear fitting for the measured currents and voltages, the phase resistances are found between 0.113 and 0.117 $\Omega$  for the temperature range of 24 to 34°C. Slightly higher resistances are obtained at higher temperatures. Furthermore, According to Equation 4.3, the calculated temperature coefficient of the tested windings is 0.004K<sup>-1</sup> which shows great agreement with the theoretical value. Thereafter, winding power losses at different current levels are calculated by Equation 4.1.

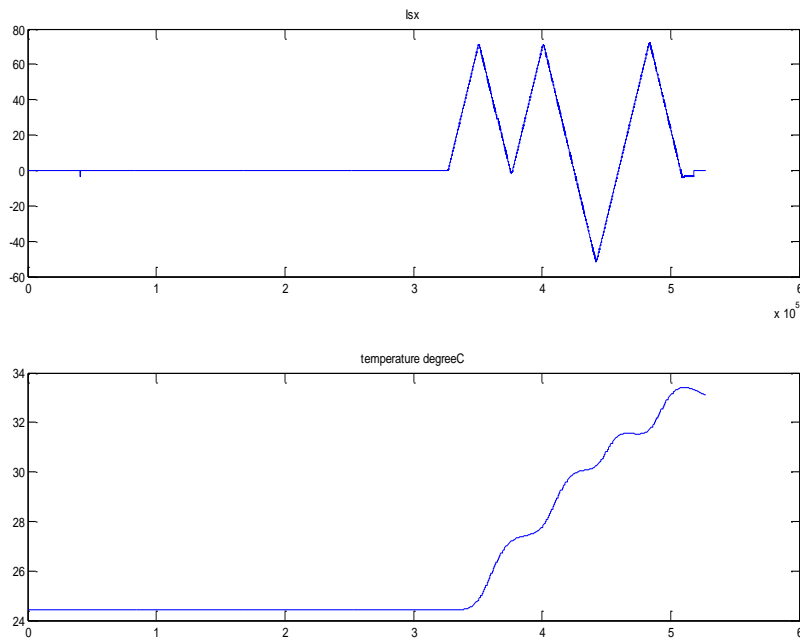


Figure 7.6 Isx current changing with time (top); winding temperature changing with time (bottom)

### 7.3 Temperature measurement results

#### Direct cooling VS indirect cooling

The following part discusses the differences between the direct oil cooled machine and indirect oil cooled machine at different current levels. Figures 7.7 to 7.10 show the temperatures of windings and housing stator interface, separately.



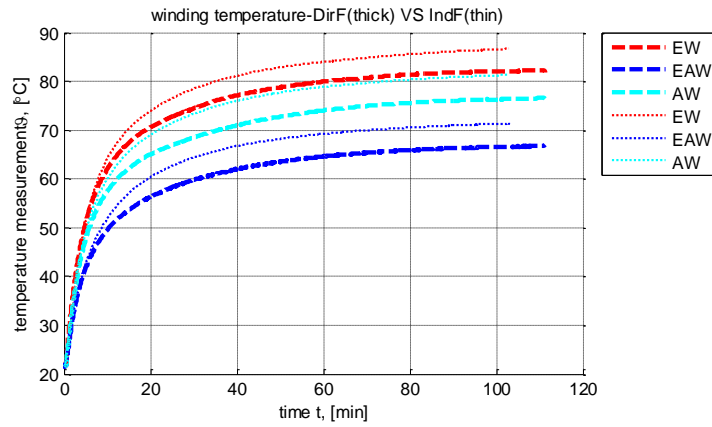


Figure 7.7 Winding temperature comparisons between direct cooled machine (thick lines) and indirect cooled machine (thin lines) at  $I=31.15A$

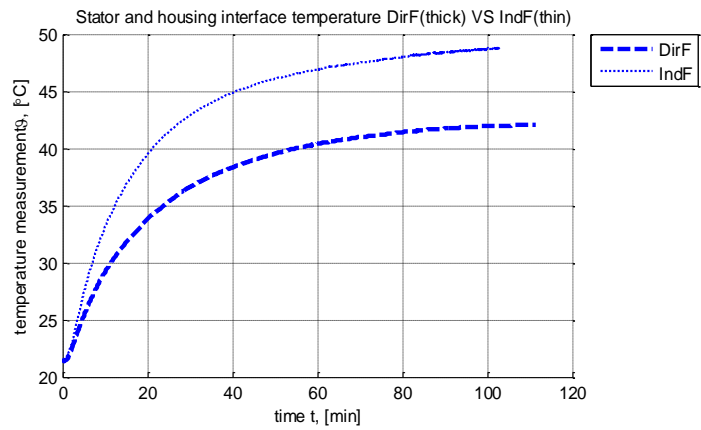


Figure 7.8 Stator and housing interface temperatures comparisons between direct (thick lines) and indirect cooled machine (thin lines) at  $I=31.15A$

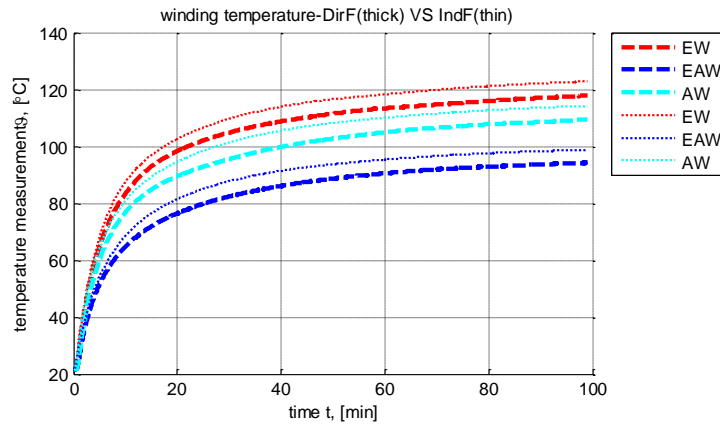


Figure 7.9 Winding temperature comparisons between direct (thick lines) and indirect cooled machine (thin lines) at  $I=37.8A$

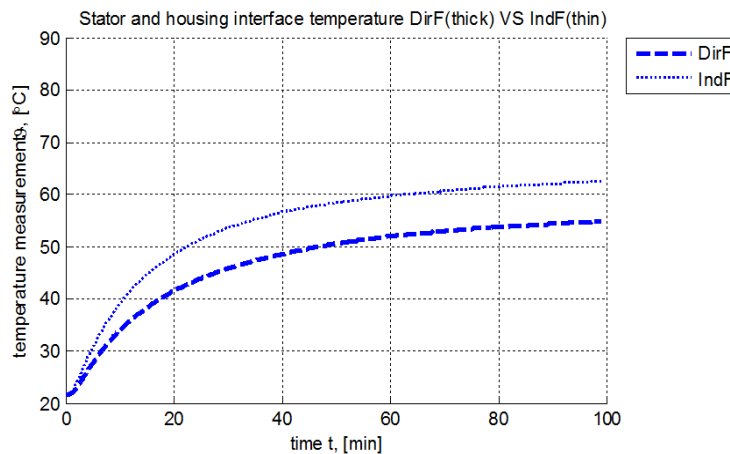


Figure 7.10 Stator and housing interface temperature comparisons between direct (thick lines) and indirect cooled machine (thin lines) at  $I=37.8A$

In the figures above, DirF means the direct cooled machine with forced cooling turned on and IndF means the indirect cooled machine with forced cooling turned on. EW represents the temperature measured in the middle of the end winding, AW represents the temperatures measured in the middle (in both axial and radial directions) of active winding and EAW represents the temperatures measured between the end winding and the active winding in the axial direction but close to the stator slot in the radial direction. Figure 7.11 shows the temperature sensor positions employed

for the end winding and slots cross sections. The winding temperature sensor positions are marked by the red stars. Besides, as shown in Figure 6.9 and Table 6.2, there are 4 temperature sensors which are embedded just between the stator and housing. The stator and housing interface temperatures shown in figures 7.8 and 7.10 are obtained by averaging the temperatures of the 4 sensors. Table 7.1 shows the steady state temperature comparisons at current 31.15A and 37.8A, which correspond to current density  $6.7\text{A/mm}^2$  and  $8.1\text{A/mm}^2$ , separately.

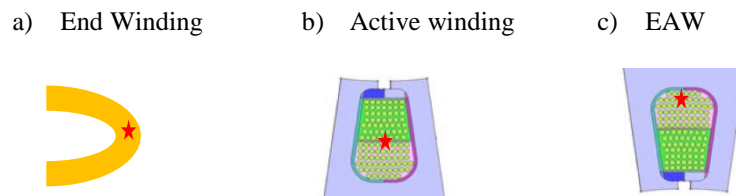


Figure 7.11 Winding temperature sensor positions

Table 7.1 Steady state temperature comparisons between direct cooled machine and indirect cooled machine with forced oil cooling turned on

Sensor positions	<b>I=31.15A, J=6.7A/mm<sup>2</sup></b>		
	Direct Forced [°C]	Indirect Forced [°C]	Difference
End winding	82.1	86.6	5.5%
Between EW and AW	66.6	71.3	7%
Active winding	76.3	81.3	6.6%
Stator and housing interface	41.9	48.8	16%
Sensor positions	<b>I=37.8A, J=8.1A/mm<sup>2</sup></b>		
	Direct Forced [°C]	Indirect Forced [°C]	Difference
End winding	117.7	122.8	4.3%
Between EW and AW	94.2	98.8	4.9%
Active winding	109.3	114.1	4.4%
Stator and housing interface	54.8	62.4	14%

As shown in the table above, the machine with direct cooling system shows better cooling performances than the one with indirect cooling system. For identical machine with the two different cooling systems, the temperature differences at stator and housing interfaces are 14% and 16% at two different current levels. Besides the temperature differences at windings vary from 4% to 7% at different locations.

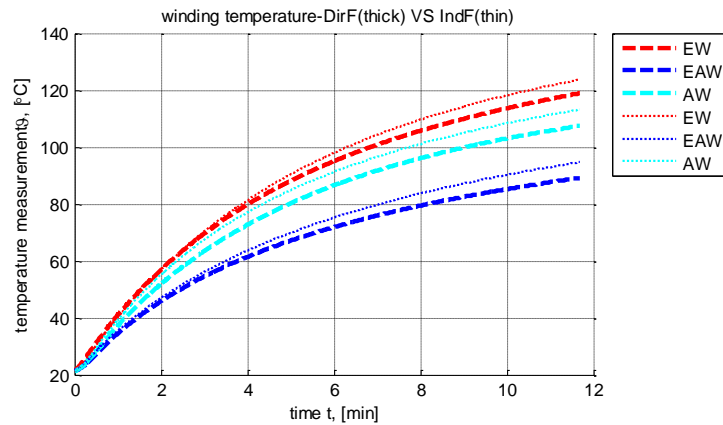


Figure 7.12 Winding temperature comparisons between direct cooled machine (thick lines) and indirect cooled machine (thin lines) at  $I=44.5A$

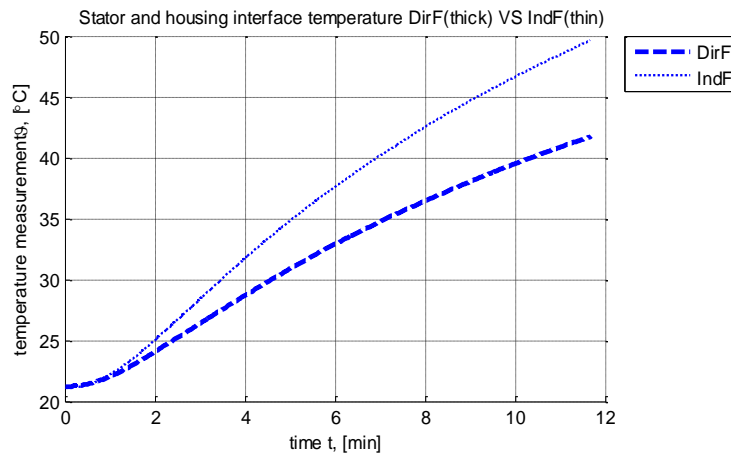


Figure 7.13 Stator and housing interface temperature comparisons between direct cooled machine (thick lines) and indirect cooled machine (thin lines) at  $I=44.5A$

Tests with higher current levels are also carried out and the results are shown in figures 7.12 to 7.13. However, since the maximum winding temperature during tests is set to 120°C, steady state temperatures at these current levels are not reached. But the machine with direct cooling system still shows better heat transfer performances than the one with indirect cooling system.

The maximum temperatures at different positions of the machines are compared in table 7.2. Before reaching the steady state, machine with direct cooling system already shows 3.3% to 6.2% better heat transfer performances than the one with indirect cooling system on winding temperatures and 19% differences on stator and housing interface temperature.

Table 7.2 Maximum temperature comparisons between direct cooled machine and indirect cooled machine with forced oil cooling turned on

Sensor positions	I=44.5A, J=9.6A/mm <sup>2</sup>		
	Direct Forced [°C]	Indirect Forced [°C]	Difference
End winding	119	123.6	3.3%
Between EW and AW	89.2	94.7	6.2%
Active winding	107.4	113.2	5.4%
Stator and housing interface	41.7	49.6	19%

### Forced cooling VS natural cooling

Figures 7.14 and 7.15 show the temperature differences in windings and stator housing interfaces between the machine with natural convection and machine with direct cooling system turned on but with the same applied current. From the comparisons one can see that forced cooling notably improves the machine heat transfer performance compared to natural cooling method.

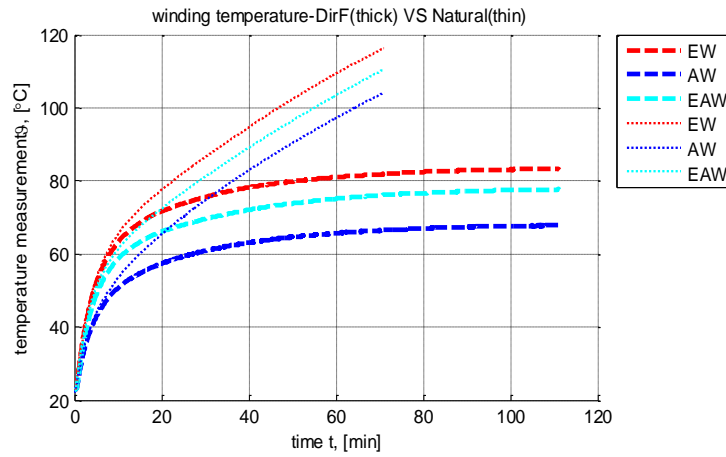


Figure 7.14 Winding temperature comparisons between direct oil cooled machine (thick lines) and natural cooled machine (thin lines) at  $I=31.15A$

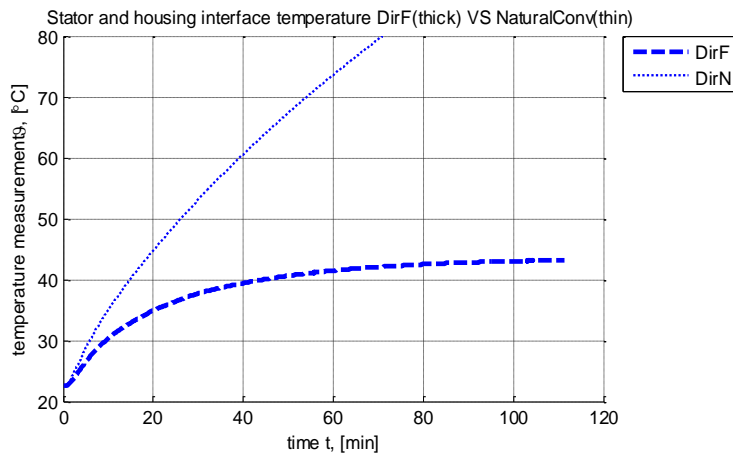


Figure 7.15 Stator and housing interface temperatures comparisons between direct cooled machine (thick lines) and natural cooled machine (thin lines) at  $I=31.15A$

### Measurement VS simulations

Table 7.3 shows the steady state temperature comparisons between the tests and FEM simulations. End winding temperatures (EW) and active winding temperatures (AW) are compared. The temperature comparisons at the position between the windings end part and active part (EAW) and the stator housing interface (SH interface) are discussed later on. Among

these cases, ‘Indirect Forced 1’ and ‘Indirect Forced 2’ represent the cases with air pocket between stator and housing 0.1mm and 0.05mm, respectively.

Table 7.3 Steady state temperature comparisons between test and FEM simulation

Sensor positions	Test		FEM		
	Direct Forced [°C]	Indirect Forced [°C]	Direct Forced [°C]	Indirect Forced 1 [°C]	Indirect Forced 2 [°C]
<b>I=31.15A, J=6.7A/mm<sup>2</sup></b>					
EW	82.1	86.6	85.6	90.6	89.1
AW	76.3	81.3	80	85	83.6
EAW	66.6	71.3	-	-	-
SH interface	41.9	48.8	30.9	-	35.8
<b>I=37.8A, J=8.1A/mm<sup>2</sup></b>					
EW	117.7	122.8	116.2	123.6	121.4
AW	109.3	114.1	107.9	115.3	113.2

From the comparisons one can observe that (1) for the machine with indirect cooling systems, results from simulation case named ‘Indirect Forced 2’, which has 0.05mm air pocket between the housing and the stator, are more close to the test results compared to results from the case named ‘Indirect Forced 1’. Therefore the estimation of the air pocket between the stator and the housing for the studied indirect cooled machine is approximately 0.05mm. (2) With applied current 31.15A, the errors between tests and simulations at end and active windings are 2 to 4°C. While at the other current level, the errors between tests and simulations at end and active windings are 1 to 2°C, which is smaller compared to the errors in previous case. In general, the comparisons in table 7.3 show good agreement on maximum end winding and active winding temperatures between tests and FEM steady state thermal calculations.

However, the temperature comparisons at the position between the windings end part and active part (EAW) is complex. Compared to the reality, the simulation simplifies the winding active part, which lumps all the winding impregnations and insulations together and considers them as one layer of equivalent winding insulation around the equivalent copper block. Therefore, as shown in Figure 5.3, the simulation results have the

tendency of showing a higher temperature gradient in the equivalent winding insulation layer but larger proportion of evenly distributed temperatures range in the equivalent copper block than in the real case. However, in the real case each winding strand has its own insulation which will 'lock' the heat inside the copper. Therefore, the most inner winding still sees the biggest amount of insulations around it, which leads to the maximum temperature in this winding. From this perspective, the maximum temperatures of the winding active part and end part are predicted quite well by this simplification method as shown in table 7.3, which are the main thermal stresses and concern for life time of the windings for the studied machines. Nevertheless, as shown in table 7.3, the measured steady state temperature at EAW (position is shown in Figure 7.11(c)) is 66.6°C for machines with applied current 31.15A and direct cooling systems. While the simulation shows the temperatures at the equivalent insulation layer are between 38 and 68°C from outer to inner as shown by Figure 5.3. The inner side temperature of the equivalent insulation layer is still quite close to the measured temperature.

As shown in figures 5.1 and 5.2, with applied current 31.15 A the simulated stator and housing interface temperatures are 30.9 and 35.8°C for direct and indirect cooled machines, separately. Compared to the measured interface temperatures 41.9 and 48.8°C with two different cooling systems, the simulation results show approximately 10°C lower at the same positions. However, the simulated volume average stator temperatures of the two machines are 39 and 42°C, respectively, which are closer to the test values. There are two factors which may lead to the differences. Firstly, the big differences between the interface temperatures and average temperatures in simulations may be caused by the smaller thermal conductivities of the stator iron applied in simulations than in reality. Secondly, the differences between the test and simulations are also due to elimination of iron losses and friction losses.

The predictions of maximum temperatures in winding end parts and active parts at steady state at higher applied currents are shown in table 7.4. The results clearly show that even with higher current applications, winding temperatures drop approximately 5% just by moving the cooling circuits closer to the stator. From a life time perspective, the directly cooled machine definitely works for longer time with winding insulation grade F than the indirectly cooled machine when 44.5 A current is applied.



Table 7.4 Steady state temperature predictions by 3D FEA simulations

FEM Sensor positions	I=44.5A, J=9.6A/mm <sup>2</sup>			I=55.7A, J=12.2A/mm <sup>2</sup>		
	Direct Forced [°C]	Indirect Forced [°C]	Diff	Direct Forced [°C]	Indirect Forced [°C]	Diff
EW	151.6	158.8	4.8%	233.3	245	5%
AW	140.2	147.6	5.3%	214.7	226.7	5.6%

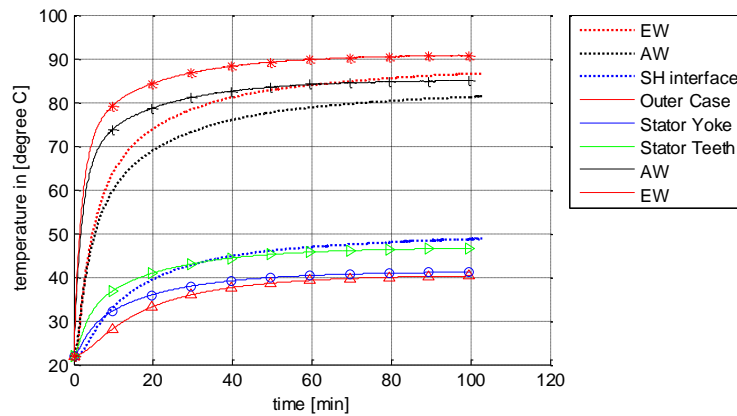


Figure 7.16 Transient temperature comparisons of machine with indirect cooling system: test results (dashed lines) with constant current I=31.15A and LPM results (solid lines) with constant losses for applied current 31.15A at 150°C

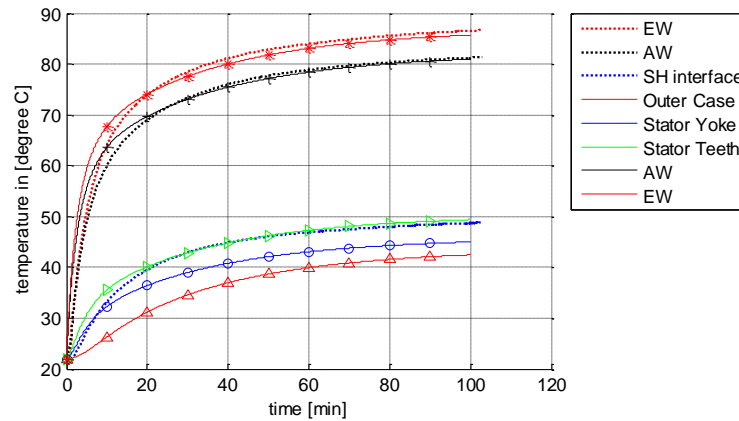


Figure 7.17 Transient temperature comparisons of machine with indirect cooling system: test results (dashed lines) and LPM results (solid lines) at I=31.15A and J=6.7A/mm<sup>2</sup>

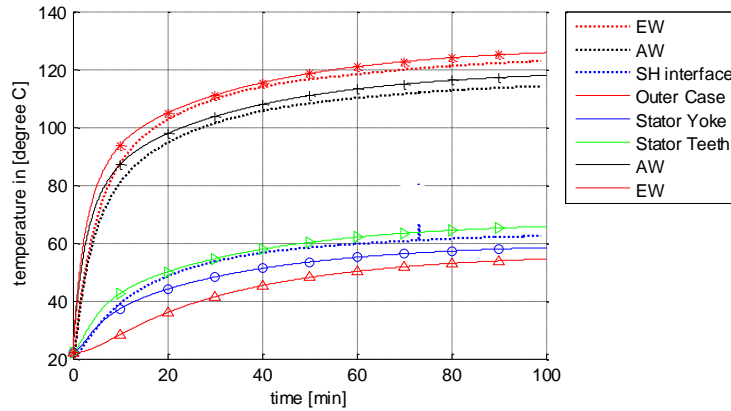


Figure 7.18 Transient temperature comparisons of machine with indirect cooling system: test results (dashed lines) and LPM results (solid lines) at  $I=37.8\text{A}$  and  $J=8.1\text{A}/\text{mm}^2$

Figures 7.16 to 7.18 show the transient temperature comparisons between test and LPM of machine with indirect cooling system. The dashed lines and the solid lines show the results from test and simulation, respectively. Besides, as stated before, EW and AW represent the temperatures obtained at winding end part and active part, separately. SH interface represents the temperature obtained at the interface between the stator and housing from test.

The dashed lines in Figure 7.16 show the temperature evolutions at the 8 nodes of the LPM based on the designed geometry and constant power losses when current 31.15 is applied at  $150^\circ\text{C}$ . Compared to the test which is conducted with constant applied current but increased power losses due to the increased temperature, the simulation results over-predict the losses and the temperature changing rate, i.e. the evolutions of winding temperature are faster by simulation.

Figure 7.17 and 7.18 show the temperature evolutions at the 8 nodes from the LPM with constant current applied. The winding loss at each time step  $k$  is updated based on the temperature obtained at time step  $k-1$ . The winding temperatures show great agreements between the test and LPM. However, the tested interface temperature between housing and stator shows approximately  $10^\circ\text{C}$  higher temperature than simulated housing temperature but closer to the simulated stator teeth temperature.

Figures 7.19 and 7.20 show temperatures obtained at the 8 nodes (as described in table 5.4) of the electrical machine with an indirect cooling system, with NEDC driving cycle and US06 driving cycle, separately. Compared to the results shown in figures 5.11 and 5.12 which are obtained with winding losses calculated at 150°C, the two plots below are obtained with the winding losses at time  $k$  updated depending on the winding temperatures at time  $k-1$ . Apparently, the results in figures 5.11 and 5.12 over estimate the hot spots temperatures in windings because of the overestimated losses.

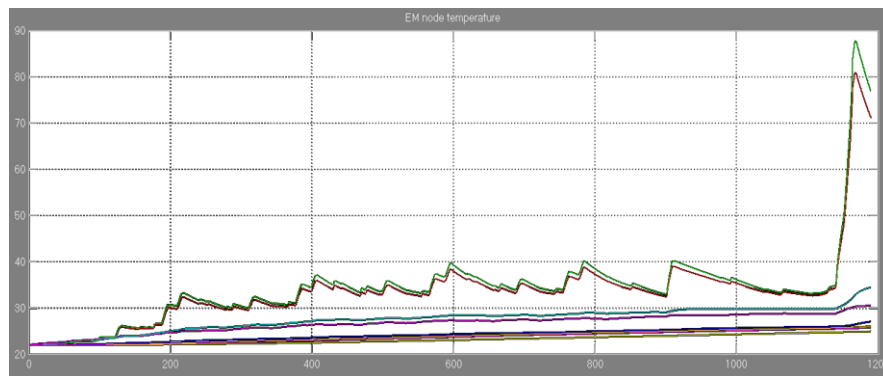


Figure 7.19 Temperatures of the machine with indirect cooling system and NEDC driving cycle

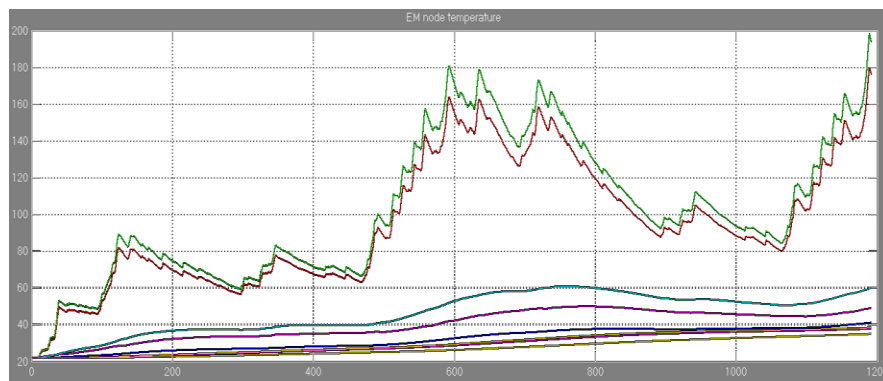


Figure 7.20 Temperatures of the machine with indirect cooling system and US06 driving cycle

## 7.4 Practical realization of cooling circuits

Figure 7.21 shows the design of direct cooling system for the electrical machine. The picture on the left side shows the complete cooling system before assembling. The picture on the right side shows the paralleled cooling channels which cover the active length of the electrical machine. The fact that the internal structure of the cooling circuit is different does not affect the size or exterior of the two machine designs. Figure 7.22 shows the exterior looks of the two machines. Besides, the manufacture process of cutting cooling grooves for direct cooling system is easier than drilling holes inside housing for indirect cooling system. However, machine with direct cooling system requires good sealing to avoid the leakage.

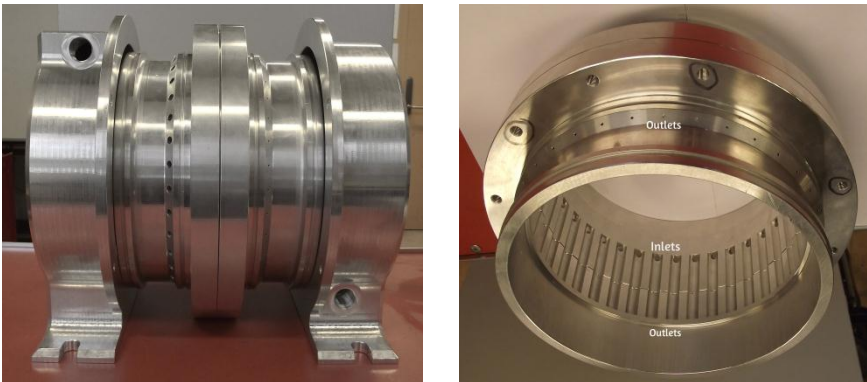


Figure 7.21 Pictures show the design of direct cooling system for the electrical machine

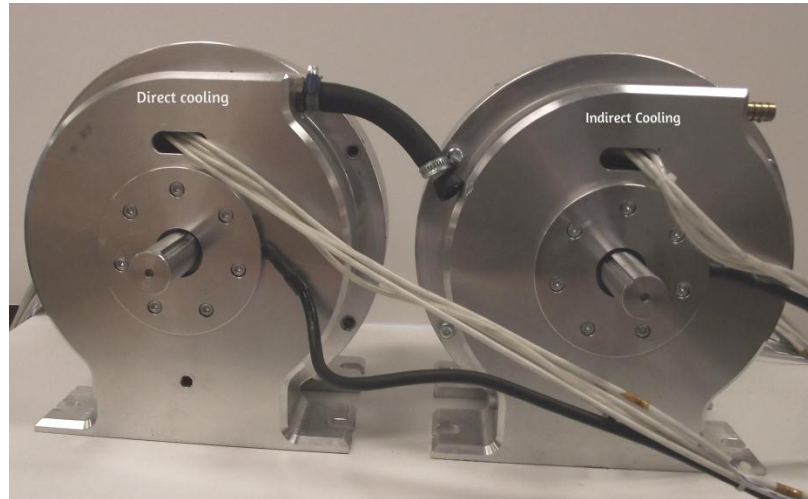


Figure 7.22 Pictures of the machines with direct (left) and indirect (right) cooling systems

## 7.5 Summary

This chapter presents the differences in heat transfer performances between the machines with direct cooling system and indirect cooling system by tests and simulations. Winding temperatures of machine with indirect cooling system show 3% to 7% higher than the machine with direct cooling system depending on the applied current and locations of temperature sensors in windings. At the same time, the temperature at the stator and housing interface is 14% to 19% higher in the machine with indirect cooling system than the one with direct cooling system. The simulation results show good agreements to the tested results on the hot spot temperatures obtained at windings. Besides, the calculated pressure losses show the same order of magnitude as the test values.

Both the applied FEA and LPM methods show quite good accuracy on predicting the hot spot temperatures in winding after small calibration. The calibrations are mainly for the end windings. The winding active length is known when the motor is designed. At the same time, the end winding axial length can be obtained from the manufacturer. However, it is hard to predict how and to what extent the end windings are bended and squeezed during manufacturing process. Therefore, the end winding fill factor and the size of end winding block need to be calibrated after the machine is

made.

Comparing to the LPM thermal models, FEA models have the advantage of making steady state sensitivity study on quite detailed changes of designs. For instance, it is able to predict the differences between the machines with direct cooling system and indirect cooling system even though the geometry difference is not notable just by moving the cooling channels position for millimeters and taking away the thin layer of air pocket between stator and housing. Since LPM represents the whole machine by several nodes and the thermal resistances and capacitances are calculated as a bulk of materials between every two nodes, it has a difficulty to predict the differences on such small changes on designs as mentioned above. However, the LPM is quite convenient for transient temperature predictions and further applications with driving cycles.

# Chapter 8

## Conclusions

### 8.1 Reflections

Direct forced cooling system for permanent magnet synchronous electrical machines applied in HEVs and ZEVs is studied. Comparisons between this approach and the indirect forced cooling approach are done by both simulation and test. The results show 4 to 7% improvement for winding temperatures and 14 to 16% improvement for housing and stator interface temperatures for machine with direct cooling system.

Based on the studied objects, the mechanisms of heat transfer and fluid dynamics are well studied and understood. Besides, choosing among different options for heat transfer models is quite important. The final choice should be decided not only by the cost, i.e. computational time and computer resources, but also by the target of a certain thermal analysis. For example, if the differences between the machines with direct and indirect cooling system are interested, steady state FEA simulation is good enough to estimate the differences. On the other hand, simplified LPM may not have the ability to further investigate such a detailed position change of cooling channels. However, if the dynamic temperature distributions and studies on life time of electrical machines are interested, fast transient thermal analysis such as LPM with drivetrain control algorithm must be involved. CFD is a good choice if design of cooling circuits or finding out heat transfer coefficients at the interfaces between fluid and solid are interested.

Temperature evolutions while driving with different driving cycles are studied based on the loss maps obtained from FEA electromagnetic

analysis and ‘translated’ LPM. The results can be used (1) to choose the proper insulation grade of the winding and (2) aging of insulation materials, as well as (3) life time of electrical machine and its mounted system.

A hydraulic equivalent circuit is built and studied in this thesis. It is made with the purposes of analyzing the flow network. Design and size of each cooling channel directly influences the hydraulic resistance, furthermore, the flow distributions, total pressure losses and heat transfer performance. In this study, a “bottleneck” at the outlet of each paralleled cooling channel leads to evenly distributed flow in each channel, which results in evenly distributed heat transfer over the machine stator. The disadvantage of this solution is that it increases the cost in terms of pressure loss, i.e. pumping power. Other suggested solutions are to increase the size of the inlet and outlet coolant collector or make stair design for the two collectors. These solutions may lead to slightly bigger size cooling systems comparing to the design in this study but cost less.

Temperature measurements for electrical machines are made with PT100 sensors. The sensors should be put in the positions whose temperatures are most interested - may be the hot spots. Temperature sensors in the windings should be carefully placed since the temperature gradients are big along the direction which is perpendicular to the current flow. Besides, temperature, flow rate and pressure loss measurements are made at the general inlet and outlet with the purpose of studying different cooling systems. The measurement results are processed manually because of the limit of the equipment, which can be improved in the future.

## **8.2 Future work**

Temperature evolutions with driving cycles can be used in material and system life time study as discussed in 8.1. In order to do so, thermal models which are able to accurately predict machine temperatures at various combinations of speed and torque are needed. Additionally, accurate thermal models require two essential factors namely losses, thermal resistances and capacitances matrixes. Therefore the future work of more accurate thermal model development could focus on improving the accuracy of these two factors.

On one hand, since the studies in this thesis are focused on low speed and



---

almost zero torque applications, losses in the rotor laminations and magnets and mechanical losses are ignored. These losses need to be studied in the future.

On the other hand, in a LPM, the thermal resistances and capacitances matrixes are dependent on the chosen nodes and the geometries in between every two nodes and also derived from material properties and heat transfer coefficients. The more nodes that are chosen for the LPM, the more node temperatures can be obtained, and also the easier it is to obtain the lumped resistance and capacitance parameters between two nodes since fewer parts are lumped. Thus a more accurate model is obtained – provided that the thermal parameters can be correctly identified or calculated.

Besides, since electrical machines in vehicle applications are controlled by power electronics, a thermal study on thermal behavior of the whole drive system is an interesting future work.

There are several aspects can be improved for temperature measurements of electrical machines. As mentioned before, the measurement of hydraulic system can be improved in a way that the hydraulic pump is controlled and the collection of measured data can be done automatically. Secondly, PT100 inside the machines, especially at the places with big temperature gradients, should be carefully placed, in order to have a good comparison between the test and simulation results. Thirdly, the rotor temperature measurement needs to be studied more in the future work.



## References

- [1] Remy Inc, "Multi-set rectangular copper hairpin windings for electric machines", Pat-ent No. US 6,894,417 B2.
- [2] [http://www.copper.org/applications/electrical/energy/motor\\_text.html](http://www.copper.org/applications/electrical/energy/motor_text.html), access date, 07/03/13.
- [3] R. Saidur, "A review on electrical motors energy use and energy savings", *Renewable and Sustainable Energy Reviews*, 14 (2010) 877–898.
- [4] <http://www.winnerscience.com/tag/definition-soft-magnetic-materials/>, access date 08/03/13.
- [5] Professor Edward Price, "Magnetic dipoles, hysteresis and core losses", copyright 2006, p. 5.
- [6] B. Sunden, "Introduction to Heat Transfer", text book, 2006.
- [7] Geankoplis, Christie John (2003). *Transport Processes and Separation Process Principles*. Prentice Hall Professional Technical Reference. ISBN 0-13-101367-X.
- [8] Cengel, Yunus A, "Introduction to thermodynamics and heat transfer" (2nd ed.), McGraw-Hill Science/Engineering/Math, 2007, page 589.
- [9] [http://en.wikipedia.org/wiki/Litz\\_wire](http://en.wikipedia.org/wiki/Litz_wire), access date, 11/03/13.
- [10] <https://www.dcpowerinc.com/dc-power-vs-competition>, access date, 12/03/13.
- [11] Adrianus W. van Gils, "Laminated winding for electric machines", United States Patent, patent number 4319152, issued date, March 1982.
- [12] Conny Högmark, Rasmus Andersson, Avo Reinap, Mats Alaküla, "Electrical machine with laminated winding for hybrid vehicle applications", 2nd International Electric Drive Production Conference (EDPC), October 2012.
- [13] V.IANCU, T.CANTA, D.C.POPA, L.SZABO, "Soft magnetic composites used for iron core of the electrical machines", Technical University of Cluj-Napoca
- [14] Shafiqh Nategh, Oskar Wallmark, Mats Leksell, "Evaluation of Impregnation Materials for Thermal Management of Electric Machines", submitted to IEEE Transactions on Energy Conversion.
- [15] [http://www.micronal.de/portal/load/443847/BASF\\_Micronal\\_PCM\\_Brochure%202009\\_English.pdf](http://www.micronal.de/portal/load/443847/BASF_Micronal_PCM_Brochure%202009_English.pdf), access date, May 2013
- [16] [http://multimedia.3m.com/mws/mediawebserver?mwsId=sssss72sFWtTz8UuoY9zpY\\_sFWuRFWtsFWtsFWtsFsssss--&fn=bro\\_heattrans.pdf](http://multimedia.3m.com/mws/mediawebserver?mwsId=sssss72sFWtTz8UuoY9zpY_sFWuRFWtsFWtsFWtsFsssss--&fn=bro_heattrans.pdf), access date May 2013.
- [17] Zhe Huang, Shafiqh Nategh, Mats Alaküla, Viktor Kassila, Jinliang Yuan, "Direct Oil Cooling of Traction Motors in Hybrid Drives", IEEE International Electric Vehicle Conference (IEVC), Greenville, SC, 2012.
- [18] Zhe Huang, Francisco Marquez, Mats Alaküla, Jinliang Yuan, "Characterization and Application of Forced Cooling Channels for Traction Motors in HEVs", XXth International Conference on Electrical Machines (ICEM), Marseille, 2-5 September 2012.
- [19] Hector Zelaya De La Parra, Freddy Magnussen, Sjoerd Bosga, ABB Coporate Research, "Challenges for Electric Machines and Power Electronics in Automotive Applications", Ecologic Vehicles & Renewable Energy (EVER) conference, 2009.
- [20] John Hsu, Curtis Ayers, Chester Coomer, "Thermal control for power electronics and motors", Oak Ridge National Laboratory, FY 2006 progress report.
- [21] Francisco Marquez, Avo Reinap, Mats Alaküla, "Design, optimization and construction of an electric motor for an Electric Rear Wheel Drive Unit application for a Hybrid Passenger Car", 19th International Conference on Electrical Machines (ICEM), Rome, Italy, 2010.

- [22] Francisco Marquez, Zhe Huang, Mats Alaküla, "Redesign of an Electrical Rear Wheel Drive (E-RWD) for a hybrid vehicle in a given drive cycle", XXth International Conference on Electrical Machines (ICEM), Marseille, 2-5 September 2012.
- [23] Jiyuan Tu, Guan Heng Yeoh and Chaoqun Liu, 'Computational Fluid Dynamics- A Practical Approach', 2007, ISBN: 978-0-7506-8563-4, page 65.
- [24] Aldo Boglietti, Senior Member, IEEE, Andrea Cavagnino, Member, IEEE, David Staton, Martin Shanel, Markus Mueller, and Carlos Mejuto, "Evolution and Modern Approaches for Thermal Analysis of Electrical Machines", IEEE Transactions on Industrial Electronics, VOL.56,NO.3, March 2009.
- [25] J. Muggleston, S. J. Pickering, and D. Lampard, "Effect of geometric changes on the flow and heat transfer in the end region of a TEFC induction motor," in Proc. 9th IEEE Int. Conf. Elect. Mach. Drives, Canterbury, U.K., Sep. 1999, pp. 40–44.
- [26] D. Staton, S. J. Pickering, and D. Lampard, "Recent advancement in the thermal design of electric motors," in Proc. SMMA—Fall Tech. Conf., Durham, NC, Oct. 3–5, 2001.
- [27] R. K. Shah and M. S. Bhatti. "Laminar Convective Heat Transfer in Ducts." In Handbook of Single-Phase Convective Heat Transfer, ed. S. Kakaç, R. K. Shah, and W. Aung. New York: Wiley Interscience, 1978.
- [28] W. M. Kays and M. E., "Crawford. Convective Heat and Mass Transfer", 2nd edition, New York: McGraw-Hill, 1980.
- [29] Arthur Akers, Max Gassman, and Richard Smith, "Hydraulic Power System Analysis", 2006, chapter 13.
- [30] David A. Staton and Andrea Cavagnino, Member, IEEE, "Convection Heat Transfer and Flow Calculations Suitable for Electric Machines Thermal Models", IEEE TRANSACTIONS ON INDUSTRIAL ELECTRONICS, VOL. 55, NO. 10, OCTOBER 2008.
- [31] Brian J. Kirby, Cornell University, "Micro- and Nanoscale Fluid Mechanics, TRANSPORT IN MICROFLUIDIC DEVICES", Cambridge university press, 2010, chapter 3.
- [32] Ramesh K. Shah, Dusan P. Sekulic, "Fundamentals of Heat Exchanger Design", chapter 6, ISBN 0-471-32171-0, 2003.
- [33] "Heat Exchanger Design Handbook, volume 3, Thermal and hydraulic design of heat exchangers", Hemisphere Publishing Corporation, 1983.
- [34] Frank M. White, 'Fluid Mechanics', fourth edition, chapter 6.
- [35] F. Marquez-Fernandez, A. Reinap, Z. Huang, M. Alakula, "Dynamic Evaluation of the Overloading Potential of a Convection Cooled Permanent Magnet Synchronous Motor", 2011 IEEE International Electric Machines & Drives Conference (IEMDC).
- [36] Dellinger, J.H., "The temperature coefficient of resistance of copper", Journal of the Franklin Institute, September 1910, 170(3):213-216.
- [37] Wenliang Chen, "Analysis of AC copper losses in form-wound stator windings of high speed machines", KTH, Stockholm 2010.
- [38] H. Gavrilă, V. Ionita, "Crystalline and amorphous soft magnetic materials and their applications—status of art and challenges", June 2002.
- [39] James L. Kirtley Jr., "Class Notes 3: Eddy Currents, Surface Impedances and Loss Mechanisms", 2005.
- [40] Mats Alaküla, Per Karlsson, "Power Electronics-Devices, Converters, Control and application", Department of Industrial Electrical Engineering and Automation, Lund University.
- [41] Professor Edward Price, "Magnetic dipoles, hysteresis and core losses", copyright 2006, p. 5.
- [42] N. Mohan, T. Undeland and W.P. Robbins, "Power Electronics: Converters, Applications, and Design", 2nd edition, John Wiley and Sons, Inc., New York, NY, USA, 1995.
- [43] The Japan Research Institute, Limited Engineering Technology Division, "Loss Calculation Method", 2005.
- [44] D.Lin, Q.M. Chen, "Core Loss Calculation in Maxwell 3D&2D", Ansoft Corporation.
- [45] Dr. Martin März, Paul Nance, "Thermal modeling of power-electronic systems".
- [46] Joachim Lindström, "Development of an experimental permanent-magnet motor drive", Technical report No. 312L, P77.

- 
- [47] Ayman M.EL-Refai, Student Member, IEEE, Nathan C. Harris, Thomas M. Jahns, Fellow, IEEE, and Khwaja M. Rahman, Member, IEEE, "Thermal analysis of multibarrier interior PM synchronous machine using lumped parameter model", IEEE Transactions on energy conversion, VOL. 19, No. 2, June 2004
  - [48] Shafiqh Nategh, Andreas Krings, Zhe Huang, Oskar Wallmark, Mats Leksell and Magnus Lindenmo, "Evaluation of stator and rotor lamination materials for thermal management of a PMaSRM", 20th International Conference on Electrical Machines (ICEM), Marseille, 2-5 September 2012.
  - [49] Shafiqh Nategh, Student Member, IEEE, Oskar Wallmark, Member, IEEE, Mats Leksell, Member, IEEE, and Shuang Zhao, *Student Member, IEEE*, "Thermal Analysis of a PMaSRM Using Partial FEA and Lumped Parameter Modeling", IEEE Transactions on energy conversion, VOL. 27, NO. 2, June 2012
  - [50] Yury Loayza, Avo Reinap, Mats Alakula, "Performance and efficiency evaluation of FPGA controlled IPMSM under dynamic loading", 2011 IEEE International Symposium on Diagnostics for Electric Machines, Power Electronics & Drives (SDEMPED).
  - [51] Mats Alakula and Per Karlsson, "Power Electronic-Devices, Converters, Control and Applications", Lund University, department of Industrial Electrical Engineering and Automation.
  - [52] <http://www.picotech.com/applications/pt100.html>, access date May 2013.
  - [53] R.P. Benedict, "Manual on the use of thermocouples in temperature measurement", Philadelphia: American soc. for testing and materials, 1981.
  - [54] "How External Gear Pumps Work", <http://www.pumpschool.com/principles/external.htm>, access date May 2013.
  - [55] "Practical Temperature Measurements Application Note 290", <http://cp.literature.agilent.com/litweb/pdf/5965-7822E.pdf>, access date 2013, 05.
  - [56] "Numerical modelling and design of electrical devices", Project 1.0101-0278, Application of interdisciplinary and international team and project based learning in Master Studies.



# Abbreviations

## Acronyms

AC	Alternating Current
CFD	Computational Fluid Dynamics
DC	Direct Current
E-RWD	Electrical Rear Wheel Drive
FEA	Finite Element Analysis
HEV	Hybrid Electric Vehicle
ZEV	Zero Emission Vehicle
HEC	Hydraulic Equivalent Circuit
IPMSM	Interior Permanent Magnet Synchronous Machine
LPM	Lumped Parameter Model
MMF	Magneto Motive Force
NEDC	New European Driving Cycle
PDE	Partial Differential Equation
PM	Permanent Magnet
PMSM	Permanent Magnet Synchronous Machine
SbTCM	Silicone based Thermal Conductive Material

SMC	Soft Magnetic Composites
-----	--------------------------

## Symbols

Symbol	Unit	Definition
$A$	$m^2$	Surface area
$a$	$m^2/s$	Thermal diffusivity
$B$	T	Flux density
$B_m$	T	Maximum flux density
$c$	J/(kg K)	Specific heat
$D_h$	m	Hydraulic diameter
$F$	N	Force
$f$	-	Darcy friction factor
$f_r$	Hz	Frequency
$H$	A/m	Magnetic field intensity
$h_f$	W/(m <sup>2</sup> K)	Heat transfer coefficient
$I$	A	Current
$J$	A/m <sup>2</sup>	Current density
$J_{in}$	kg/m <sup>2</sup>	Inertia
$K_c$	-	Contraction loss coefficient
$K_e$	-	Expansion loss coefficient



$K_b$	-	Bending loss coefficient
$k_e$	-	Eddy current losses coefficient
$k_h$	-	Hysteresis losses coefficient
$L$	m	Length
$M$	kg/s	Mass flow rate
$P_{DC}$	W	DC current losses
$p$	Pa	Pressure
$\Delta P_f$	Pa	Pressure drop due to friction
$\Delta P_b$	Pa	Pressure drop due to bending
$\Delta P$	Pa	Total pressure drop
$Pr$	-	Prandtl number
$P_t$	W	Total iron loss
$P_h$	W	Hysteresis loss
$P_e$	W	Eddy current loss
$P_{ex}$	W	Excess loss
$q$	W/m <sup>2</sup>	Heat flux
$Q$	m <sup>3</sup> /s	Flow rate
$Q'$	W/m <sup>3</sup>	Internally generated volume heat
$Re$	-	Reynolds number
$R_{el}$	$\Omega$	Electrical resistance

$R_{el_r}$	$\Omega$	Reference electrical resistance
$T$	$^{\circ}\text{C}$	Temperature
$T_s$	$^{\circ}\text{C}$	Surface temperature
$T_{vf}$	$^{\circ}\text{C}$	Fluid volume temperature
$T_{out}$	$^{\circ}\text{C}$	Outlet temperature
$T_{in}$	$^{\circ}\text{C}$	Inlet temperature
$u$	m/s	Velocity in x direction in Cartesian coordinate system
$v$	m/s	Velocity in y direction in Cartesian coordinate system
$w$	m/s	Velocity in z direction in Cartesian coordinate system
$\mu$	kg/(m s)	Dynamic viscosity
$\mu_0$	H/m	Magnetic permeability of free space
$\mu_r$	-	Relative permeability of conducting material
$V$	$\text{m}^3$	Volume
$\mathcal{V}_m$	m/s	Mean velocity
$\lambda$	W/(m K)	Thermal conductivity
$\alpha_r$	1/K	Temperature coefficient of resistance for conductor material
$\partial_1, \partial_2$	-	Material dependent hysteresis loss constants
$\sigma$	-	Area ratio

---

---

$\delta$	-	Height width ratio
$\rho$	kg/m <sup>3</sup>	Density
$\rho_i$	kg/m <sup>3</sup>	Pipe inlet density
$\rho_o$	kg/m <sup>3</sup>	Pipe outlet density
$\rho_e$	$\Omega$ m	Electrical resistivity
$\sigma_e$	1/ ( $\Omega$ m)	Electrical conductivity
$\delta$	m	Skin depth
$\tau$	s	Time

---

---